Forschungszentrum Karlsruhe
Technik und Umwelt

Wissenschaftliche Berichte
FZKA 6618

Thermalhydraulic and Material Specific Investigations into the Realization of an Accelerator Driven System (ADS) to Transmute Minor Actinides

2000 Status Report

J.U. Knebel, X. Cheng, G. Müller, G. Schumacher, J. Konys, O. Wedemeyer, G. Grötzbach, L. Carteciano

Institut für Kern- und Energietechnik
Institut für Hochleistungsimpuls- und Mikrowellentechnik
Institut für Materialforschung
Institut für Reaktorsicherheit
Programm Nukleare Sicherheitsforschung

September 2001

Forschungszentrum Karlsruhe

Technik und Umwelt

Wissenschaftliche Berichte

FZKA 6618

Thermalhydraulic and Material Specific Investigations into the Realization of an Accelerator Driven System (ADS) to Transmute Minor Actinides

2000 Status Report

J. U. Knebel, X. Cheng, G. Müller, G. Schumacher,
J. Konys, O. Wedemeyer, G. Grötzbach, L. Carteciano

Institut für Kern- und Energietechnik
Institut für Hochleistungsimpuls- und Mikrowellentechnik
Institut für Materialforschung
Institut für Reaktorsicherheit

Programm Nukleare Sicherheitsforschung

Forschungszentrum Karlsruhe GmbH, Karlsruhe
2001

Als Manuskript gedruckt

Forschungszentrum Karlsruhe GmbH
Postfach 3640, 76021 Karlsruhe

Mitglied der Hermann von Helmholtz-Gemeinschaft
Deutscher Forschungszentren (HGF)

ISSN 0947-8620

The co-authors and co-workers, who significantly contributed to this work, are listed together with the institute in alphabetical order:

Institut für Kern- und Energietechnik (IKET)
Institute for Nuclear and Energy Technologies

X. Cheng, M. Daubner, F. Fellmoser, J.U. Knebel, V. Krieger, C.H. Lefhalm, K. Mack, P. Miodek, H.J. Neitzel, C. Pettan, H. Piecha, H. Schmidt, R. Stieglitz, R. Vollmer,

Nam-Il Tak (KAERI, Korea)

Institut für Hochleistungsimpuls- und Mikrowellentechnik (IHM)
Institute for Pulsed Power and Microwave Technology

A. Heinzel, R. Huber, G. Müller, G. Schumacher, D. Strauss, F. Zimmermann, A. Weisenburger

Institut für Materialforschung (IMF)
Institute for Materials Research

C. Adelhelm, H. Glasbrenner, J. Konys, W. Krauss, H. Muscher, J. Novotny, Z. Voss, O. Wedemeyer

Institut für Reaktorsicherheit (IRS)
Institute for Reactor Safety

L. Carteciano, B. Dorr, G. Grötzbach

Abstract

Thermalhydraulic and Material Specific Investigations into the Realization of an Accelerator Driven System (ADS) to Transmute Minor Actinides

2000 Status Report

At Forschungszentrum Karlsruhe an HGF Strategy Fund Project entitled "Thermalhydraulic and Material Specific Investigations into the Realization of an Accelerator-Driven System (ADS) to Transmute Minor Actinides" is performed which is funded by the Hermann von Helmholtz-Gemeinschaft Deutscher Forschungszentren (HGF) in the section "Energy Research and Energy Technology" over a time period from 07/1999 to 06/2002 (Förderkennzeichen 01SF9926/3).

The objective of this HGF Strategy Fund Project is the development of new methods and technologies to design and manufacture thin-walled and thermally highly-loaded surfaces which are cooled by a corrosive heavy liquid metal (lead-bismuth eutectic). The beam window is a vital component of an ADS spallation target.
The results of this project will provide the scientific-technical basis which allows the conception and the design of an ADS spallation target and later on a European Demonstrator of an ADS system. The work performed at Forschungszentrum Karlsruhe is embedded in a broad European research and development programme on ADS systems.

The project is divided in three sub-projects:

Sub-Project SP1: Thermalhydraulic Investigations
In the field of experimental thermalhydraulics physical models are developped for conductive and convective heat transfer along thin-walled and thermally highly-loaded surfaces (e.g. beam window) in turbulent lead-bismuth flow. In parallel, a thermalhydraulic computer programme is validated for the low Prandtl number fluid lead-bismuth. Finally, a complete spallation target is numerically designed.

Sub-Project SP2: Material Specific Investigations
In the field of material science physical methods are developped to describe corrosion mechanisms and to solve the corrosion challenge for potential structure and window materials with and without surface treatment for flowing lead-bismuth.

Sub-Project SP3: Oxygen Control System
In the field of reaction kinetics a physical / chemical method is developped to measure and control the oxygen potential in a lead-bismuth loop in order to prevent the corrosion of the materials used.

The experimental investigations are performed in the KArlsruhe Lead LAboratory KALLA.
The investigation of the complex system „heat transfer along thermally highly-loaded surfaces that are in contact with liquid corrosive lead-bismuth under well-defined chemical and material specific boundary conditions" has not been performed up to now. It will be done within this project and directly applied to the design of a spallation target, one key component of an ADS.
This report gives the results achieved during the year 2000.

Kurzfassung

Thermohydraulische und materialspezifische Untersuchungen zur Realisierung einer Beschleuniger getriebenen Anordnung (ADS) zur Transmutation von Aktiniden

2000 Status Report

Am Forschungszentrum Karlsruhe wird ein HGF-Strategiefonds Projekt mit dem Titel „Thermohydraulische und materialspezifische Untersuchungen zur Realisierung einer Beschleuniger getriebenen Anordnung (ADS) zur Transmutation von Aktiniden" durchgeführt, das von der Hermann von Helmholtz-Gemeinschaft Deutscher Forschungszentren (HGF) in der Sektion „Energieforschung und Energietechnologie" für den Zeitraum 07/1999 bis 06/2002 gefördert wird (Förderkennzeichen 01SF9926/3).
Ziel dieses HGF-Strategiefondsprojektes ist es, neue Methoden und Technologien zur Auslegung und Herstellung dünnwandiger, thermisch hochbelasteter Oberflächen, die von einem korrosiven schweren Flüssigmetall (eutektisches Blei-Wismut) gekühlt werden, zu entwickeln. Das Strahlfenster ist eine entscheidende Komponente eines Spallationstargets für einen ADS.
Das Ergebnis dieses Projektes ist ein wissenschaftlich-technisches Instrumentarium zur Konzeption und zur detaillierten Auslegung zunächst eines Spallationstargets und später einer Europäischen Demonstrationsanlage eines ADS. Die Arbeiten am Forschungszentrum sind in ein breites europäisches Forschungs- und Entwicklungsprogramm zu Beschleuniger getriebenen Anordnungen (ADS) eingebunden.

Das Projekt gliedert sich in drei Teilprojekte:
Teilprojekt 1: Thermohydraulische Untersuchungen
Im Bereich der *Thermohydraulik* werden für das Fluid Blei-Wismut physikalische Gesetzmäßigkeiten zum konduktiven und konvektiven Wärmeübergang für die turbulente Umströmung einer thermisch hochbelasteten Oberfläche (z.B. Strahlfenster) entwickelt. Parallel dazu wird ein thermohydraulisches Rechenprogramm für ein Fluid kleiner molekularer Prandtl-Zahl (Blei-Wismut) validiert. Abschließend wird ein komplettes Spallationstarget numerisch ausgelegt.
Teilprojekt 2: Materialspezifische Untersuchungen
Im Bereich der *Materialforschung* werden physikalische Methoden zur Beschreibung der Korrosionsmechanismen und zur Lösung der Korrosionsproblematik für potenzielle Struktur- und Fensterwerkstoffe, mit und ohne Schutzschichten, in strömendem Blei-Wismut entwickelt.
Teilprojekt 3: Sauerstoffkontrolle
Im Bereich der *Reaktionskinetik* wird auf der Basis von physikalisch / chemischen Überlegungen ein Verfahren zur Messung und Regelung des Sauerstoffpotenzials in Blei-Wismut und somit zur Kontrolle der Korrosion der eingesetzten Werkstoffe entwickelt.

Die experimentellen Untersuchungen werden im Flüssigmetalllabor KALLA (KArlsruhe Lead LAboratory) durchgeführt. Eine Betrachtung des komplexen Gesamtsystems „Wärmeübertragung an thermisch hochbelasteten Oberflächen in flüssigem, korrosivem Blei-Wismut unter Berücksichtigung von reaktionskinetisch kontrollierten und materialspezifisch definierten Randbedingungen" ist bisher noch nicht erfolgt. Dies wird mit dieser Arbeit geleistet und direkt für die Auslegung eines Spallationstargets, das eine wesentliche Komponente eines ADS ist, eingesetzt.
Dieser Bericht gibt die im Jahr 2000 erzielten Ergebnisse wieder.

CONTENTS

Thermalhydraulic and Material Specific Investigations into the Realization of an Accelerator Driven System (ADS) to Transmute Minor Actinides

2000 Status Report

Thermalhydraulic and Material Specific Investigations into the Realization of an Accelerator Driven System (ADS) to Transmute Minor Actinides

2000 Status Report

1. Introduction and Objectives

1.1 Introduction

The long-term strategy of the European reseach and development programme in the area of the peaceful utilization of nuclear energy for electricity production is based on scenarios, which consider the importance of the CO_2 emissions and the emission of other greenhouse gases, and the importance of the reduction of fossil fuel. These scenarios are balancing all possible energy resources. Supposing that nuclear energy shall provide a considerable amount of the electric energy produced in Europe, criteria such as energy security, economic efficiency and environmental sustainability are important.
If the option of nuclear energy for electricity production is to be kept open, a research and development programme has to be proposed which covers the following two aspects:

1. Plant life management dealing with the assurance of the high safety level of existing nuclear power plants. This includes risk analysis work which quantifies safety features leading to safety criteria.
2. Development of new reactor systems (evolutionary or innovative) according to market rules, considering: economic aspects, safety assessment, waste management strategies, inherent non-proliferation features and ease of safe-guards' measures applications.

Independent of any scenario considered (revival of nuclear energy or not), a third aspect is of major importance and is expected to grow, Allgeier (2000):

3. *Nuclear waste management*, including non-proliferation and disarmament.

To face facts, the nuclear waste is already existing in large quantities and will be produced continuously in the operating nuclear power plants. This is independent of the future of nuclear energy. As a consequence projects on fundamental actinide research, *partitioning and transmutation (P&T)*, spent fuel behaviour and fuel storage safety evaluations are required.
All these topics have a high degree of promising and future characteristics. They exhibit a national and European challenge to governments / polititians, industry and research. Finally the important aspect of communication and of public perception has to be improved by developing effective strategies.

Transmutation is considered a promising technology worldwide for significantly reducing the amount and, thereby, the long-term radiotoxicity of highly active waste (HAW), European Commission (2001). Transmutation is the treatment of nuclear waste with an intense neutron flux in order to transmute transuranium (TRU) isotopes (plutonium and minor actinides) and long-lived fission products into short-lived radioisotopes or stable nuclei. The maximum reduction of radiotoxicity could be by a

factor of about 100 (Knebel and Heusener (2000)). Transmutation is thus an alternative to the direct deposition of large volumes of highly radioactive waste. Transmutation presents the possibility of closing the fuel cycle including the minor actinides. Plutonium, minor actinides and long-lived fission products can be transmuted in a so called *Accelerator Driven System (ADS)*, which consists of an accelerator, a target module and a subcritical blanket.

The target module for ADS application is a technologically new component, the technical feasibility of which has to be assessed and experimentally proved. This report is concentrating on the development of a spallation target and on the solution of accompagnying questions.

Now, it has to be assessed whether transmutation is technically feasible and whether this technology provides advantages in comparison to direct disposal, especially as worldwide public acceptance of final repositories is low. Although transmutation does not completely eliminate the need for storing HAW in repositories, e.g. due to small inevitable reprocessing losses, the volume of the HAW will become much smaller if the transmutation option were chosen.

1.2 Objectives

The *short-term objective of this HGF Strategy Fund Project* is the development of new methods and technologies to design and manufacture thin-walled and thermally highly-loaded components which are cooled by a corrosive heavy liquid metal. Such a component is the beam window which is cooled by liquid lead-bismuth eutectic. The beam window is a vital component of an ADS spallation target and thus of an Accelerator Driven System (ADS).

The project is divided in three sub-projects (SP):

- SP1: Thermalhydraulic investigations
  Thermalhydraulic investigations of thin-walled, thermally highly-loaded surfaces (beam window and spallation target module) with liquid lead-bismuth as coolant,
- SP2: Material specific investigations
  Investigation of corrosion mechanisms and development of an instruction to condition metals in flowing lead-bismuth,
- SP3: Oxygen control system
  Oxygen concentration measurement and oxygen control in lead-bismuth loops.

The strategy of the project is based both on a theoretical / numerical approach and on an experimental approach.
The summary of the results of the three sub-projects contributes to the method and technology to realize critical and system-relevant components of an Accelerator Driven System (ADS), such as the beam window and the spallation target. The safe design of these components relative to heat transfer, material selection and corrosion control is a basic requirement to guarantee the integral funtionality of an ADS.

The *medium-term objective of this HGF Strategy Fund Project* is the participation in the MEGAPIE Initiative which aims at the development and operation of the

exploratory heavy liquid metal spallation target MEGAPIE with a beam power of *1 MW*. MEGAPIE will be implemented in the existing spallation neutron source SINQ at Paul Scherrer Institute (PSI), Switzerland. A sketch of MEGAPIE is given in figure 1.

Within the MEGAPIE Initiative, this HGF Strategy Fund Project will provide valuable results based on experimental and numerical investigations in the following areas:

- Thermalhydraulic design,
- Liquid metal technology,
- Material specification and selection,
- Corrosion and surface protection,
- Cooling of the beam window.

Details of the SINQ are given in PSI (1997), details about the MEGAPIE Initiative are given in Bauer et al. (1999).

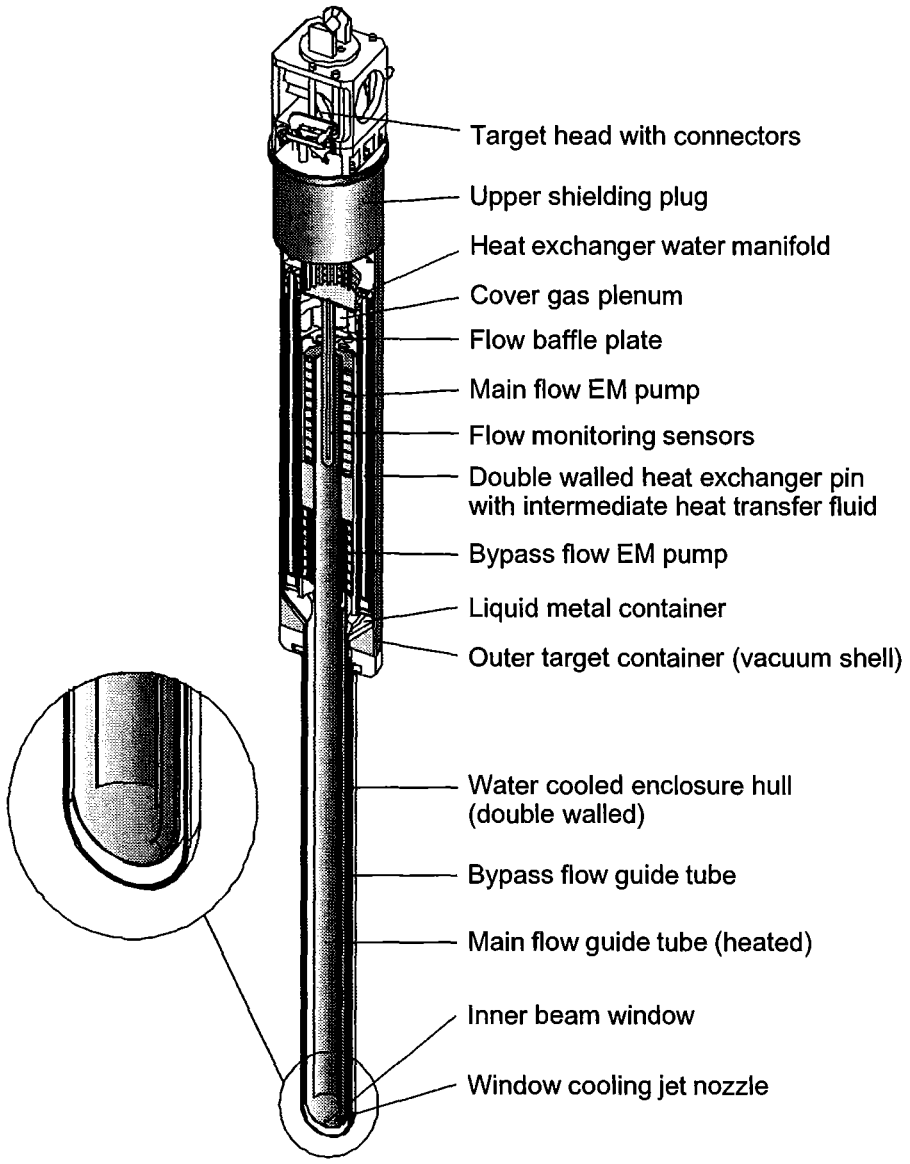

Figure 1: Sketch of the MEGAPIE (MEGAwatt PIlot Experiment) spallation target for SINQ at Paul Scherrer Institute (PSI) Switzerland.

The *long-term objective of this HGF Strategy Fund Project* is – on the basis of the newly developped methods and technologies – to provide the scientific-technical tool which allows, now, the conceptual design and, at a later stage, the detailed design of a European Experimental Demonstrator of an ADS.
The Experimental Demonstrator with a thermal power of about 80 to 100 MW(th) is a milestone towards the long-term realization of a prototypical ADS with a thermal power of about 1500 MW(th).
The tools provided by this HGF Strategy Fund Project comprise of

- A thermalhydraulic and material specific data base resulting from fundamental and application-oriented experiments,
- A computational fluid dynamics (CFD) code validated for lead-bismuth,
- An identification of beam window and structure materials,
- An instruction for corrosion control, material conditioning and oxygen control in lead-bismuth loops.

1.3 Accelerator Driven System (ADS)

An *accelerator driven system (ADS)* consists of three main parts: an accelerator for primary particles (protons), a spallation target (or target module) in which the protons produce free nucleons (neutrons) in a spallation reaction (external neutron source), and a subcritical blanket in which, first, the fission reaction, producing fission neutrons (internal neutron source) and thermal energy, and second, the transmutation reaction occur, Bowman et al. (1992). The protons are injected into the spallation target through a vacuum beam pipe, the beam pipe being closed by a window at the end. The target is a heavy liquid metal (e.g. lead Pb or eutectic lead-bismuth Pb-Bi). The spallation neutrons produced in the spallation target are completely independent of the subcritical blanket. A shut-down of the accelerator or an interruption of the proton beam immediately stops the fission reaction. Safety aspects of such a subcritical system are discussed in Wider (1998), Maschek, Thiem, Heusener (1999), Klügel et. al. (1999). A sketch of an ADS is given in figure 2.

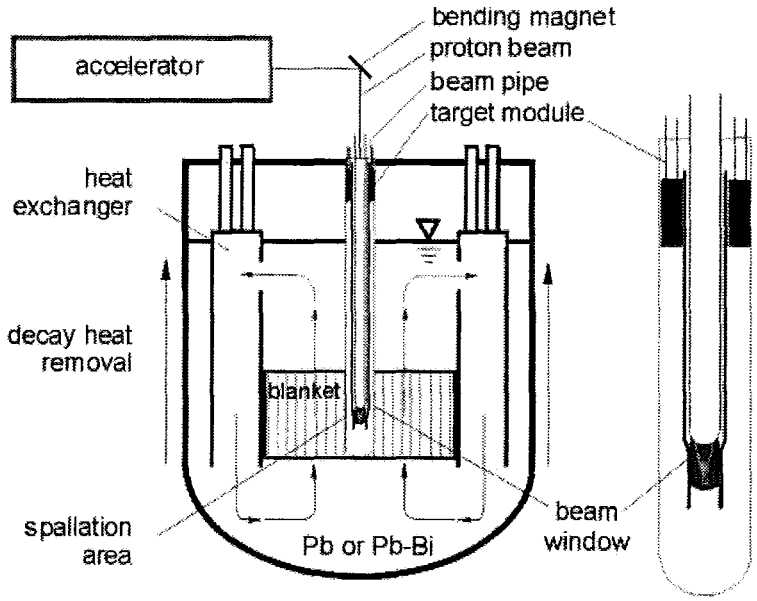

Figure 2: Sketch of an accelerator driven system (ADS).

The strategic objective of an ADS is to transmute long-lived radioactive waste and, thus, to close the fuel cycle including minor actinides, (Heusener und Salvatores (1998), Carminati et al. (1993), Rubbia et al. (1995)). The waste which is treated in an ADS can be divided into two parts: the minor actinides such as Neptunium, Americium und Curium and some long-lived fission products such as technetium 99 and iodine 129. The two latter species can diffuse in the biosphere in the long run where they can be selectively incorporated by organisms.
The ADS technology is a natural extention to the existing park of light water reactors (LWR). The use of ADS reduces the amount and the radiotoxicity of radioactive waste which has to be transported and stored in a final repository. Such considerations are formulated for Europe, TWG (2001), the United States, US-DOE (1999) and van Tuyle (2000), Japan, Takizuka et al. (1998), and Korea, Park (1999).

The evaluation commission of the Bundesministerium für Wirtschaft (BMWi) considers the strategic work on transmutation a priority task. The evaluation commission considers it as required to fundamentally investigate the physical and technical conditions for the technological realization of the ADS technology, Evaluierungskommission (2000).

This HGF Strategy Fund Project provides an essential scientific contribution to the application-oriented fundamental research work within the energy technology of an ADS as mentioned above.

1.4 Scientific Approach and Programme

The scientific approach is governed by three critical technical questions to an ADS, which need further research and development efforts and the answer to which is a basic requirement to successfully operate an ADS.
The scientific approach within the HGF Strategy Fund Project in order to reach the objectives is schematically given in figure 3. The project time table is given in table 1.
Further details on the scientific approach and the programme are explicitely given in Knebel et.al. (2000).

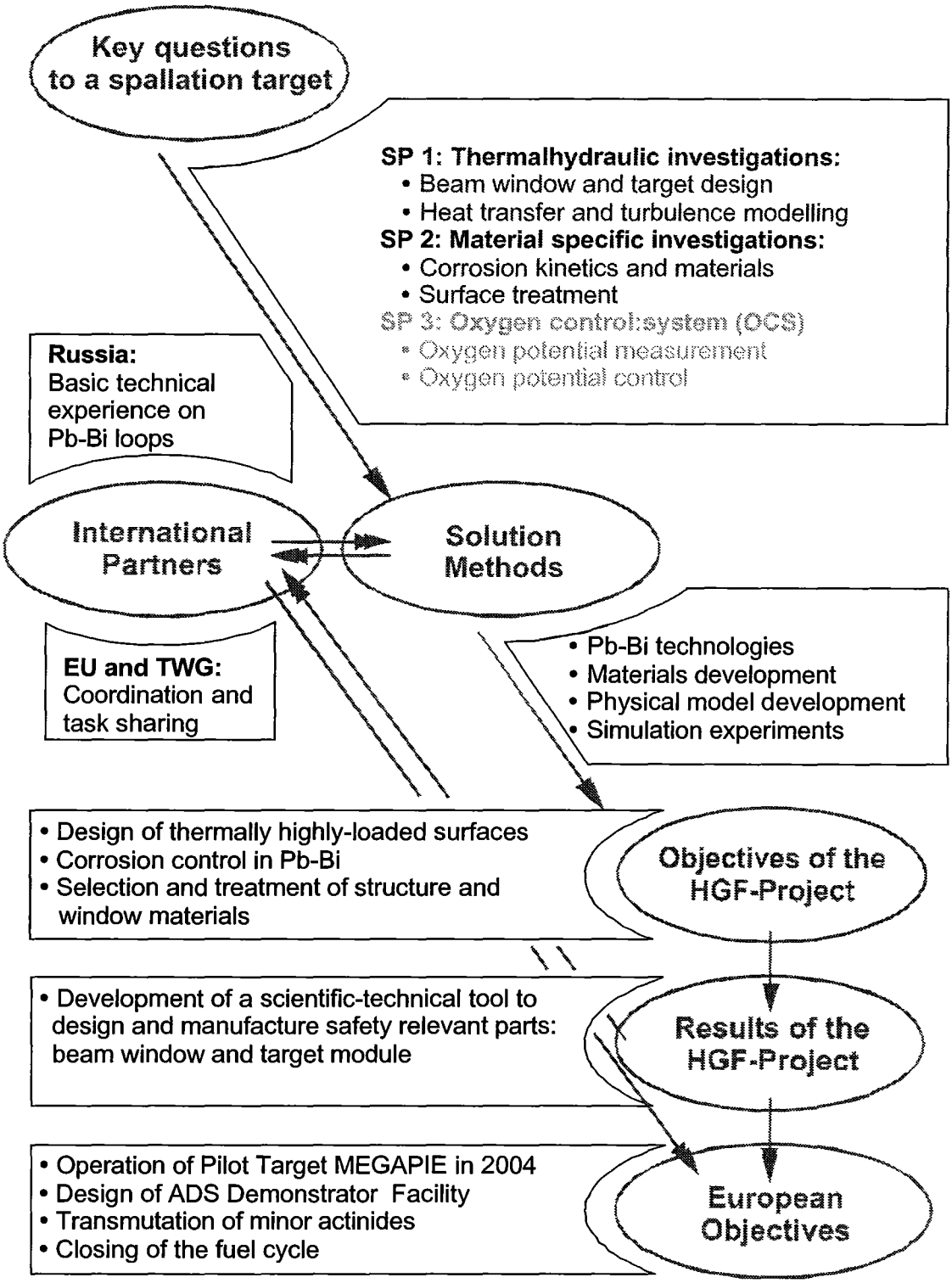

Figure 3: Scientific approach within the HGF Strategy Fund Project to reach the objectives.

Table 1: Project time table.

period / Sub-Projects		2000				2001				2002		
	IV	I	II	III	IV	I	II	III	IV	I	II	III
Sub-Project 1: *WP1.* Design of beam window, Model experiment in water *WP2.* Basic experiment in Pb-Bi and physical model development *WP3.* Experiment and modelling of beam window in Pb-Bi *WP1.-WP3.* Validation of thermalhydraulic computer code												
Sub-Project 2: *WP1. – WP3.* Orientation experiments in stagnant Pb-Bi Performance of corrosion experiments Data / probe evaluation and material specific interpretation												
Sub-Project 3: *WP1.* Development of oxygen probe, oxygen measurement, long-term investigations *WP2.* Oxygen Control System OCS												
Final report												

2. Results during 2000

Within this chapter the results achieved during 2000 are collected. The results are classed with the respective sub-projects and work packages. Cross-links between the sub-projects are outlined.
Before the 2000 results of the three sub-projects are presented and discussed in detail, a short description and the status of the KArlsruhe Lead LAboratory KALLA is given.

2.1 KArlsruhe Lead LAboratory KALLA

The KArlsruhe Lead LAboratory KALLA summarizes all experimental activities at Forschungszentrum Karlsruhe which use the fluid lead-bismuth eutectic, (KALLA (2001)). The involved institutes are Institute for Nuclear and Energy Technologies (IKET), Institute for Pulsed Power and Microwave Technology (IHM), Institute for Materials Research III (IMF III).
The experimental activities of KALLA can be divided in two groups:

- Stagnant experiments:
  - COSTA 1 to 3 (COrrosion test stand for STagnant liquid lead Alloys)
  - KOSIMA 1 to 6 (Karlsruhe Oxygen Sensor In Molten Alloys)
  - KOCOS (Kinetics of Oxygen COntrol Systems)

- Loop experiments (figure 4):
  - THESYS (Technologies for HEavy metal SYStems)
  - THEADES (THErmalhydraulics and Ads DESign)
  - CORRIDA (CORRosion In Dynamic lead Alloys)
  - K4T (Karlsruhe 4 MW Target experiment)

The Technical Working Group (TWG) proposes to establish only a few larger laboratories for experimental investigations in liquid lead-bismuth within the European Union. With the KArlsruhe Lead LAboratory KALLA at Forschungszentrum Karlsruhe there will be a strategic focal point in the field of lead-bismuth technologies in Germany.

In this sense, KALLA is meant to be an open user laboratory for experiments which are relevant for ADS applications. KALLA shall enhance international collaboration and encourage scientific staff exchange. In addition, your scientists can be educated and trained in heavy liquid metal technologies and applications. This is in agreement with the newly proposed direction of EURATOM research in the Framework Program 2002-2006, which will strengthen both integrated projects and networks of excellence, EURATOM (2001).

In the following, each experiment is briefly explained, giving the objectives, the experimental set-up, the parameter range and a representative photograph. Further information can be found in *http:// www.kalla.fzk.de*.

Parallel to the lead-bismuth experiments in KALLA, model experiments with water as fluid are performed in the test facility HYTAS (HYdraulic behaviour in spallation TArget Systems). HYTAS allows for hydraulic and heated experiments in various lucid test sections, the measurement techniques being a 4-beam 2-component fiber optical Laser Doppler Anemometer (LDA) and Laser light sheet for the velocity field and thermocouples and shadow graph for temperature field. The application of particle image velocimetry (PIV) and ultrasonic velocimetry technique (UVP) is envisaged.

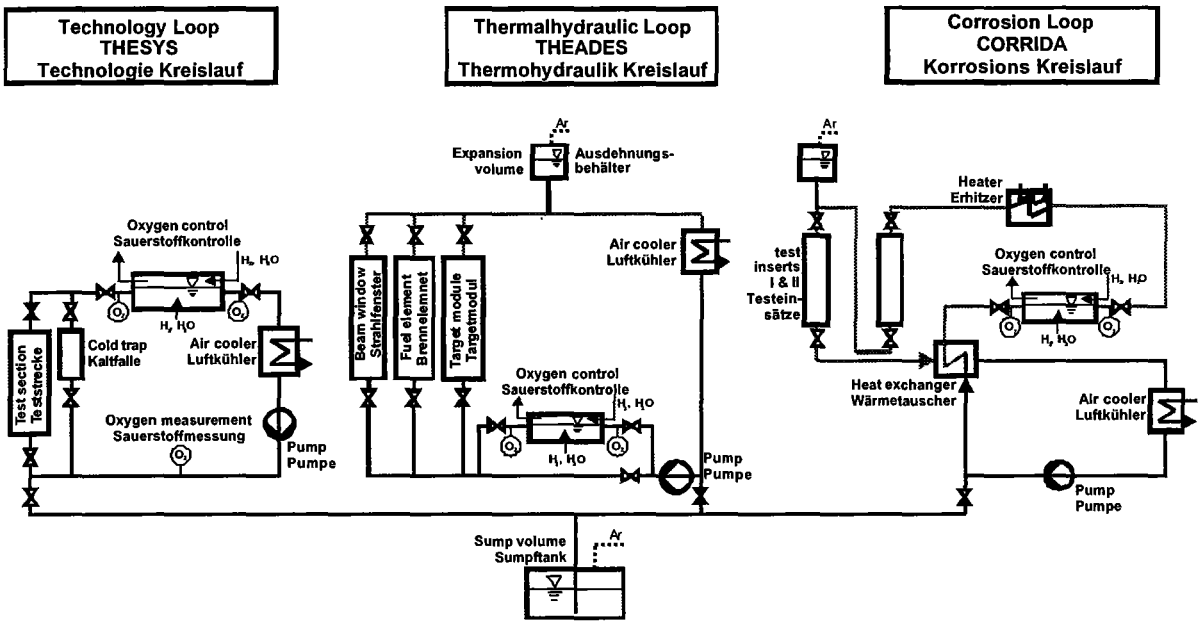

Figure 4: The three loops of KArlsruhe Lead LAboratory KALLA:

- Technology Loop THESYS,
- Thermalhydraulic Loop THEADES,
- Corrosion Loop CORRIDA.

2.1.1 Stagnant Experiment COSTA

The main objectives of the stagnant experiment COSTA (COrrosion test stand for STagnant liquid lead Alloys) are:

- Investigation of corrosion mechanisms
- Influence of protection layers on corrosion
- Investigation of GESA treated surfaces
- Influence of surface alloying on corrosion.

The parameter range is:	max temperature	700°C
	number of test sections	3
	number of crucibles	10 per test section
	number of specimens	2 per crucible
	specimen dimensions	15 x 10 x 2 mm^3
	oxygen control system (OCS)	yes
	heavy liquid metal	Pb or Pb-Bi

The flow diagramme of COSTA together with the oxygen control system (OCS) is given in figure 5. A photograph is given in figure 6. COSTA is in continuous operation since November 1997. More technical data are given in Knebel et al. (2001).
In total there are three test sections, each being equipped with a maximum of 10 crucibles.
A new test section to be used by guest scientists according to their specifications can be easily provided.

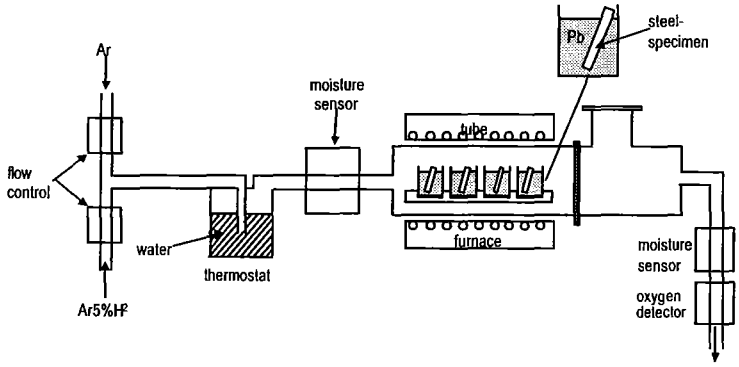

Figure 5: Flow diagramme of COSTA.

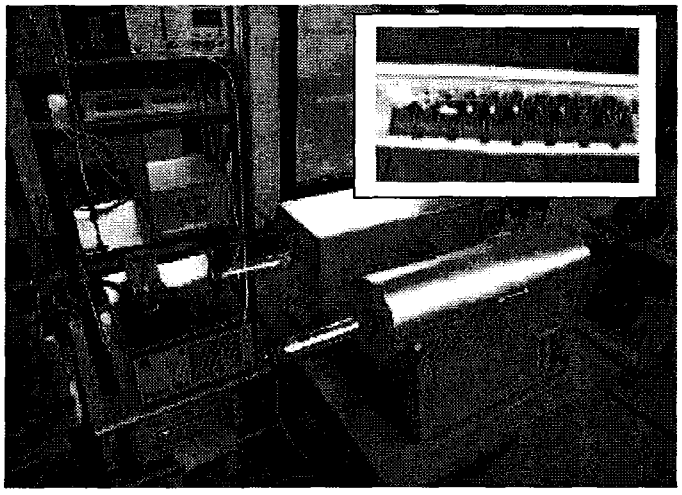

Figure 6: Photograph of stagnant experiment COSTA and of crucibles (upper right).

2.1.2 Stagnant Experiment KOSIMA

The main objectives of the stagnant experiment KOSIMA (Karlsruhe Oxygen Sensor In Molten Alloys) are:

- Development of oxygen sensors
- Investigation of oxygen sensor performance
- Calibration of oxygen sonsors

The parameter range is:	max temperature	700°C
	number of test sections	6
	number of sensors	3 per test section
	oxygen control system (OCS)	yes
	heavy liquid metal	Pb or Pb-Bi

The flow diagramme of KOSIMA together with the oxygen control system is given in figure 7. A photograph is given in figure 8. KOSIMA is in continuous operation since 1998. More technical data are given in Knebel et al. (2001).
In total there are six test sections, each being equipped with a maximum of 3 oxygen sensors.

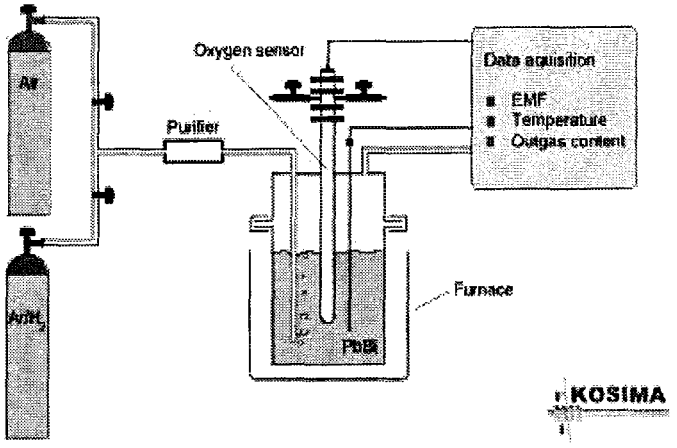

Figure 7: Flow diagramme of KOSIMA.

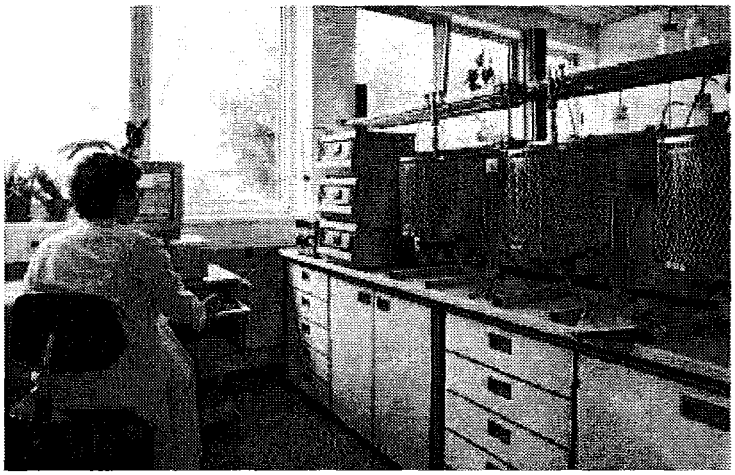

Figure 8: Photograph of KOSIMA.

2.1.3 Stagnant Experiment KOCOS

The main objectives of the stagnant experiment KOCOS (Kinetics of Oxygen COntrol Systems) are:

- Development of oxygen control system (OCS),
- Application of OCS to stagnant and flowing Pb or Pb-Bi,
- Calibration of oxygen sonsors,
- Measurement of diffusion coefficients of oxygen in Pb-Bi,
- Measurement of oxygen mass exchange rates.

The parameter range is:	max temperature	600°C
	number of test sections	1
	number of sensors	4 per test section
	oxygen control system (OCS)	yes
	heavy liquid metal	Pb-Bi

The flow diagramme of KOCOS together with the oxygen control system is given in figure 9. A photograph is given in figure 10. KOCOS is in continuous operation since November 1999. More technical data are given in Knebel et al. (2001).
The instrumentation of OCS is a modular stand-alone system which can be applied to any Pb or Pb-Bi system. The oxygen control is done via the gas phase, e.g. by controlling the H_2/H_2O ratio in the gas phase above the heavy liquid metal, Lefhalm et al. (2001). There is a simultaneous measurement of the partial oxygen pressure using oxygen probes both in the liquid metal and in the gas phase.

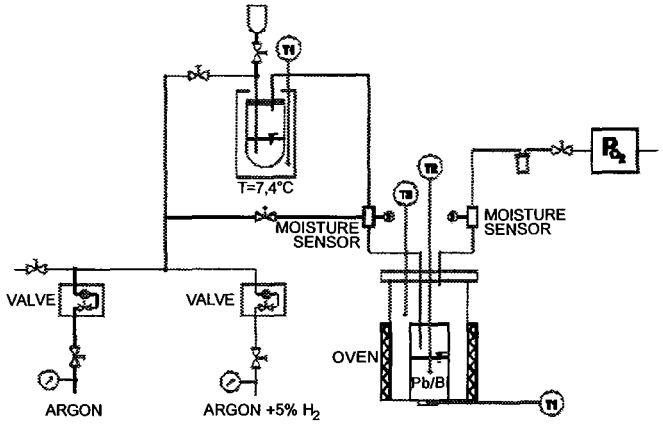

Figure 9: Flow diagramme of KOCOS.

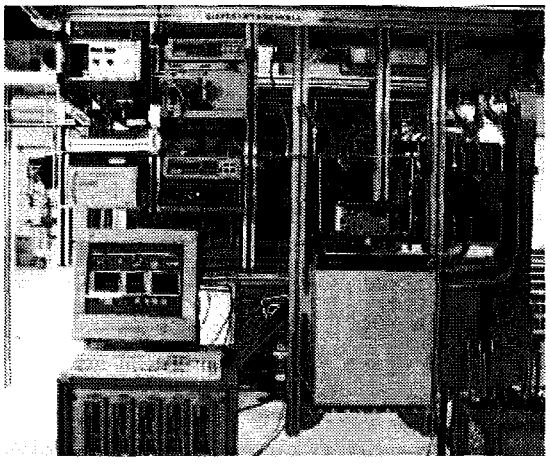

Figure 10: Photograph of KOCOS.

2.1.4 Loop Experiment THESYS

The loop experiment THESYS (Technologies for HEavy metal SYStems) concentrates on fundamental lead-bismuth technologies. The main objectives of THESYS are:

- Optimization of oxygen control system (OCS) for loop applications,
- Development of thermalhydraulic measurement techniques
  - temperature: thermocouples and PT100-thermometers
  - pressure: capacitive pressure gauges with coupling fluid
  - flow rate: magnetic flowmeter, ultrasonic flowmeter, turbine flowmeter,
  - velocity: miniature permanent magnet flowmeter (MPP) probe, ultrasonic Doppler technique (UVP)
  - wall heat flux: heat emitting temperature sensing surface (HETSS)
- Heat transfer experiments (data bank for code validation)
- Turbulence measurements (data bank for code validation)
- Development of high performance inconel heaters (fuel rod simulator)
- Set-up of thermalhydraulic data base for physical model and code validation

The parameter range is:		
	max temperature	450°C
	max flowrate	3 m³/h
	number of test sections	1
	test section diameter	60 mm
	test section length/diameter	40
	oxygen control system (OCS)	yes
	heavy liquid metal	Pb-Bi

The flow diagramme of THESYS is given in figure 4. A photograph is given in figure 11. THESYS is equipped with an OCS. More technical data are given in Knebel et al. (2001).

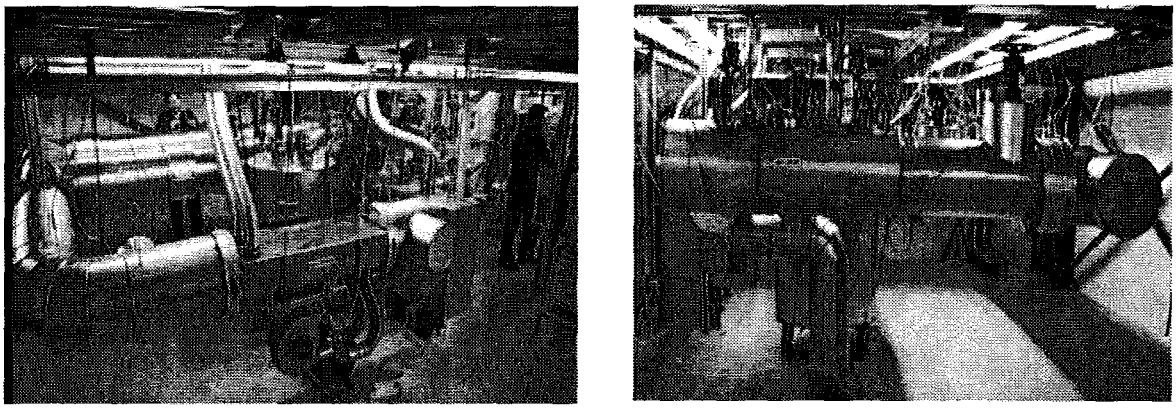

Figure 11: Photograph of THESYS: total view from south (left) and east (right).

2.1.5 Loop Experiment THEADES

The loop experiment THEADES (THErmalhydraulics and Ads DESign) concentrates on thermalhydraulic single-effect investigations of ADS components which are of vital importance for the design work. The main objectives of THEADES are:

- Cooling of the beam window
- Flow field of a windowless target configuration
- Cooling of fuel element(s)
- Heat transfer characteristics of a Pb-Bi / Pb-Bi heat exchanger
- Heat transfer characteristics of a steam generator
- Heat transfer characteristics of a Pb-Bi / air heat exchanger
- Set-up of thermalhydraulic data base for physical model and code validation

The parameter range is:		
	max temperature	450°C
	max flowrate	100 m³/h at 4.5 m NPSH
	max electrical power	4 MW
	number of test sections	4
	max test section height	3.4 m
	oxygen control system (OCS)	yes
	heavy liquid metal	Pb-Bi

The flow diagramme of THEADES is given in figure 4. A photograph is given in figure 12. THEADES is equipped with an OCS. More technical data are given in Knebel et al. (2001).

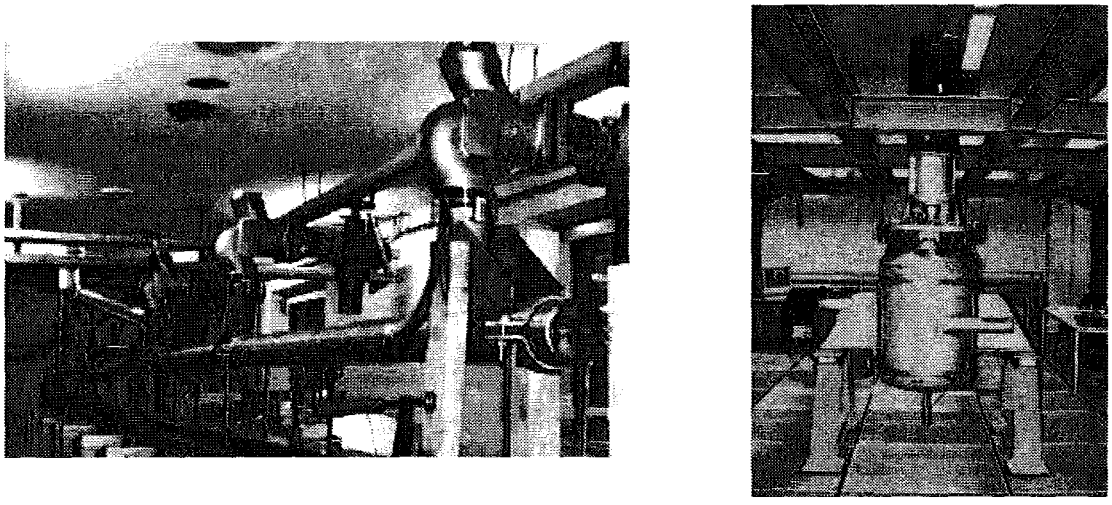

Figure 12: Photograph of THEADES: sump tank and three inlet lines for test sections (left) and immersion pump (right) before being insulated.

2.1.6 Loop Experiment CORRIDA

The loop experiment CORRIDA (CORRosion In Dynamic lead Alloys) concentrates on fundamental corrosion investigations of low activation structure and beam window materials which are considered in the ADS design work. The main objectives of CORRIDA are:

- Fundamental corrosion mechanisms
- Formation and stability of protection layers
- Performance of mechanical tests
- Development of structure and beam window materials

The parameter range is:	max temperature	550°C (650°C)
	max flowrate	5 m³/h
	number of test sections	2
	number of specimens	14 per test section
	specimen dimensions	∅ 8 mm, 35 mm long
	oxygen control system (OCS)	yes
	heavy liquid metal	Pb-Bi

The flow diagramme of CORRIDA is given in figure 4. A photograph is given in figure 13. CORRIDA is equipped with an OCS. More technical data are given in Knebel et al. (2001).

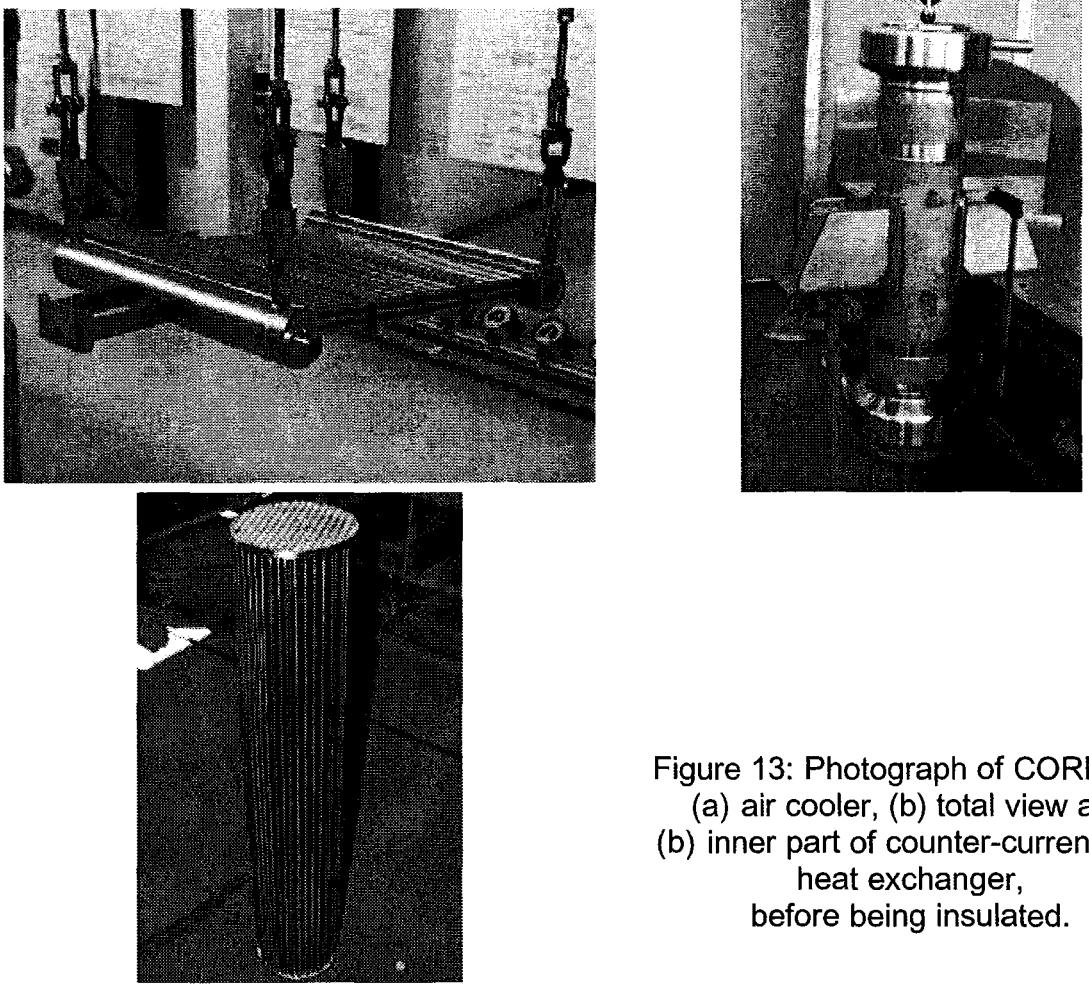

Figure 13: Photograph of CORRIDA:
(a) air cooler, (b) total view and
(b) inner part of counter-current flow
heat exchanger,
before being insulated.

2.1.7 Integral Experiment K4T

The loop experiment K4T (Karlsruhe 4 MW Target experiment) concentrates on thermalhydraulic integral investigations into the heat removal from the spallation target for normal and decay heat removal conditions which are of vital importance for the design work. The main objectives of K4T are:

- Heat transport within a closed spallation target module
- Steady-state and transient thermalhydraulic behaviour of coupled heat removal system (target loop, intermediate loop, air cooler) under natural circulation and/or forced flow conditions
- Set-up of thermalhydraulic data base for physical model and code validation

The parameter range is:		
	max temperature	550°C
	max flowrate	variable
	max electrical power	4 MW
	target loop fluid	Pb-Bi
	intermediate loop fluid	Pb-Bi (or organic fluid)
	oxygen control system (OCS)	yes

Currently, the integral experiment K4T is in the design phase. A sketch of K4T which is based on design considerations of Neitzel and Knebel (2000) is given in figure 14. All heights are scaled 1:1. More technical data are given in chapter 2.2.3.2.

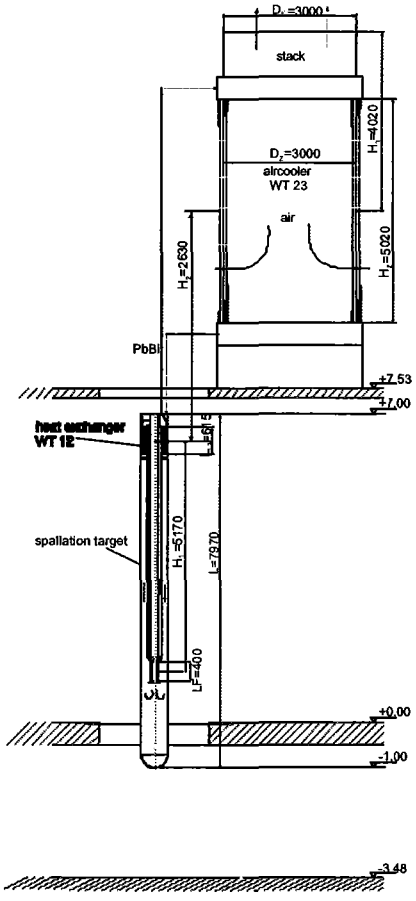

Figure 14: Integration of K4T in KALLA laboratory building.

2.1.8 Data Acquisition and Control Scheme

In the KArlsruhe Lead LAboratory KALLA a distributed measurement and automation system consisting of several personal computers and measurement devices is used. All PCs are linked over a 100 Base-TX switched Ethernet and are connected to a central server, which provides connectivity to the intranet and internet. The configuration and data storing is managed by a central database server running IBM DB2 V7 for Linux, attached to a Level 5 RAID with backup to obtain highest possible reliability and data security. The programming based on National Instruments LabVIEW 6.0i including the Datalogging and Supervisory Control Modules (DSC) which allows to share measurement values in the internal network and so to remote access any data from any PC.
The process control is managed by one Siemens S5 processor per loop connected over serial AS511 interface to a control PC running National Instruments Lookout OPC Server. Target values for heating temperatures, pump power and other process equipment can be entered by the operator using a graphical human machine interface (HMI) on these PCs. Historical process data are logged continuously to the database and can be reviewed at any time. By this means a user friendly, long term state monitoring for the test facilities is made available.
To acquire the measurement data of the extensive loop instrumentation, mainly three different devices come into operation. First Schlumberger Integrated Measurement Pods (IMPs) are used for logging of the internal Pb-Bi temperatures in the loops and for acquisition of voltage and currency as scaled outputs of arbitrary devices. Second the Beckhoff Fieldbus with different types of terminals and controllers is installed to operate the Oxygen Control Systems (OCS) in combination with external control equipment. Third fast data acquisition cards (DAQ) in a National Instruments PXI rack are used for special measurement tasks at the test sections. The resulting data are collected by personal computers and also filed in the central database for later analysis.
In addition to the above described features a very new technique in the field of data acquisition and control is used at KALLA. A wireless local area network (WaveLAN) is installed at the laboratory which gives the possibility to use one or more laptops as mobile maintenance and measurement units. With this installation one can control an experiment from "within" the test facility always having direct access to the desired measurement data and control operations.
Figure 15 gives a schematic view of the distributed measurement and automation network in the Karlsruhe Lead Laboratory KALLA. Online data displays are given on *http:// www.kalla.fzk.de/kalla.*

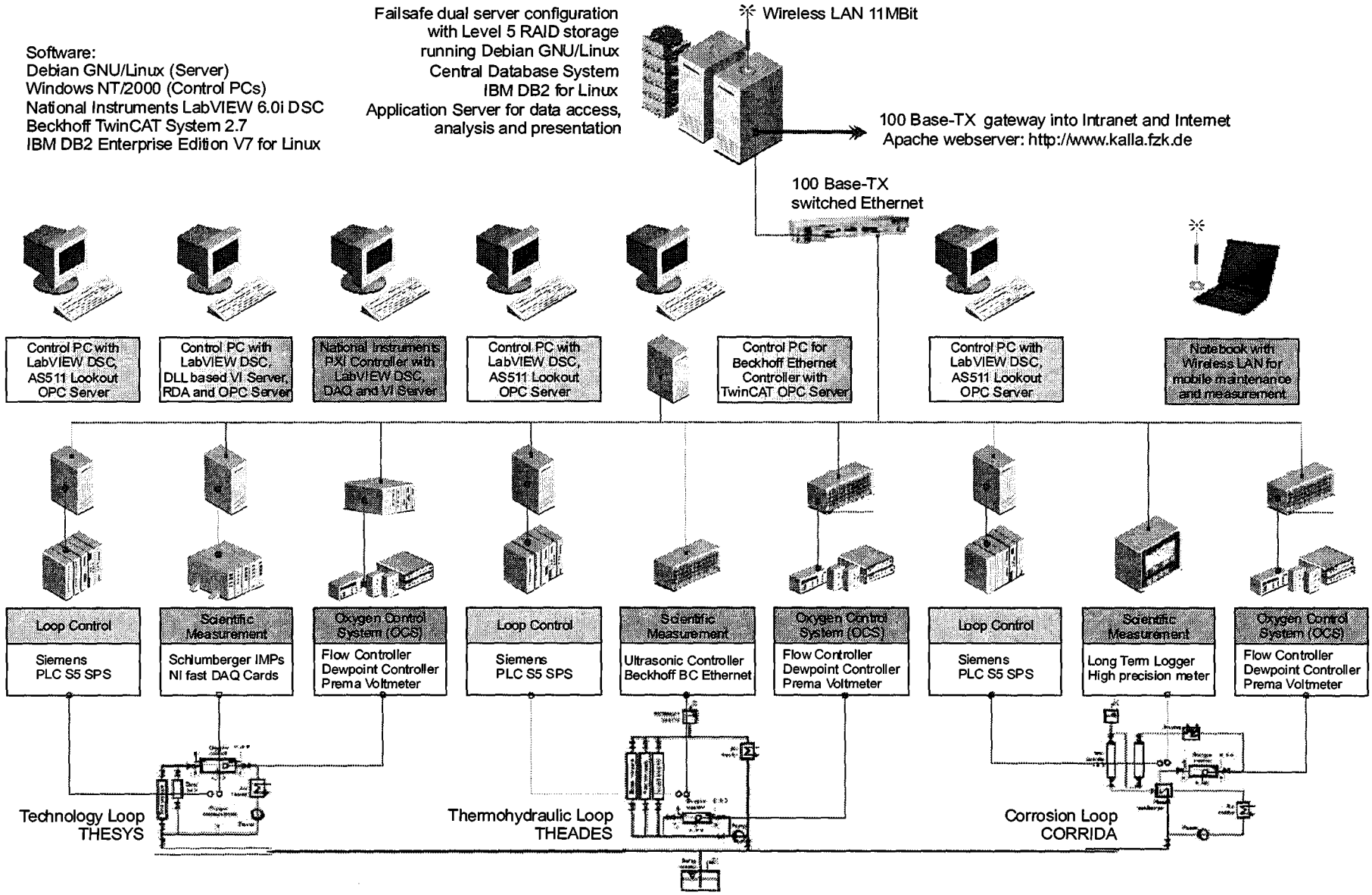

Figure 15: Automization scheme of KALLA: data acquisition and control.

2.2 Sub-Project SP1: Thermalhydraulic Investigations

A three steps strategy has been proposed for the research activities accompagnying the spallation target design.
In the *first step* a numerical analysis is carried out with available CFD codes (CFX from CFX Int. Services (1995), FIDAP from Fluid Dynamics International (1993) and the Forschungszentrum Karlsruhe code FLUTAN from Willerding and Baumann (1996)), to provide a fundamental knowledge about the steady-state and transient thermalhydraulic behaviour of a spallation target, and to develop evaluation criteria which are to be applied to a design selection procedure at a later stage.
In the *second step* model experiments are performed, to provide an experimental data base for physical model development and code improvement and validation. At the present stage a certain deficiency in applied Pb-Bi technology exists so that experimental investigations both with a model fluid, e.g. water, and with the realistic coolant, Pb-Bi eutectic, are recommended. A model experiment using water as fluid allows to both perform a systematical study of the physical phenomena involved and to apply sophisticated measurement techniques, which is not the case with the prototypical fluid. To this purpose the water test facility HYTAS (HYdraulic behaviour in spallation TArget Systems) has been erected. However, the results obtained in a water model experiment cannot be directly transferred to the prototype conditions as far as heat transfer characteristics and buoyancy effects are concerned.
In the *third step* experimental studies in liquid Pb-Bi are performed in the KArlsruhe Lead LAboratory KALLA for the final design of a beam window. The design of the complete spallation target module is done numerically first. The experimental investigations of a target module is beyond the scope of this HGF Strategy Fund Project.
The first step is done for two beam window designs which are related to two ongoing internationally well established projects on the design of a spallation target: the ISTC 559 Project (Yefimov (1998)) and the MEGAPIE Initiative (Bauer et al. (1999)).
The second step is done for a simple heat transfer experiment in a rectangular channel and for a buoyant jet flow benchmark task.
The third step concentrates on the development of a prototypical beam window and spallation target geometry.

2.2.1 Work Package WP1: Design of a Beam Window Based on Numerical Simulations and Model Experiments with Water as Fluid

2.2.1.1 Experimental Study on the ISTC Target

Test Facility HYTAS:

Figure 16 gives a schematical sketch of the water test facility HYTAS. The water loop is capable of circulating a maximun volumetric flow rate of 100 m^3/h with a maximum pressure drop of 0.4 MPa. Test sections with a maximum vertical length of 3.5 m can be integrated in the test facility.
The main purpose of the HYTAS experiment is to study the hydraulic behaviour of the flow around the beam window of a spallation target. It is well known that the hydraulic behaviour of a liquid metal flow in a prototype geometry can be exactly simulated in a model experiment using water, as long as the Reynolds numbers in both the prototype and the model are identical.

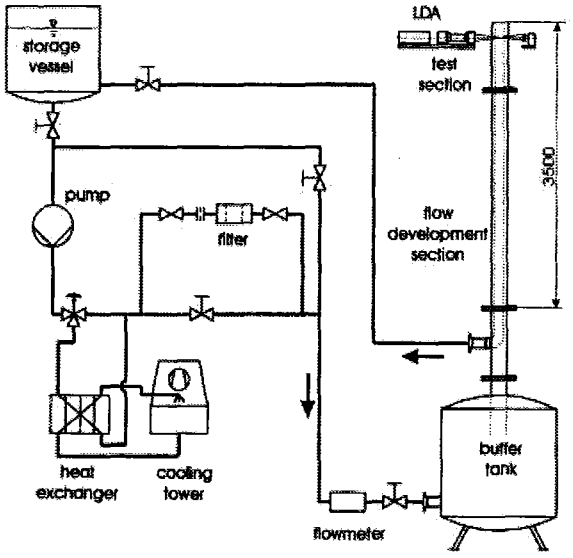

Figure 16: Sketch of the HYTAS test facility.

Test Section for ISTC Target:

During the reported time period experiments have been carried out for the ISTC 559 target. More details about the ISTC 559 project can be found in Cheng and Slessarev (2000). The design of the active part (beam window and spallation area) is one of the main tasks in the target design. Figure 17 shows a sketch and a photograph of the ISTC 559 model test section. The beam window has a semi-spheric surface, the diameter being 110 mm. The active part consists of two coaxial cylinders with inner diameters of 130 mm and 185 mm, respectively. The coolant flows into the annular gap between the two cylinders, makes a U-turn at the top, passes along the window surface, and then exits the active part via the central cylinder. To reduce the flow stagnation zone near the center of the beam window (stagnation point), where the heat deposition by the proton beam has its maximum, a perforated steel plate with distributed holes is installed close to the beam window. The plate has a thickness of 5 mm. The porosity is highest on the centerline and decreases with increasing distance from the center line. The flow resistance increases with increasing distance from the centerline. In this way, the coolant flow and the heat transfer near the center of the beam window is significantly enhanced.

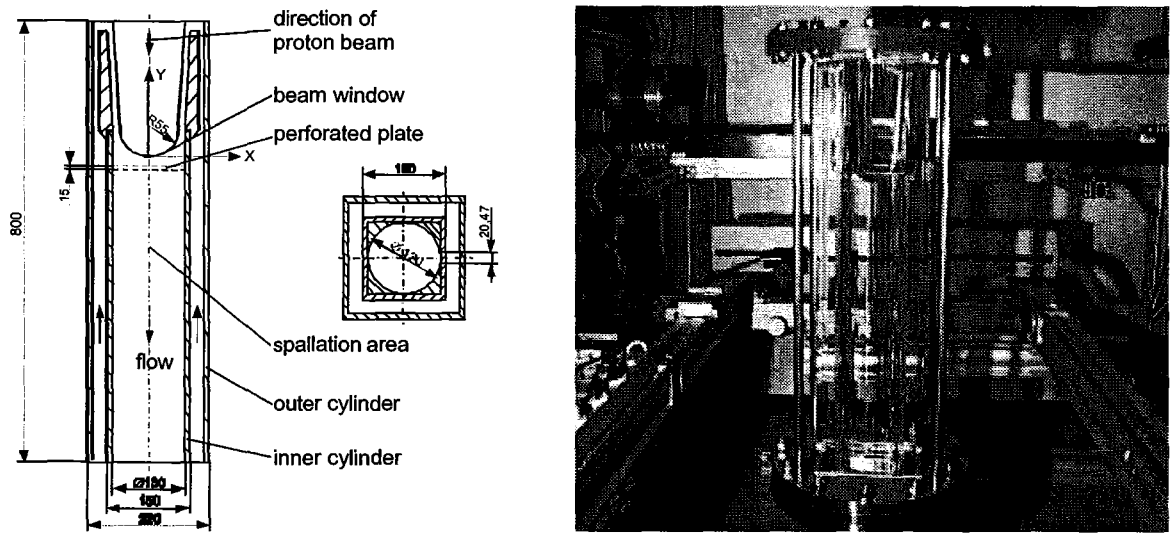

Figure 17: Test section of the ISTC 559 beam window geometry.

Results:

The local velocities are measured with a 2-D Laser-Doppler Anemometer (LDA). To present the results, a coordinate system is chosen, the origin of which is located on the center of the window surface, see figure 17. The x-axis is in the radial direction. The y-axis is parallel to the axis of the target, the positive direction being towards the direction of the proton beam. Figure 18 shows the distribution of the mean axial velocity u versus the radial direction of the test channel with a perforated plate. The distance between the perforated plate (5 mm thick) and the center of the beam window is 15 mm. It is found that there is no detachment of the boundary layer from the window surface, i.e. at both elevations (y = 0 and y = 10 mm) the axial velocity is negative for all radial positions. Close to the perforated plate (e.g. at y= -10 mm) a strong increase in the axial velocity is obtained around the axis of the target. As indicated in figure 18, the axial velocity on the centre line (x = 0) is about -0.8 m/s at 5 mm upstream of the plate, e.g. at y = -10 mm, and -1.5 m/s at 10 mm downstream of the plate, e.g. at y = -30 mm. Obviously, flow recirculation occurs both downstream of the plate and between the holes.
Figure 19 compares the radial profile of the axial velocity at y = 0 mm for both cases: with and without perforated plate. It is seen that the introduction of the perforated plate leads to a strong increase in the axial velocity near the beam window. The stagnation zone close to the beam window is reduced significantly. In the outer region, i.e. $x \geq 40$ mm, flow recirculation occurs. In order to avoid a hot spot in the fluid for the case of a proton beam shift, an optimization of the distribution of the holes in the perforated plate is required.

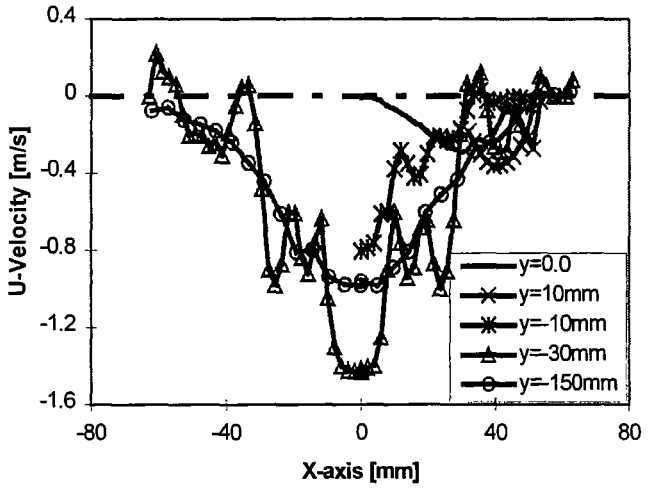

Figure 18: Axial velocity profiles with downward flow through the central channel and a perforated plate, V = 10 m³/h.

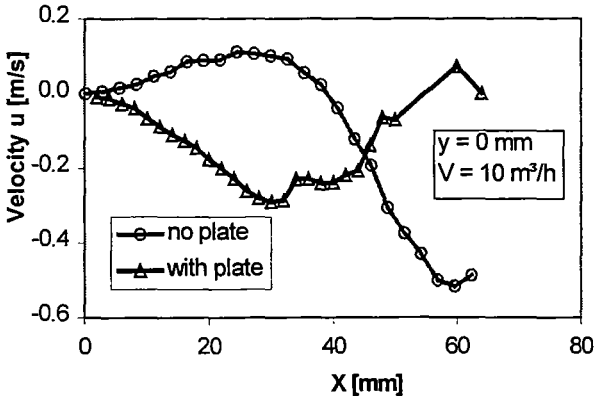

Figure 19: Axial velocity profiles with downward flow through the central channel at y = 0 mm: comparison of the experimental results with and without perforated plate.

2.2.1.2 Numerical Study on the MEGAPIE Target

MEGAPIE target:

MEGAPIE (MEGAwatt PIlot Experiment) is a collaborative effort of CEA, CNRS and SUBATECH France, ENEA Italy, FZK Germany, JAERI Japan, PSI Switzerland and SCK-CEN Belgium. The final goal of the MEGAPIE Initiative is to design, build, operate, examine and decommission a liquid lead-bismuth spallation target of 1 MW beam power, making use of the existing accelerator facility SINQ at PSI, Bauer et al. (1999). The major objectives are:

- Full feasibility demonstration of a spallation target system,
- Study of radiation and damage effects of structures and beam window in a realistic spallation spectrum,
- Effectiveness of the window cooling under realistic conditions,
- Liquid metal / metal interactions under irradiation and stress.

The MEGAPIE Initiative will demonstrate the feasibility of coupling a high power accelerator and a spallation target for future use in an ADS. The MEGAPIE experiment will provide an important data base for the validation and the improvement of neutronic and thermalhydraulic computer codes. In addition, it allows experience to be gained in the safe handling and decommissioning of irradiated components which have been in contact with lead-bismuth.

A reference design of the active part of the target is indicated in figure 20. The semi-spheric beam window has an inner diameter of 174 mm. The diameter of the guide tube is about 130 mm. To improve the window cooling, especially in the region of the window center, two different measures are considered. The first method is to cut the lower end of the guide tube with an inclination angle of about 10° to the horizontal. In this way the axial-symmetry of the flow is destroyed and the flow stagnation zone near the window center can be reduced. With the second method a bypass flow is introduced across the beam window via a jet pipe, as indicated in figure 20. The geometrical details of the jet pipe and of the guide tube have to be optimised based on numerical and experimental results.

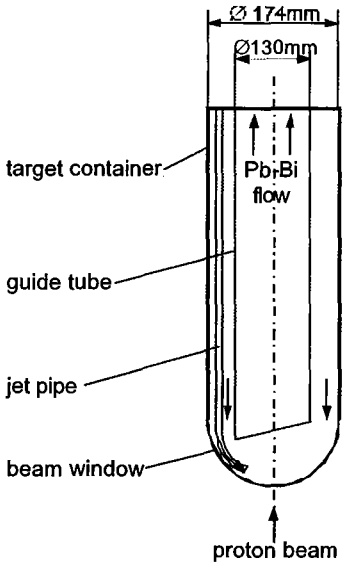

Figure 20: Active part of the 1 MW pilot spallation target MEGAPIE.

Results:

One of the proposals for heat removal from the active part of the MEGAPIE target is a combined mode of natural and forced convection. Forced convection is only restricted to the injection bypass with a mass flow rate of about 5 kg/s, whereas the main flow through the annulus between target container and guide tube is initiated by natural convection. Under natural convection mode, the start-up phase (or the onset of the convection) is of crucial importance. Any excessive hot spot in the fluid as well as in the beam window material has to be avoided. The 1-D code HETRAF (Cheng (1994)), has been applied to analyze the transient behavior of the target under beam start-up and beam interrupt conditions. Figure 21 shows an example of the transient behaviour of the mass flow rate and the maximum coolant temperature after switching on the beam power. The beam power in the reference case is suddenly increased from zero to its final value. The initial inlet temperature of the coolant is 200°C.

After switching on the beam power, the mass flow rate of Pb-Bi increases continuously and reaches its maximum after about 20 s. For the system considered the mass flow rate at steady-state conditions is about 33 kg/s. The hot spot in the fluid is located within the guide tube at about 250 mm upstream of the beam window. This temperature maximum (600°C) is reached about 5 s after the switch-on of the beam power. Taking into account the high heat flux on the beam window surface, an excessive temperature of the beam window is expected. However, using the 1D code HETRAF, this cannot be evaluated. 3-D calculations to solve this question are discussed in chapter 2.2.3.3. In order to assure a safe cooling of the MEGAPIE beam window for all operational conditions, a start-up mode with a sudden power increase has to be avoided.

Figure 22 indicates the effect of a finite ramp time of the start-up phase on the fluid temperature transient. Here, a linear increase of the beam power is considered. The ramp time of the start-up phase is defined as the time period during which the beam power is increased from zero to its final value. It is seen that the maximum fluid temperature decreases with increasing ramp time of the start-up phase. With a ramp time of 30 s the maximum fluid temperature is reduced from 600°C for the reference case to 400°C. With increasing ramp time, the maximum temperature is reached at a later time after switching on the proton beam.

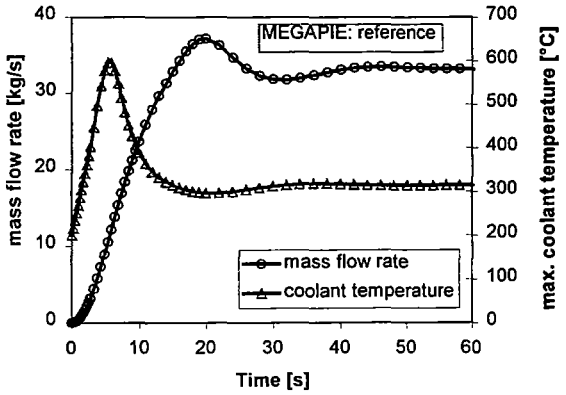

Figure 21: Transient behavior of mass flow rate and coolant temperature.

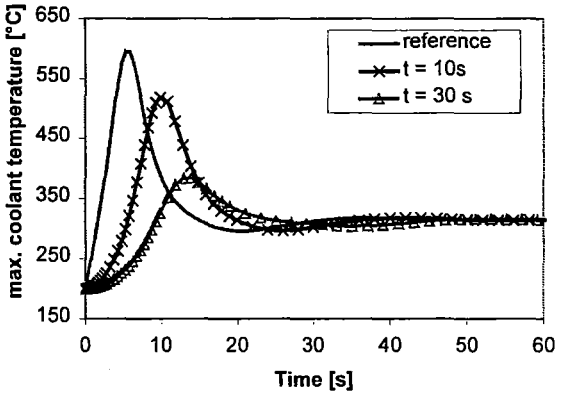

Figure 22: Maximum coolant temperature versus time: effect of the ramp time.

Figures 23 and 24 present the velocity and temperature distribution in the MEGAPIE target with a slanted end of the inner cylinder. The inclination angle to the horizontal is 10°, cf. Figure 20. There is no bypass flow. Due to the non-symmetric geometry, a region of high velocities is observed in the left part of the inner cylinder where the gap size is smaller. A large flow recirculation occurs in the right part, where the gap size is larger. However, flow is stagnant near the center of the beam window. This leads to an excessive temperature of the window surface. Obviously, for the case without a bypass flow, the beam window cannot be cooled sufficiently.

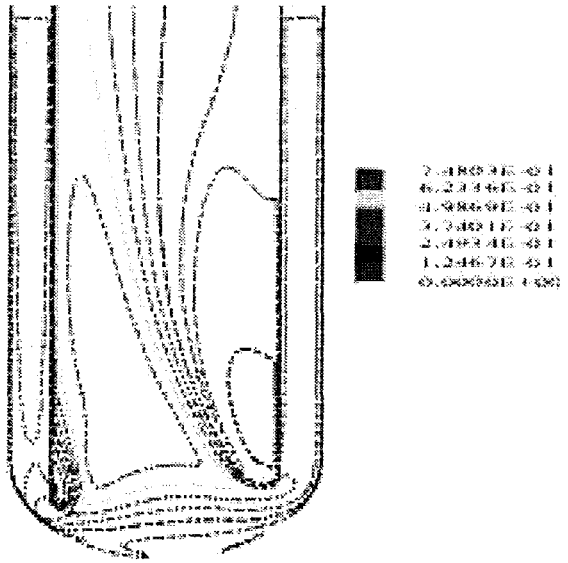

Figure 23: Velocity distribution with a slanted guide tube, without bypass flow.

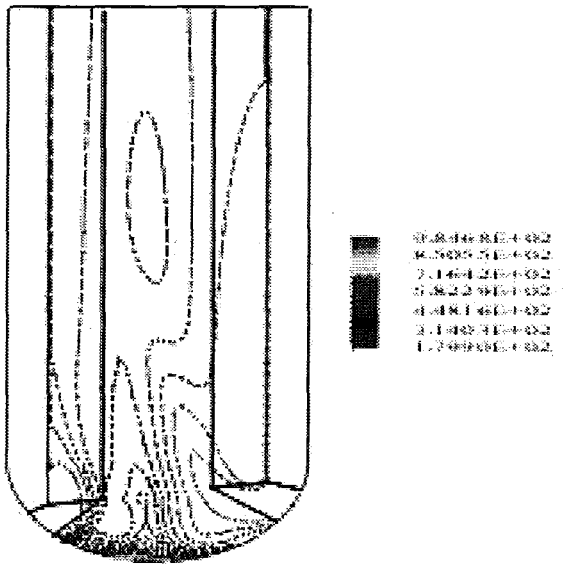

Figure 24: Temperature distribution with a slanted guide tube, without bypass flow.

Figures 25 and 26 show the temperature and velocity distribution in the MEGAPIE target with a bypass flow, being injected through the jet pipe in the left part of the target container, cf. Figure 20. The cross section of the jet pipe is about 59 mm x 5.0 mm. The injection velocity is 1 m/s (9.4% of the main inlet flow rate). It is seen that a region of high velocity near the beam window is generated. The maximum local velocity is about 1.18 m/s, which is still acceptable in order to prevent erosion. Due to the high velocity near the center of the beam window, where the heat deposited by the proton beam has its maximum, the beam window is sufficiently cooled.
The bypass flow penetrates slightly into the opposite side of the annulus, as the main inlet flow rate is low. This can produce large scale eddies in the annulus which cause a non-symmetrical flow distribution in the annulus. In order to investigate this phenomena in more detail, the computational domain in axial direction has to be enlarged, cf. chapter 2.2.3.3.

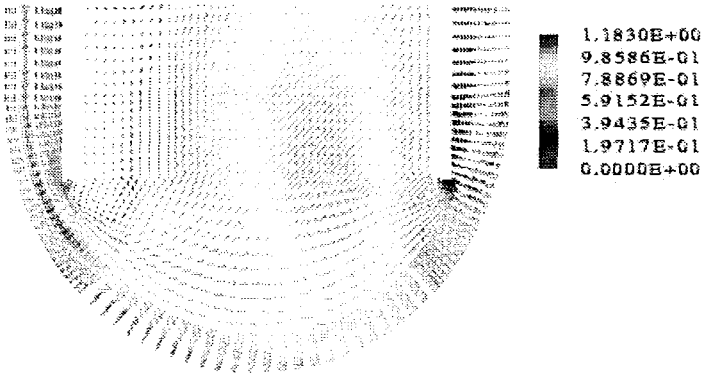

Figure 25: Velocity distribution with a bypass jet.

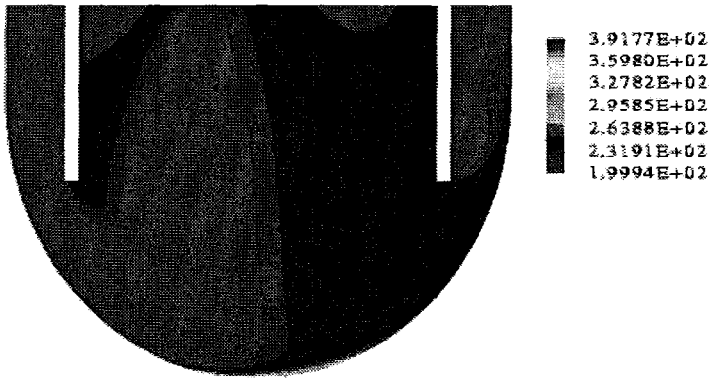

Figure 26: Temperature distribution with a bypass jet.

2.2.1.3 Conclusions

The Forschungszentrum Karlsruhe is involved in the numerical and experimental thermalhydraulic design of the spallation target of an ADS system.
Two computer codes of different specific capabilities have been used for the target design, i.e. the 1-D system code HETRAF and the 3-D CFD code CFX-4.3. In the time period of this report, first, the experimental investigation on the ISTC 559 target has been completed. An optimized geometry, which allows the cooling of the beam window under normal operating conditions, is presented. Second, numerical design studies have been performed for the MEGAPIE target. The presented results for natural convection conditions show that the ramp time of the start-up phase of the proton beam has to be large enough in order to avoid excessive hot spots in the coolant as well as in the beam window. In any case, a ramp time larger than 30 s should be chosen. For the reference design of the MEGAPIE target, a bypass flow via a jet pipe is inevitable in order to sufficiently cool the beam window. A further detailed 3-D numerical analysis combined with model experiments in the HYTAS test facility will make a crucial contribution to the design of the MEGAPIE target, and will improve the available tools to design an ADS relevant spallation target.

2.2.2 Work Package WP2: Fundamental Experiments in Liquid Lead-Bismuth on Heat Transfer and Model Development / Model Validation

2.2.2.1 Instrumentation Development

In the technology loop THESYS fundamental measurement techniques, which have been used with other liquid metals such as sodium Na and sodium-potassium Na-K, will be tested and applied to liquid lead-bismuth.
The following measurement techniques have been or are planned to be applied:

- Thermocouples (temperature),
- Heat Emitting Temperature Sensors (heat flux), Platnieks et al. (1998),
- Electromagnetic flowmeter (flow rate),
- Turbine flowmeter (flow rate), Natec (2000),
- Ultrasonic Measurement Technique (flow rate), Panametrics (2000),
- Miniature Permanentmagnet Flowmeter Probes (velocity), Knebel et al. (1998),
- Ultrasonic Measurement Technique (velocity), Takeda and Kikura (1997).

After the calibration of these measurement techniques in the lead-bismuth environment of the technology loop THESYS, these techniques will be applied to the thermalhydraulic loop THEADES and the corrosion loop CORRIDA, see chapter 2.1.

Thermocouples:

The measurement of the liquid lead-bismuth temperature is done with insulated NiCr-Ni thermocouples, which are sheathed in stainless steel. The diameter is between 0.25 mm and 1.0 mm depending on the required response time of the thermocouple. Because of the high heat transfer coefficients that are characteristic of a liquid metal the frequency response of thermocouples is far higher than in conventional fluids. According to Krebs and Bremhorst (1983) a *0.25 mm* sheathed thermocouple with an insulated junction gives undamped signals in sodium in excess of *40 Hz*.

Heat Emitting Temperature Sensors HETSS:

A device to measure wall heat fluxes, HETSS (Heat Emitting Temperature Sensing Surface), has been developped at the University of Riga, Latvia, Platnieks et al. (1998). A sketch is given in figure 27. A HETSS module consists of many temperature-sensitive resistors (minimum surface area 5 x 5 mm^2) which are adapted to high temperatures. Parallel to the temperature measurement over one module, a defined heat flux can be released by the resistors. Knowing the heat flux and the temperatures of both the wall (HETSS module) and the bulk fluid, the heat transfer coefficient can be determined.
A first calibration curve of a circular HETSS module of 200 mm length is given in figure 28. A linear relationship between electric resistivity and temperature is measured, Dementjev (2000).
A specially manufactured flat HETSS module will be used in order to simulate the beam window heating.

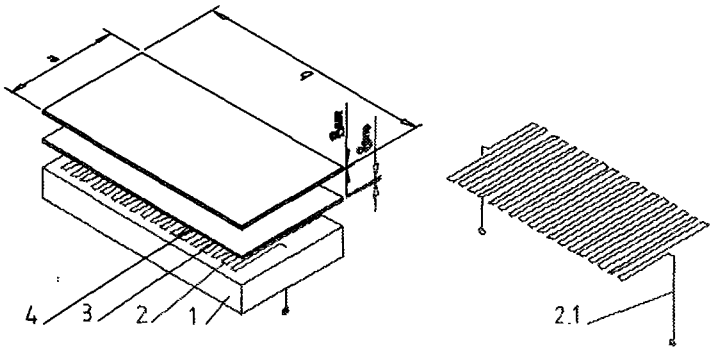

Figure 27: Scheme of HETSS:
1 – substrate,
2 – heater-sensor,
2.1 – current leads,
3 – electrical insulation,
4 – stainless steel screen,
(private communication
S. Dementjev, (2000)).

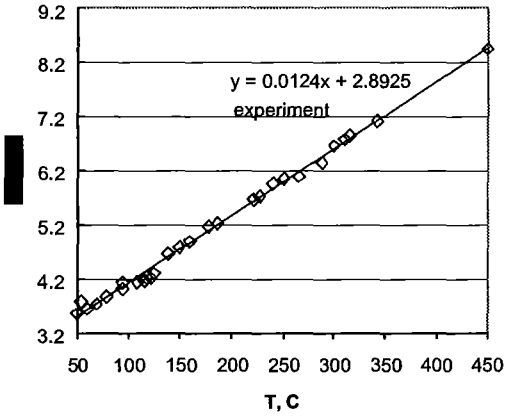

Figure 28: Calibration curve of a circular HETSS module: resistivity versus temperature.

Miniature Permanentmagnet Flowmeter Probes (MPMF-Probe):

The temperature compensated miniature permanent magnet flowmeter probe (MPMF probe) is shown in figure 29. It consists essentially of a stainless steel sheath of outer diameter *2.5 mm* which contains a miniature AlNiCo 450 permanent magnet, of length to diameter ratio *1* and magnetized radially. The measuring principle is based on electromagnetic induction: liquid Pb-Bi flows in a vertical direction through a horizontal magnetic field, generating an electromotive force (emf) which is perpendicular to both the liquid Pb-Bi flow and the magnetic field and proportional to the Pb-Bi velocity. The emf is detected using grounded thermocouples *0.25 mm* in diameter which are welded on the inner surface of the sheath of the probe normal to the permanent magnet poles at the positions *1* and *2* (lower probe plane). The wall thickness of the sheath is *0.1 mm*. Whether this might dampen the thermocouple signal and thus lower the response time has to be investigated in more detail. The emf is measured between two thermocouple wires of the same material that are marked *A* (Alumel), *C* (Chromel) or *S* (stainless steel). The thermocouples are routed inside the probe sheath. If a temperature field is superimposed on the velocity field, a thermoelectric voltage is added to the velocity induced voltage. In order to compensate for the thermoelectric voltage two other grounded thermocouples are installed at positions *3* and *4* (upper probe plane) and these are only weakly influenced by the magnetic field. The distance between the two probe planes is *3.0 mm*. An additional thermocouple of *0.25 mm* diameter at the tip of the probe (position *5*) is used for measuring the mean temperature and the temperature fluctuations. The distance between the thermocouple position *5* and the lower probe plane is *7.2 mm*.

The MPMF probe design allows the simultaneous measurement of the temperatures at the five thermocouple positions and of the three voltages at each probe plane, i.e. U_{21A}, U_{21C}, U_{21S}, U_{43A}, U_{43C} and U_{43S}. The voltmeters used have a resolution of *0.1* μV

and an adjustable integration time of multiples of *10* seconds. The probe responds very rapidly to changes in velocity but long integration times are needed to establish accurate mean values of the very low voltages. The temperature fluctuations are first measured with an integrating RMS-voltmeter which gives the rms values. Then, in a separate measurement, the time history of the temperature fluctuations is recorded over a frequency range from *0.1 Hz* to typically *500 Hz*, the latter figure being chosen because it is sufficiently higher than the frequency response of the probe to avoid a loss of information about the frequency spectrum.
In the following the velocity measurement will be explained briefly (a detailed explanation is given by Knebel and Krebs (1994)). The voltages consist of components depending on the velocity and temperature:

$$U_{21A,C,S} = E_{21} + \left(S_{A,C,S} - S^*_{N21}\right) \cdot \Delta T_{21} \tag{1}$$

in the lower probe plane,

and $$U_{43A,C,S} = \alpha \cdot E_{21} + \left(S_{A,C,S} - S^*_{N43}\right) \cdot \Delta T_{43} \tag{2}$$

in the upper probe plane. E_{21} is the velocity induced voltage in the lower probe plane, α is the ratio of the velocity induced voltages at the two probe planes, $S_{A,C,S}$ are the Seebeck coefficients corresponding to the materials of the thermocouple wires, and ΔT_{21} and ΔT_{43} are the temperature differences in the lower and the upper probe planes respectively. S^*_{N21} and S^*_{N43} are the Seebeck coefficients of the electrically conductive connections between the two thermocouple positions at the two probe planes and these depend on the Seebeck coefficients of the lead-bismuth and the stainless steel and the relative electrical resistances of the paths through the lead-bismuth and the stainless steel. Assuming identical Seebeck coefficients S^*_{N21} and S^*_{N43} the velocity induced voltage E_{21} can be determined by the measurement of four voltages. Equations (1) and (2) for Alumel and stainless steel give:

$$E_{21} = \frac{U_{43A} \cdot U_{21S} - U_{21A} \cdot U_{43S}}{U_{43A} - U_{43S} + \alpha \cdot (U_{21S} - U_{21A})} \quad . \tag{3}$$

It should be noted that Chromel has a very high Seebeck coefficient relative to Alumel and stainless steel and hence the voltages U_{21A}, U_{21S} and U_{43A}, U_{43S} are preferred for the evaluation of the velocity signal instead of U_{21C} and U_{43C} because thermoelectric effects are smaller.
Alternatively the voltage induced by the lead-bismuth velocity may be calculated from:

$$E_{21} = \frac{U_{21A} - K_{AS} \cdot U_{21S}}{1 - K_{AS}} \tag{4}$$

where

$$K_{AS} = \frac{S_A - S^*_{N21}}{S_S - S^*_{N21}} \quad . \tag{5}$$

This means that only two voltages have to be measured to obtain the lead-bismuth velocity but K_{AS} has to be found by calibration.
This MPMF probe has successfully been applied to buoyant sodium jets, Knebel (1993). The sensitivity of the probe is determined by calibration and mean

sensitivities of about $47\ \mu V/(m \cdot s^{-1})$ are obtained for MPMF probes of *2.5 mm* outer diameter. According to Müller and Thun (1977) the spatial resolution of the probe is equal to twice the diameter of the MPMF probe, or *5.0 mm*, although the MPMF probe gives a varying output when moved much smaller distances in velocity gradients. The probe signal reflects the average velocity of the lead-bismuth flowing over it and provided that the velocity distribution across the probe diameter is approximately linear an accurate velocity profile will be obtained. Knebel and Krebs (1994) present a velocity profile for an axial position close to the jet outlet ($x/d = 4$) where the velocity variation is restricted to a radial distance of less than *20 mm*, but the profile is still in good agreement with the theoretical Gaussian curve. The limiting accuracy is on the jet axis where the rapid changes in velocity around the maximum may not be captured fully.
The accuracy of the velocity measurement depends on the zero offsets for the probe signals, which have to be constant for a long time, and on the stability of the voltmeters. Both zero offset and voltmeter drift are small compared with the signal itself. The probe offsets are determined before each measurement by calibration and this procedure gives an accuracy of $\pm 7\%$ for sodium velocities above *0.05 m/s*, even with temperature gradients of more than *10 K/mm*.

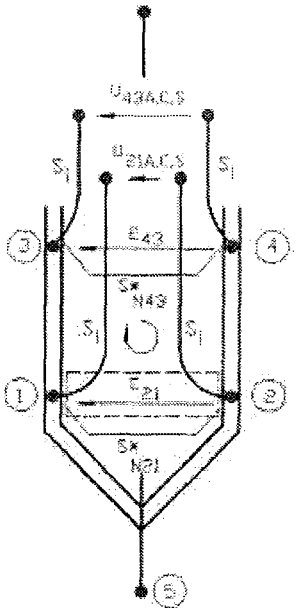

Figure 29: Sketch of the MPMF probe, outer diameter: 2.5 mm.

One prototype of the MPMF probe will be calibrated in the Technology Loop THESYS and applied for velocity measurement, as indicated in figure 30. The MPMF probe and the heater (equipped with a circular HETSS module) can be traversed in x and r direction, respectively, using stepping motors. Experiments will be performed in 2001, as soon as the HETSS module is delivered by the University of Riga.

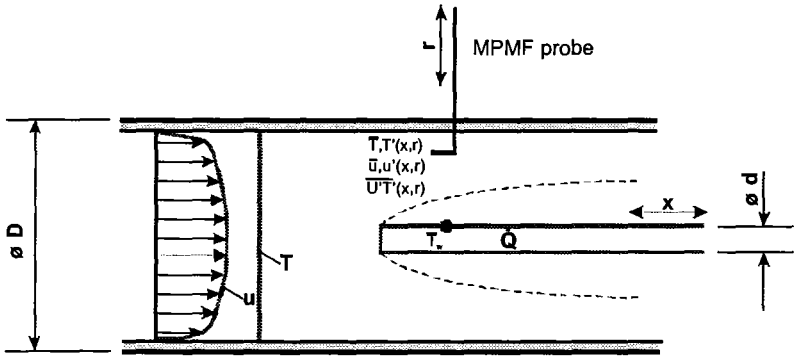

Figure 30: Model experiment on heat transfer and turbulence in the Technology Loop THESYS.

Electromagnetic flow meter:

The knowledge of the flow rate in a loop system is important in order to accurately calculate the characteristic numbers such as the Reynolds number.
Due to the high density of Pb-Bi the application of a gyrostatic flow meter is not possible. Therefore, an electromagnetic flow meter is used. The measurement principle is based on the measurement of an electric voltage which is induced if an electrically conducting fluid flows through an externally applied steady magnetic field. The induced potential U_{ind} can be calculated by

$$U_{ind} = u\,B\,D \quad , \tag{6}$$

where u is the average velocity in the pipe, B the magnetic field strength and D the pipe diameter.

In figure 31 a typical calibration curve of the electromagnetic flow meter in the Technology Loop THESYS is given. There is a perfect linear relationship between induced potential and power supply to the pump. Due to the temperature dependence of the magnetic field, such a calibration has to be done for each operating temperature of the magnet.
According to the partial oxygen pressure in the loop, a thin oxide scale is forming on or is being dissolved from the inner surface of the pipe, cf. chapter 2.4. This changes the electrical conductivity between the liquid Pb-Bi and the structure material of the pipe. As a consequence, the induced potential U_{ind} is changed. Figure 32 illustrates the influence of the partial oxygen pressure (represented by the EMF of the oxygen probe) in the loop on the measured signal at the two electrodes. The influence of the partial oxygen pressure on the voltage of the flowmeter is low, however, this indluence needs further investigations.
In addition, the effect of wettability of the steel surfaces and its influence of the signal of the flow meter has to be analysed in more detail.

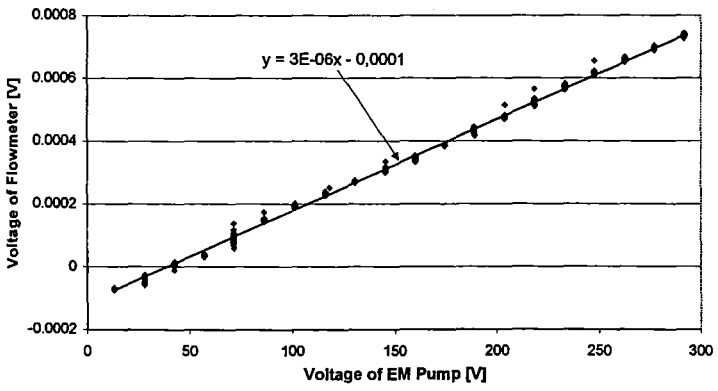

Figure 31: Calibration curve of the electromagnetic flow meter in the Technology Loop THESYS.

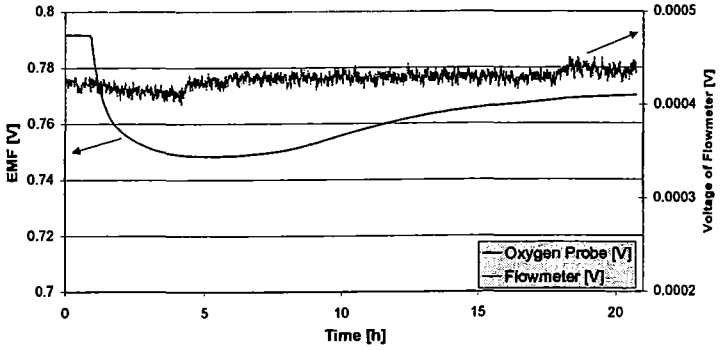

Figure 32: Dependency of the measured voltage of the electromagnetic flow meter (EMF) on the partial oxygen pressure in the liquid lead bismuth.

Turbine flowmeter technique:

The Flow Technology, Inc. Standard Line Turbine Flowmeter is a volumetric flow measuring instrument. A sketch is given in figure 33. The flow sensing element is a freely suspended, bladed rotor positioned axially in the flow stream with the flowing fluid pushing against the blades. The rotational speed of the rotor is proportional to the velocity of the fluid. Since the flow passage is fixed, the rotational speed of the turbine rotors is a true representation of the volume of fluid flowing through the flowmeter. The rotation of the turbine rotor generates electrical pulses in the pickoff which is attached to the flowmeter housing in close proximity to the turning rotor. Each one of the pulses represents a discrete volume of fluid. The frequency or pulse repetition rate represents the volumetric flow rate and the accumulated pulse total represents the total volume measured.
Optimum performance of a turbine meter system depends upon a valid calibration as well as the correct selection of supporting equipment. The rotational speed of a turbine rotor depends upon fluid properties as well as the fluid velocity. The most significant fluid property for a liquid meter is the kinematic viscosity. As liquid viscosity increases, the slip of the turbine rotor due to viscous drag is increased, and the rotational speed and hence the pick-off frequency is decreased.
The turbine meter system, which will be applied to the KALLA loops, is calibrated with a model fluid which has exactly the same kinematic viscosity as liquid lead-bismuth. Thus, an absolute flow measuring technique for Pb-Bi is available for a volume flow rate of up to 6.3 m^3/h. First, the turbine will be installed in the Technology Loop THESYS, in order to compare its performance relative to the other flow measurement techniques described in this chapter.

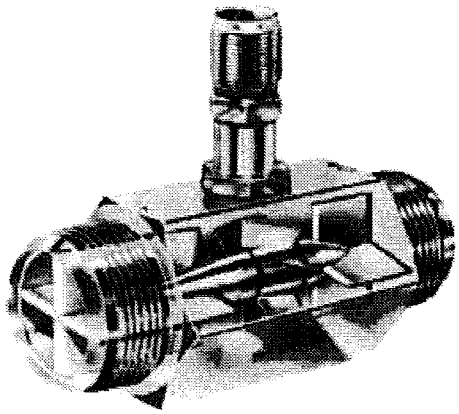

Figure 33: Sketch of the Turbine Flowmeter, Flow Technology (1999).

Ultrasonic measurement technique:

The ultrasonic measurement technique can be applied both for integral flow rate measurement (ultrasonic transit-time method) and for local velocity measurement (ultrasonic Doppler method).
In the first method the transit-time of an ultrasonic wave travelling simultaneously through a flowing medium both in upstream and in downstream direction is measured. The flow velocity is calculated from the time difference that arises over the two signal paths (figure 34a).

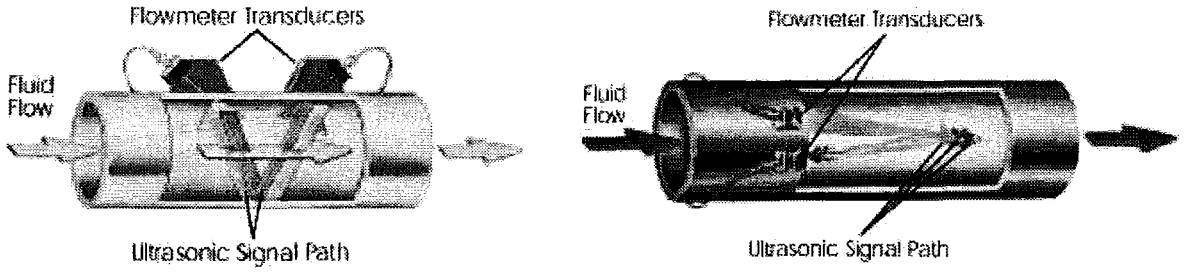

Figure 34: Signal path for (a) ultrasonic transit-time method and for (b) ultrasonic Doppler method.

The second method uses the Doppler frequency shift, arising from the reflection of the transmitted ultrasonic wave at particles (impurities, gas bubbles, etc.) within the flowing medium, to calculate a velocity profile (figure 34b). Only the velocity component parallel to the path of the ultrasonic wave is measured.
The limiting factor for this measurement technique is the fluid temperature. The working range of available high temperature transducers reaches up to temperatures of 150°C (long-term applications) or 200°C (short-term applications). To extend the temperature range a technology known as Bundled Wave Guides from Panametrics (Panametrics (2000)) will be installed at the Technology Loop THESYS. A Bundled Wave Guide consists of a multitude of thin tubes which are guiding the ultrasonic wave into the medium and which decouple the hot fluid side from the cold transducer side of the Bundled Wave Guide. The decoupling is done by cooling the top side.
The introduction of the ultrasonic measurement technique will provide a reliable flow rate measurement, which is essential for the operation and the control of a Pb-Bi loop system.

2.2.2.2 Heat Transfer Experiment

Introduction:

In order to do an adequate design of thermally highly-loaded surfaces (e.g. beam window, fuel rod) or heat transfer components (e.g. heat exchanger, steam generator), the knowledge of the convective-diffusive heat transport phenomena in laminar and turbulent liquid metal flow is needed. Due to the low Prandtl number of liquid metals being usually of the order $O(10^{-1}\text{-}10^{-2})$, numerical calculations may sometimes lead to misconceptions in the design, especially in the weakly turbulent Reynolds number regime, where buoyancy plays a non-negligible role. For the liquid metal flow the viscous and the thermal length scales separate and the normally used constants of the k-ε turbulence model lead to considerable differences to experimentally obtained values. Moreover, in most technical applications the flows are thermally developing so that the heat exchange through the boundary layer plays a significant role.
Here, an experimental and numerical study of the heat transfer charactersitics of a thermally developing liquid metal flow in a rectangular duct with thin steel walls is investigated. The fluid used is the eutectic sodium-potassium alloy $Na^{78}K^{22}$ owing a Prandtl number of Pr=0.02. Both, the integral quantities like the Nusselt number Nu as well as the local quantities (temperatures at the fluid-wall interface, temperature within the fluid) are measured. The parameter field investigated is covered in the following parameter range:

- Reynolds number Re : $2{\cdot}10^3 \leq Re \leq 1.3\text{x}10^5$
- Peclet number Pe : $6.10^1 \leq Pe \leq 2.9\text{x}10^3$.

The heat transfer experiments were performed using NaK as fluid instead of PbBi, as the influence of boundary conditions such as oxygen partial pressure in the liquid metal, wetting and temperature have a significant effect on the flow rate, which is measured using an electromagnetic flowmeter in the Technology Loop THESYS of KALLA. As soon as the absolute value of the flow rate can be measured in a reproducible way, the heat transfer experiments will be performed with PbBi as fluid.
As the molecular Prandtl number of NaK (Pr = *0.02* at *50°C*) and PbBi (Pr = *0.045* at *400°C*) differ only by a factor of about 2, the transferability of the presented experimental and numerical results from NaK to PbBi is given. The requested experiments in PbBi will be done within 2001.

For the heat transfer experiment, a liquid metal flow in a rectangular duct is considered, which is exposed to a heat source being perpendicular to the side walls, as shown in figure 35. The heat flux q produced by a radiation heater can attain values up to 25 Wcm^{-2}.
In most technical applications the flow is thermally developing before reaching the outlet of the heated section. Similarity considerations yield that the thickness of the thermal boundary layer δ scales with $\delta \sim Pe^{-1/2}$. Consider now a duct flow with a Peclet number $Pe = 10^4$ and duct dimensions of approximately 0.1 m in the geometry shown in figure 35. If the Peclet number is scaled with the heated length, namely the x-coordinate, the flow is thermally developed if the thermal boundary layer has reached the opposite side. This results in a thermal development length of O(10m)! This simple estimate demonstrates the necessity for the detailed study of thermally developing flows.

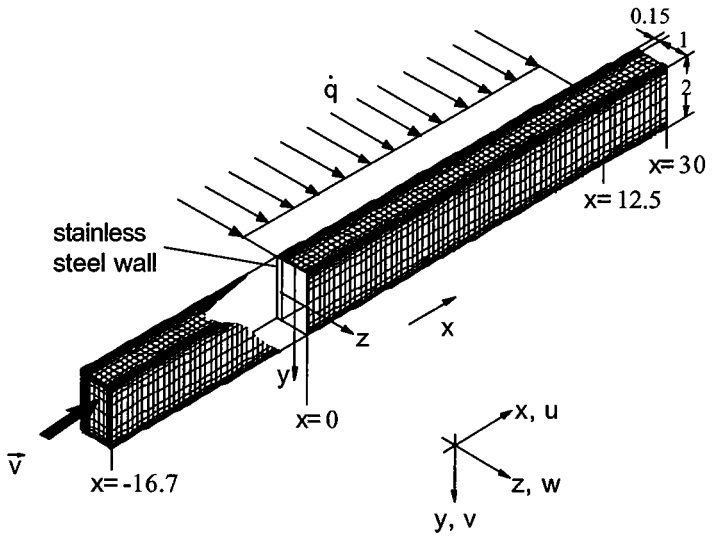

Figure 35: Schematics and coordinate system of the duct studied. The mesh shows the computational mesh being used in the numerics.

Numerical simulation and Experimental setup:

The calculation of the heat transfer in a laminar flow has been performed completely three-dimensional using the commercial program package *FIDAP*. A non-equidistant mesh has been generated in the *yz*-plane, as shown in figure 35, whereas the grid in flow direction is equidistant. The number of grid points per unit length used in the coordinate direction *x, y* and *z* of the fluid domain are 16, 32 and 16. Since the heat conductivity of stainless steel and the fluid is of similar magnitude, heat can be transported within the wall in flow direction and opposite to it. In the experimental setup the ratio is $\lambda_{steel} / \lambda_{NaK} = 0.684$. Due to this $O(1)$ ratio the fluid is especially heated upstream by the upstream heat diffusion within the wall. Thus, the temperature in plane x=0 is not zero especially for low *Pe* and *Re* numbers. This leads to the following two consequences:

- The computational domain exceeds the heated region from $0 \le x \le 12.5$. In order to keep the calculation time in limits the computational domain chosen is $-16.7 \le x \le 30$.
- Since the wall contributes to the heat conduction in all directions, the walls are integrated in the calculation with the same mesh discretisation in *x, y* direction as in the fluid domain. In *z*-direction only 3 equidistant spaced grid points are used.

Due to the restricted storage capacity of the used work station (about 125MB RAM) the flow domain has been split-up into three parts, which overlap each other by two characteristic lengths *a*. As inlet condition for the test part (flow domain 2) from $-3 \le x \le 15.5$ the results obtained for flow domain 1 are used; the same holds for flow domain 3.
First the laminar flow is considered. The flow was assumed to be of slug flow type at $x = -16.7$. The dimensionless temperature there was chosen to be zero. At all walls the non-slip condition is applied and all walls except for the heated regions have been assumed to be adiabatic.
In the turbulent flow the situation is somehow more difficult. The calculation presented for the turbulent flow is based on the κ-ε-turbulence model with a standard set of the turbulent constants given by Rodi (1985). The choice of these constants may be problematic in the turbulent flow regime for $Re \le 10^4$ because buoyancy

effects cannot be neglected in the experiment in that regime. However, the physical effects leading to disagreements between experimental and theoretical results will be highlighted in the discussion. Finally, the distribution of k and ε at the inlet (x = -16.7) are $k = 5 \cdot 10^{-3}$ and $\varepsilon = 5 \cdot 10^{-3}$ over the whole ducts cross-section except for the wall region. The chosen values for k and ε assume homogeneous turbulence as proposed by Rodi (1985) assuming a homogeneous grid turbulence. This assumption is justified for the investigated test sections, because at the inlet a flow straightener is installed.

The experiments have been performed in the MEKKA-facility of Forschungszentrum Karlsruhe. Here only a brief overview of the experimental facility is given. A more detailed description may be taken from Barleon et al. (1996).

A centrifugal pump with a pressure head of 0.9 MPa at a flow rate of 22 m^3/h circulates the eutectic sodium-potassium alloy $Na^{78}K^{22}$ (melting point –11°C) at temperatures below 250°C. The thermophysical properties of this alloy have been described in detail by O'Donell et al. (1989). In the investigated temperature range ($T \approx 50$°C) NaK has a Prandtl number of Pr = 0.024. An additional electromagnetic pump is used for the high temperature wetting procedures above 250°C and also for very low flow rates. During a wetting procedure at 350°C impurities on the steel surface, such as oxygen or alloy components are dissolved in the NaK and extracted by cold traps. The dissipated energy is removed by an oil-cooled double tube heat exchanger.

The flow rate is measured simultaneously by a gyrostatic mass flow meter and by an electromagnetic flow meter in order to have two independent measurement principles. Both agreed throughout the measurements with an accuracy of 0.5%.

The test channel has a rectangular cross-section with an aspect ratio 2:1 and a characteristic length of a = 40 mm. A sketch with all dimensions scaled with a is shown in figure 35. All walls consist of stainless steel, which are welded by electron beam welding. The walls being perpendicular to the heat flux are 1 mm thick, whereas walls facing the radiation heater consist of 6 mm thick plates. Twelve thermocouples are embedded in the side wall in groves directly at the fluid-wall interface at three different axial positions, namely at the entrance of the heater (S1 at x = 0), in the middle of the heated section (S2 at x = 6.25) and also at the outlet of the heated section (S3 at x = 12.5). These thermocouples are counted as an array $T_{mn,i}$, where the first index denotes the axial position in x-direction (S1, S2 or S3). The second index n specifies the location in y-direction (1,2,3 or 4) and the subscript i indicates a sensor at the fluid-wall interface. A similar set of 12 thermocouples is embedded in the side walls at the outside facing the radiation heater. The numbering is analogous to the fluid-wall thermocouples with the exception of the index o instead of i indicating that these sensors are located at the outside. The exact spatial location and the definition of the indices may be taken from figure 36a. All thermocouples have an outer diameter of 0.5 mm and are made of the pairing copper-constantan.

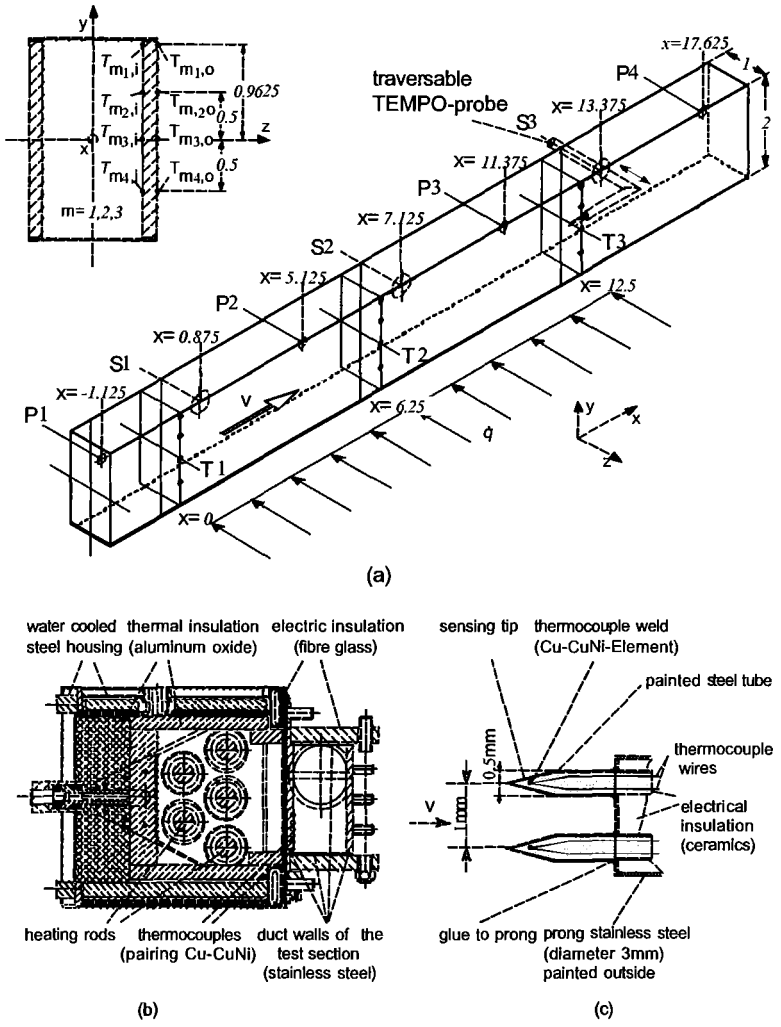

Figure 36: a) Geometry and location of the measurement positions of the test section. The thermocouples imbedded at the fluid-wall-interface are marked by i. The TEMPO probe is traversed in the plane y=0 at S1 (x=0), S2 and S3.
b.) Cut through the radiation heater with the attached test section.
c.) Sketch of the TEMPO probe.

All quantities furtheron discussed in the following paragraph are dimensionless in order to satisfy a transferability of the experimental and numerical results. The dimensionless velocity v, the time t, the pressure p, the temperature difference Θ are scaled with the mean flow velocity v_0, a/v_0, $\rho\, v_0^2$, $(q\, a)/\lambda$, respectively. ΔT is a characteristic temperature difference. Here, ΔT is the difference between the average inlet temperature and the average temperature at the measurement position. The heat flux applied is denoted by q. For simplicity a non-buoyant flow is considered so that the molecular properties of the liquid like the density ρ, the kinematic viscosity ν, the heat capacity cp and the heat conductivity λ are constant with respect to space and time. As a result of this assumption the temperature Θ acts like a passive scalar. The scaling leads to the following dimensionless groups as the Reynolds number $Re = v_0 a/\nu$, Peclet number $Pe = v_0 a/\kappa$, Prandtl number $Pr = \nu/\kappa$, where κ is the heat diffusivity.
Figure 36b gives a cut through the radiation heater with the attached test section, figure 36c gives a sketch of the TEMPO probe which is used for temperature measurements. Further technical details may be taken from Barleon et al. (1996).

Results:

All commonly used heat transfer correlations contain a pressure drop relation, which takes into account the momentum transport. The pressure drop relations mostly indicates the degree of turbulence (Blasius or Prandtl type) within the duct and thus describes integrally the turbulence structure. Here, a forced convective flow is investigated. Therefore, the temperature distribution within the fluid depends mainly on the velocity and turbulence structure within the liquid.

Figure 37 shows the dimensionless temperature within the duct as a function of the transverse coordinate z for a weakly turbulent Reynolds number of *Re* = 2493. A remarkable difference between the numerical and experimental results appears. At the Reynolds number investigated in the flow buoyancy effects play a significant role. If one calculates the relevant Grashof number Gr ($Gr = (\Delta\rho\ g\ d^3)/(\rho\nu^2)$) a value of $3.05 \cdot 10^8$ is obtained, which is already in the unsteady turbulent buoyant convection regime. An attempt to incorporate buoyancy effects into simulation yielded the dashed line, which is closer to the experimental values. Nevertheless, the dimensionless temperature calculated is overestimated by a factor of 1.6. Thus, the real heat transfer is much better. The remaining difference between simulation and experiment clearly shows that in the mixed convection regime conventional turbulence models lead to miscellaneous results.

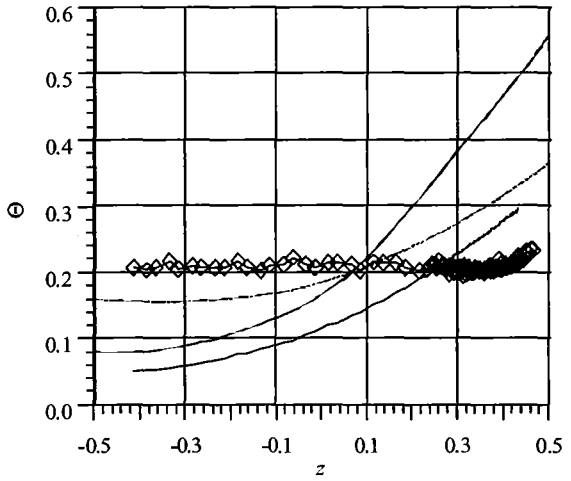

Figure 37: Temperature Θ as a function of z in the plane y=0 at x=12 in a flow with Re=2493. The line (---) indicates the computational values neglecting buoyancy, the dashed marks the calculated values with buoyancy.

The discrepancies between experiment and simulation rapidly diminish for increasing Reynolds numbers, as the figures 38 show. There also the dimensionless temperature is plotted as a function of the coordinate z. For Reynolds numbers higher than $Re = 1.8 \cdot 10^4$ a nearly perfect agreement between the simulation and the experiment was found.

The temperatures at the fluid-wall interface serve from an engineering point of view the most interesting results since the results obtained there determine the achievable heat flux removable from the wall. As described in the introduction most heat transfer problems are thermally developing. Unfortunately, for such developing flows of fluids with low Prandtl numbers no heat transfer correlations are given in engineering textbooks. In technical systems usually the correlations for thermally fully developed flows are used as a conservative assessment, because the Nusselt numbers in developing flows are higher than in already developed flows. The Nusselt number Nu is the inverse of the dimensionless interface temperature Θ, i.e. $Nu = 1/(T_{Wall}-T_{bulk})$.

In the figures 39 a-f the dimensionless fluid-wall interface temperatures $\Theta_{m3,i}$ of a liquid metal flow in the plane y = 0 are plotted as a function of x for several Reynolds

numbers Re. Both, the calculated and the experimental results reveal that the upstream heat flux in the structural material for each Reynolds number leads to a temperature at x = 0 different from zero. This effect decreases as *Re* increases because the heat removal from the wall grows with higher velocities. The reason for the upstream heating of the fluid is that the heat conductivities of the fluid and the wall and the wall are comparable.
The fluid-wall interface temperatures $\Theta_{m3,i}$ for a laminar flow in the experiment agree qualitatively with the numerically calculated values, see figure 39 a. Quantitatively, however, deviations of about 25% are found. As previously discussed these deviations originate from buoyancy effects present at low Re. As *Re* increases, the fluid-wall interface temperatures decrease both due to the higher average flow velocity and due to the turbulent transport of heat towards the core of the flow. Nevertheless, the interface temperatures calculated with the k-ε-model and the adapted standard constants agree rather well with the measured values throughout the whole Reynolds number range investigated.

Conclusions:

The presented experimental results give a detailed and broad database on heat transfer along a thermally highly-loaded surface which is cooled by a liquid metal. For these experiments buoyancy effects are of no influence to the flow and the temperature field. The data set available can be used for physical model development and improvement and, consequently, for numerical code validation.
The comparison between the numerical calculation, which applies a k-ε turbulence model with constants that are adapted to low Prandtl number fluids, and the experiment shows significantly better heat transfer characteristics in the weakly turbulent Reynolds number regime ($Re \leq 1.8 \cdot 10^4$) for the calculation. The dimensionless fluid-wall interface temperatures, which correspond to the inverse of the Nusselt number, are by a factor of nearly two lower than numerically predicted. If the thermal wall conductivity is taken into account in the numerical simulation, a reasonably well agreement in all flow quantities is found between experiment and calculation for Reynolds numbers exceeding $1.8 \cdot 10^4$. The deviations between calculation and experiment are below 10-15%.

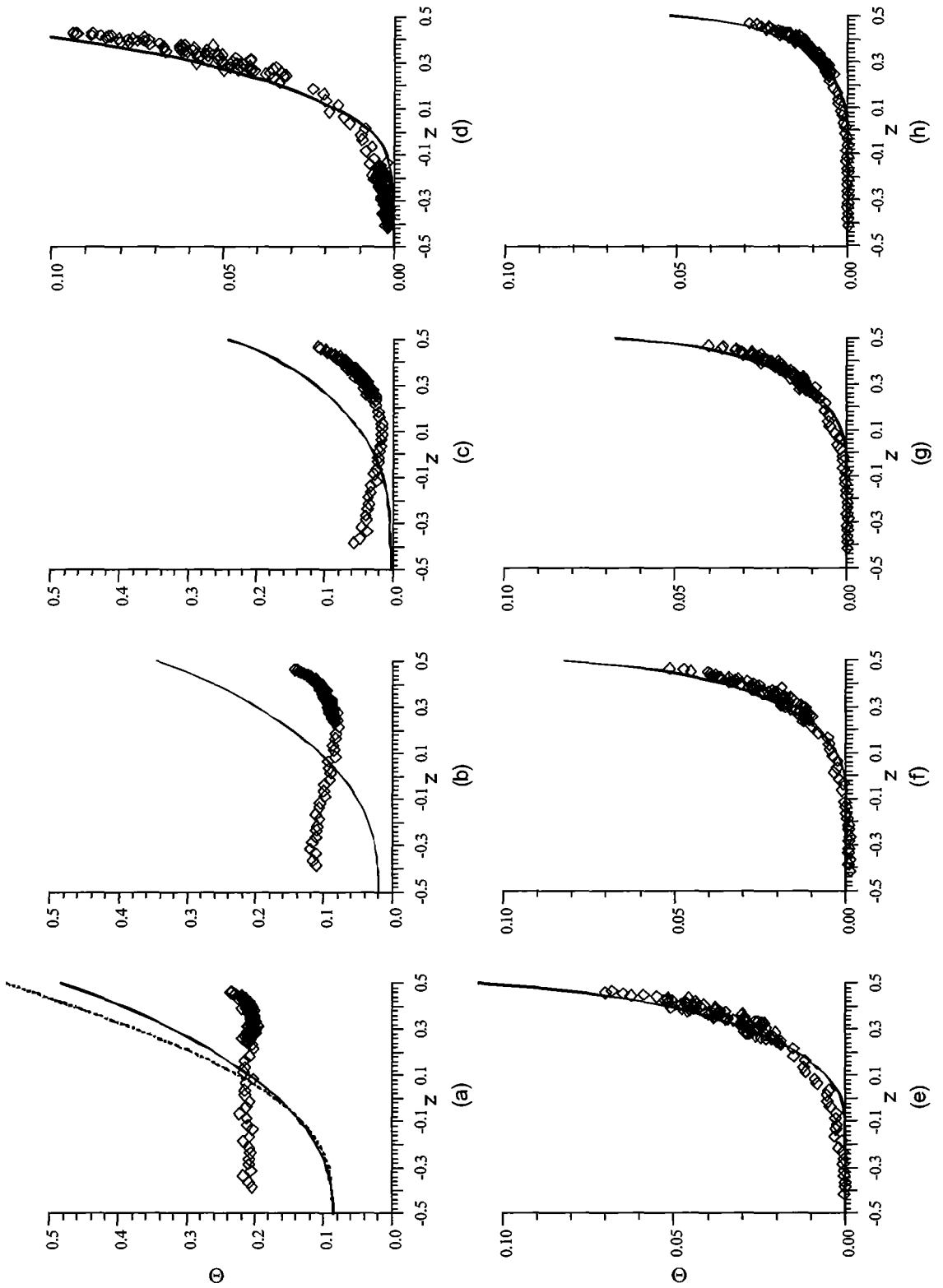

Figure 38: Temperatures Θ as a function of z in the plane y=0 for different *Re*. The lines indicate the calculated temperature values. The dashed line in graph (a) denotes the calculation for a laminar flow. (a) Re=2673; (b) Re=4763; (c) Re=9173; (d) Re=18046; (e) Re=37481; (f) Re=57956; (g) Re=77190; (h) Re=119600.

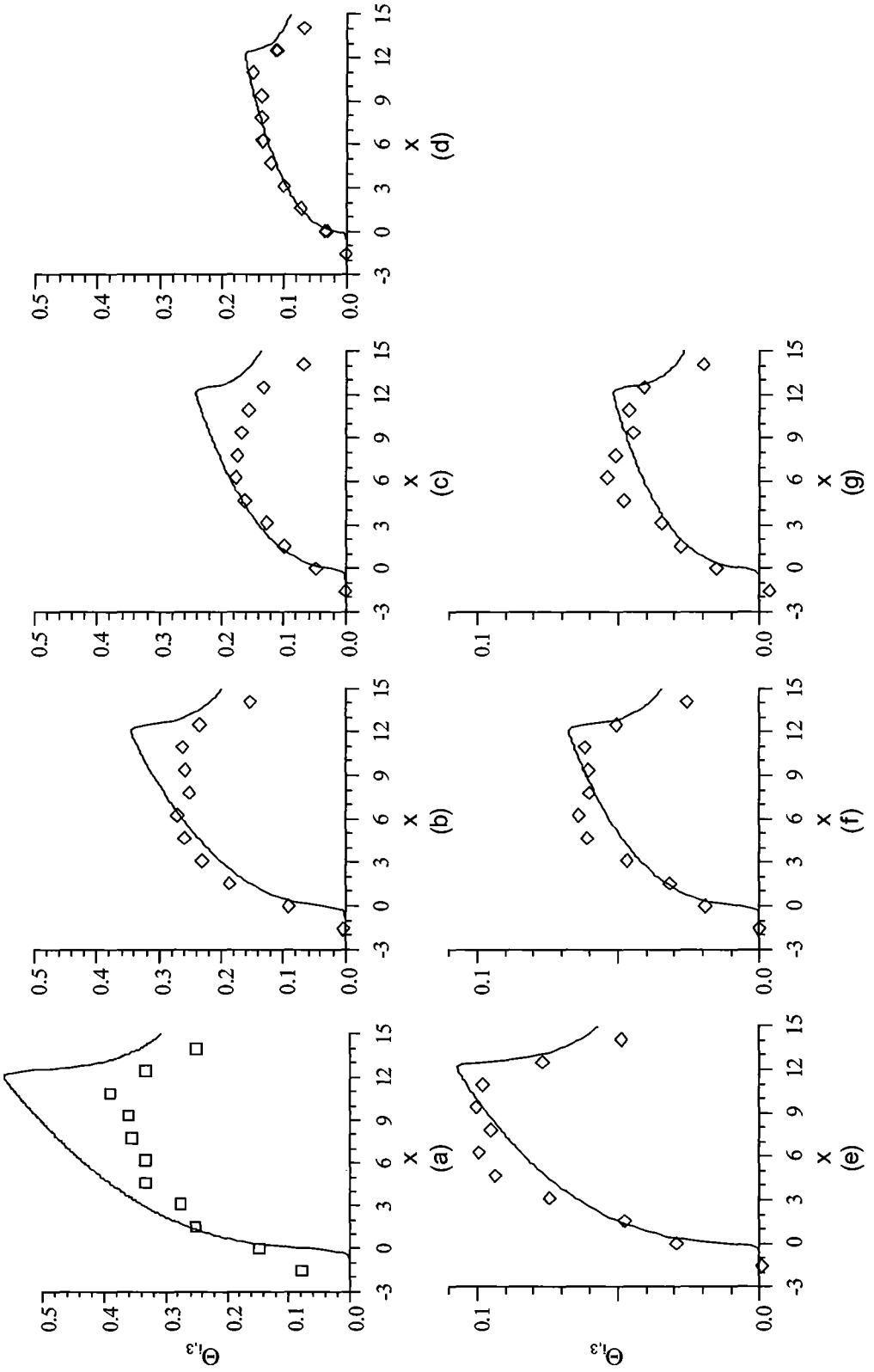

Figure 39: Fluid-wall interface temperature $\Theta_{m3,i}$ in the plane y=0 as a function of x for a hydrodynamic turbulent flow. The lines (-) indicate the values calculated with the k-ε model. (a) Re=2273, (Pe=59); (b) Re=4763, (Pe=121); (c) Re=9173, (Pe=240); (d) Re=18046, (Pe=488); (e) Re=37481, (Pe=962); (f) Re=77719, (Pe=1913); (g) Re=119060, (Pe=2816).

2.2.2.3 TEFLU Benchmark

Introduction:

The temperatures in the structures of a spallation target reach critical values at the beam window. In order to determine these structure temperatures accurately, turbulence models are required to predict the temperature field in the cooling fluid. Standard turbulence models, which are used in commercial codes, are not suitable for the adequate simulation of turbulent heat transfer in heavy liquid metal flows, with buoyancy effects being important: the models using a turbulent Prandtl number to describe the turbulent heat transport assume the Reynolds analogy between the turbulent transport of momentum and heat. This assumption is not valid for liquid metals because the momentum field is mainly turbulence dominated and has only thin wall layers governed by molecular viscous forces, whereas the temperature field is less turbulence dominated and has thick wall layers governed by molecular conduction.
Improved turbulent heat transfer modeling for liquid metals requires more sophisticated measures, than are usually applied for momentum transfer. This means that additional transport equations have to be used which characterize the statistics of the temperature fluctuations. In Knebel al al. (2000) the TMBF turbulence model is described, which consists of a combination of a low–Reynolds number k-ε model and a second order 5–equation heat flux model (Carteciano (1996)). Certain model extensions for liquid metal flows are reported which were developed based on the analysis of data from direct numerical turbulence simulations (Carteciano et al. (1999)).
The objective of the last year activity was to investigate in more detail the advantages of the extended TMBF model and possible necessities for additional model extensions. For this purpose, a heated turbulent sodium jet was chosen by the Benchmark Working Group in order to test the capabilities of CFD codes at simulating liquid metal turbulent flows with heat transfer. The corresponding experiments were performed in the test facility TEFLU at Forschungszentrum Karlsruhe (Knebel (1993)). Three different flow regimes being a forced jet, a buoyant jet, and a plume are considered for the TEFLU Benchmark (Maciocco (2000)).
The FLUTAN calculations (Carteciano and Grötzbach (2001)) are performed using two different turbulence models: the standard k-ε-σ_t model and the TMBF model. The calculations with the k-ε-σ_t model are performed using the standard value for the turbulent Prandtl number σ_t=0.9. The results are compared with experimental data in order to show how the TMBF improves the k-ε-σ_t model and to show the limits of applicability of an eddy diffusivity approach to liquid metal flows. In addition results are deduced from the TMBF calculations on the spatial distribution of the turbulent Prandtl number σ_t which are required to approximate the experimental temperature field with a k-ε-σ_t model.

The TMBF Turbulence Model:

The TMBF model is a combination of a first-order 2-equation model for the turbulent transport of momentum and of a second-order 5-equation model for the turbulent transport of heat. The turbulent stresses are calculated assuming an isotropic eddy viscosity and solving the transport equations for turbulent kinetic energy k and for its dissipation rate ε. The three turbulent heat fluxes $\overline{u_i T'}$ are determined by means of transport equations for these quantities. Moreover, transport equations for the

variance of temperature fluctuations $\overline{T'^2}$ and its dissipation rate ε_T are used in the description of the turbulent transport of heat. In order to extend the range of the TMBF model to low Peclet numbers, new model relationships have been developed (Carteciano et al. (1999)) based on the direct numerical simulations by Wörner and Grötzbach (1997) and analyses by Ye et al. (1997). The TMBF model does not introduce six additional transport equations for the turbulent stresses and thus differs from the so-called Reynolds stress model. However, the calculated turbulent stresses and heat fluxes are no longer related to one another by a fixed turbulent Prandtl number σ_t and are therefore not limited by the Reynolds analogy. The extended TMBF model has been implemented in the FLUTAN computer code and has been validated by means of experimental data from turbulent flows in forced, mixed and natural convection (Carteciano et al. (1997) and (1999)).
The extended TMBF model contains seven transport equations and 17 empirical coefficients. The standard set of empirical coefficients (Table 2) from Gibson and Launder (1978) and Nagano and Kim (1988) is used here.

Table 2: Standard set of empirical coefficients in the extended TMBF model.

k-tr.eq.		ε-tr. Eq.		$\overline{U_j'T'}$-tr. eq.		$\overline{T'^2}$ -tr.eq.		ε_T-tr.eq.	
coeff.	value	coeff.	value	coeff.	value	coeff.	value	coeff.	value
σ_k	1.0	σ_ε	1.3	c_{TD}	0.11	c_{TT}	0.13	c_{DD}	0.13
c_μ	0.09	$c_{\varepsilon 1}$	1.44	c_{T1}	3.0			c_{D1}	2.2
		$c_{\varepsilon 2}$	1.92	c_{T2}	0.33			c_{D2}	0,8
		$c_{\varepsilon 3}$	0.8	c_{T3}	0.5			c_{P1}	1.8
				c_{T4}	0.5			c_{P2}	0.72

TEFLU Experiments:

The experiment of a buoyant turbulent sodium jet was performed in the test facility TEFLU. A sketch of the test facility is shown in Figure 40. The test section consisted of a containment pipe of D = 110 mm diameter and a multi-bore jet block which has 158 bores of d = 7.2 mm diameter, placed on a triangular pitch of 8.2 mm. The length to diameter ratio for individual bores is 16.7.
Sodium was injected into the central bore at a higher temperature ΔT_j and a higher velocity ΔU_j relative to the co-flow through the other bores. By modifying ΔT, ΔU, and the co-flow velocity, three different turbulent flow regimes were experimentally investigated: a forced jet, a buoyant jet, and a plume regime, see Table 3. The Reynolds number Re_{cf} is calculated using the co-flow velocity and the outer diameter D. Re_j is calculated using the maximum value of the velocity at the exit of the jet and the bore diameter d. The value of the densimetric Froude number Fr_j at the exit of the jet block determines the flow regime. Radial profiles of mean velocity, mean temperature and variance of temperature fluctuations were measured at several axial positions downstream of the jet block.

$$Re_{cf} = \frac{u_{cf}\, D}{\nu} \quad \text{and} \quad Re_j = \frac{u_j\, d}{\nu} \tag{7}$$

$$Fr_j = \frac{\rho_0 \left(\overline{u}_j^{\,2} - \overline{u}_{cf}^{\,2} \right)}{g(\rho_{cf} - \rho_j)\, d} \tag{8}$$

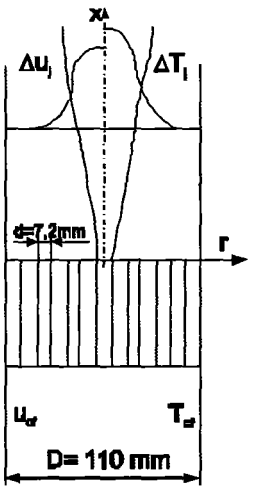

Figure 40: Sketch of a buoyant turbulent sodium jet downstream of a multi-bore jet block.

Table 3: Experimental conditions.

Experiment	$\bar{u}_{cf}$ (m/s)	$\bar{T}_{cf}$ (K)	Re_{cf}	$\Delta\bar{u}_j$ (m/s)	$\Delta\bar{T}_j$ (K)	Re_j	Fr_j
a) forced jet	0.05	573	1.4×10^4	0.50	30	1.01×10^4	521
b) buoyant jet	0.1	573	2.8×10^4	0.33	25	7.9×10^3	365
c) plume	0.1	573	2.8×10^4	0.17	75	4.96×10^3	43.1

Case Specifications:

A two-dimensional numerical grid composed by 19,200 cells (64x1x300) using a cylindrical geometry is sufficient in order to obtain a grid independent solution. In fact, the same results were obtained using a finer grid than this one. The same grid is used for all three regimes. It simulates the fluid domain downstream the jet block starting from the plane x/d = 6 up to x/d = 40. By using symmetry conditions only half of the tube is recorded, from the axis to the wall. The mesh size of the grid changes from 0.36 mm to 1.44 mm in radial direction and from 0.72 mm to 2.88 mm in axial direction.

The inlet profiles for mean velocity, mean temperature, and variance of temperature fluctuations were determined from measured values. The inlet profile for k and ε given by the benchmark proposal were derived using similarity considerations from experimental results in air (Maciocco (2000)). The inlet profiles for ε_T and for the turbulent heat fluxes $\overline{u_i'T'}$ were calculated using the following empirical relationships (Carteciano (1996)):

$$(\varepsilon_T)_{inl} = \left(\overline{T'^2}\varepsilon/k\right)_{inl} \quad \text{and} \tag{9}$$

$$\left(\overline{u_x'T'}\right)_{inl} = -0.1(\partial T/\partial x)_{inl} \tag{10}$$

A very low value for the convergence criterion parameter was chosen: $\varepsilon_3 = 10^{-7}$. The steady state is reached when the change of each velocity component divided by the maximum velocity magnitude and the change of the enthalpy divided by the maximum enthalpy value in the entire field is less than ε_3. The calculations were performed with the first order upwind discretization method for the convective terms in the momentum, energy, and turbulence equations. A first order time discretization was used with $\Delta t = 0.1$s. The system of transport equations is solved by a direct GAUSS-Solver.

Results:

The TMBF and the k-ε-σ_t model can adequately simulate the turbulent transport of momentum using the standard values of the empirical coefficients for the buoyant jet and for the plume regime. However, the value of c_μ must be reduced to 0.06 in the case of the forced jet in order to damp the well known attitude of the k-ε model to overestimate the rate of spread of an axisymmetric jet, Figures 41 to 44 (Rodi (1980)). The fact that the TMBF simulates the same velocity field as calculated by the k-ε-σ_t model signalizes that the temperature influence on the velocity field by means of the turbulent transport of heat is negligible even in the case of the plume regime. In fact, both models describe the turbulent transport of momentum using the same transport equations of k and ε. The only difference in this description is in the model of the buoyancy term which is obviously of negligible order in all the calculations.

The TMBF is a significant improvement in comparison to the k-ε-σ_t model in the simulation of the turbulent transport of heat (Figures 45 to 47). The TMBF can reproduce the mean temperature field well by using the standard values of empirical coefficients in all experiments. This good agreement is due to the separate treatment of the turbulent transport of heat and momentum in the TMBF using the transport equations for the three heat fluxes instead of using the isotropic Fourier assumption.

In contrast, the k-ε-σ_t model cannot accurately simulate the mean temperature field when the standard turbulent Prandtl number is used. As a result of a strong anisotropy in the field of the temperature gradient which shows very high values perpendicular to the flow direction, the turbulent heat flux acting perpendicular to the flow direction has very high values as they are calculated being proportional to the temperature gradient according to the Fourier assumption. For this reason the k-ε-σ_t model shows an unsatisfactory simulation of the turbulent heat fluxes overestimating the values calculated from the TMBF model.

The k-ε-σ_t model can give a good simulation only by adjusting the value of σ_t reducing the turbulent heat flux acting perpendicularly to the flow direction. The fields of σ_t can be calculated by the TMBF model. They represent approximate values because σ_t is calculated using the turbulent heat fluxes, which are modelled by transport equations, and the turbulent shear stresses, which are modelled like in the k-ε model by velocity gradients. The calculated fields show that the turbulent Prandtl number depends not only on the fluid but also on the flow regime and on the position (Figure 48).

From the turbulent Prandtl number distributions it is obvious that the influence of the overestimation of the turbulent radial heat flux on the temperature field by the k-ε-σ_t model is negligible in the plume regime due to the high turbulent conductivity λ_t. In all three flow regimes the turbulent conductivity is lower than the molecular one. The turbulent heat transport by becomes less and less important compared to the molecular one when going from the forced to the plume regime. This can explain the acceptable simulation of the temperature field performed by the k-ε-σ_t model in case of the plume regime.

The TMBF properly simulates the variance of temperature fluctuations $\overline{T^2}$ in all experiments with the exception of the plume regime (Figures 49 to 50). Due to the use of a transport equation for $\varepsilon_{T'}$ a local non-constant value of the turbulent time-scale ratio

$$R=0.5*(\overline{T^2}/\varepsilon_T)/(k/\varepsilon) \qquad (11)$$

can be calculated which is otherwise needed to model the sink term in the $\overline{T^2}$ equation. For more details see Carteciano and Grötzbach (2001).

Conclusions:

The recalculations of the TEFLU experiments show the limits of the applicability of an eddy diffusivity approach used by the widely used k-ε-σ_t model to buoyant liquid metal flows. The TMBF which is a compromise between the classical k-ε-σ_t model and the Reynolds stress model is clearly an improvement of the k-ε-σ_t model for turbulent flows where the turbulent transport of heat is complex and the Reynolds analogy is not valid, such as in buoyant liquid metal flows. A further development of the TMBF model should still be carried out as the radial profiles of $\overline{T^2}$ in the plume regime are overestimated. In fact, a new modeling depending on the Peclet number should be developed for the transport equation of ε_T (Wörner and Grötzbach (1996) and Wörner et al. (1999)). Further validation of the TMBF model for heavy liquid metals has to be carried out for flow regimes in which the velocity field is considerably influenced by the turbulent heat transport, this means for buoyant flows.

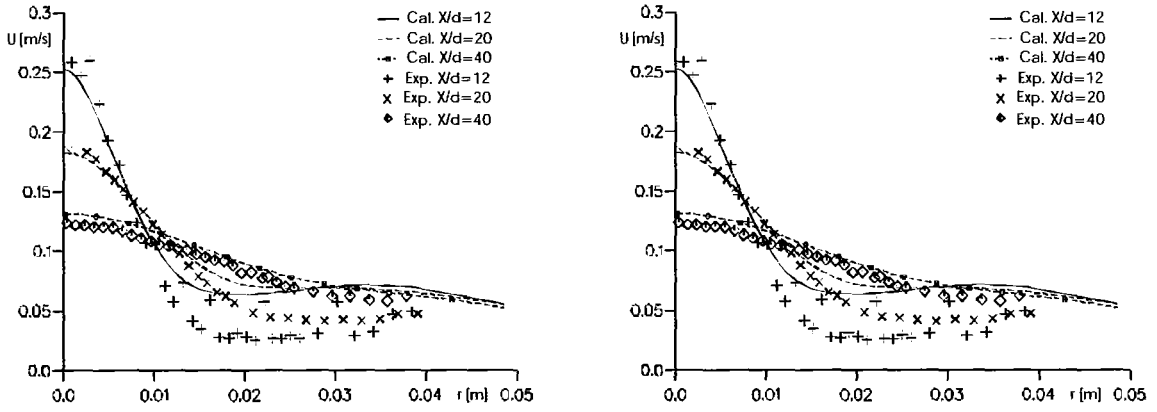

Figure 41: Radial velocity profiles. Forced Jet. Calculation with the k-ε-σ_t model (left) and the TMBF model (right).

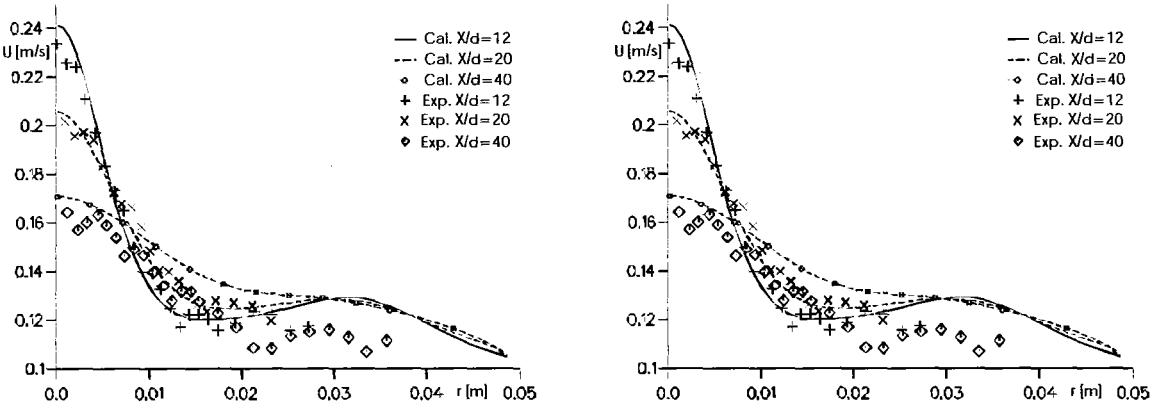

Figure 42: Radial velocity profiles. Buoyant Jet. Calculation with the k-ε-σ_t model (left) and with the TMBF model (right).

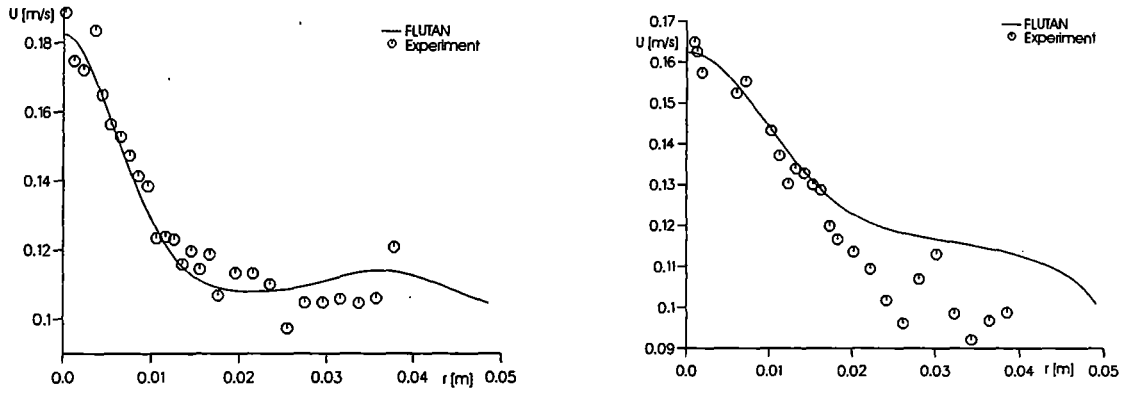

Figure 43: Radial velocity profiles at x/d=12 (left) and x/d=40 (right). Plume. Calculation with the k-ε-σ_t model.

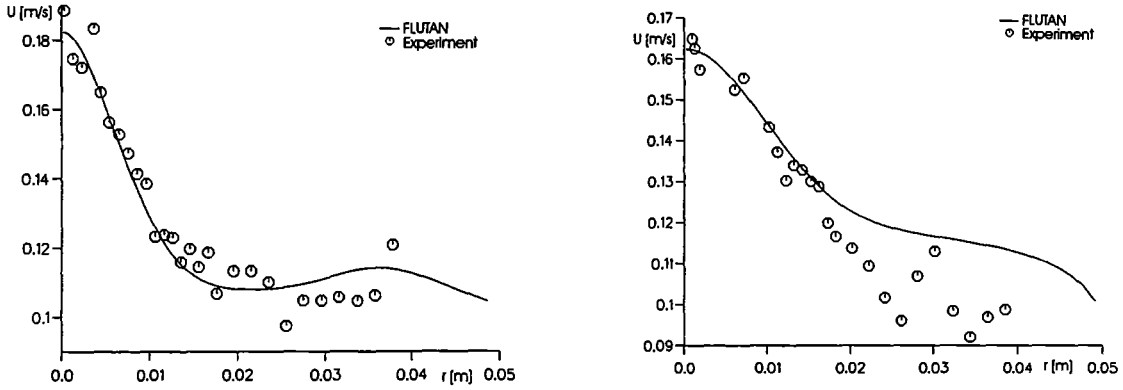

Figure 44: Radial velocity profiles at x/d=12 (left) and x/d=40 (right). Plume. Calculation with the TMBF model.

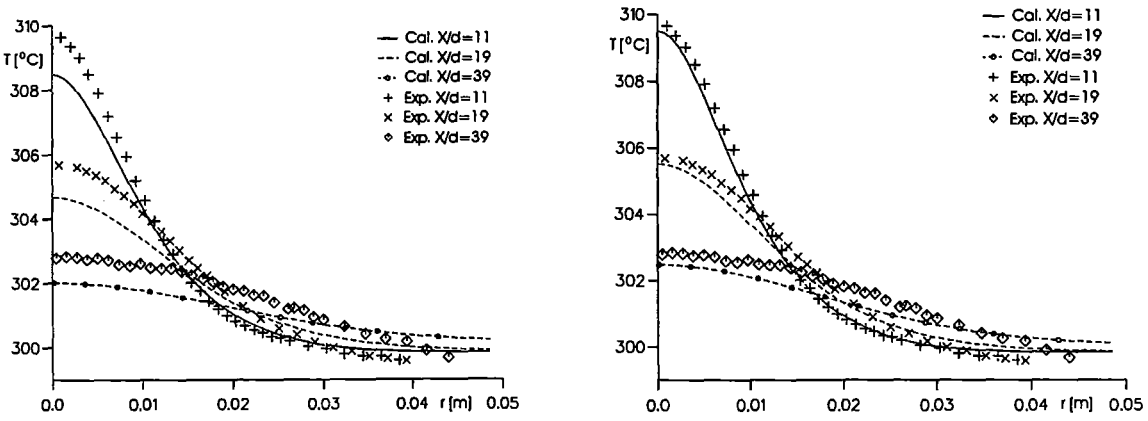

Figure 45: Radial temperature profiles. Forced Jet. Calculation with the k-ε-σ_t model (left) and with the TMBF model (right).

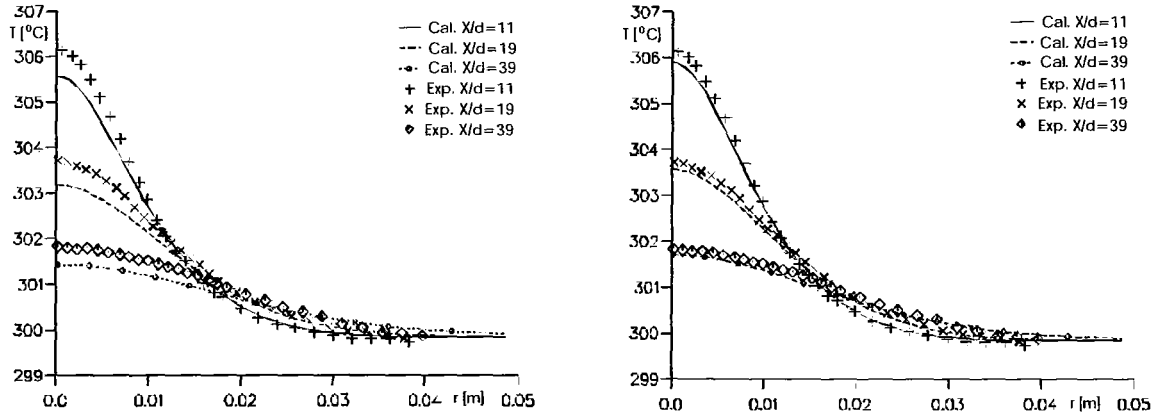

Figure 46: Radial temperature profiles. Buoyant Jet. Calculation with the k-ε-σ_t model (left) and with the TMBF model (right).

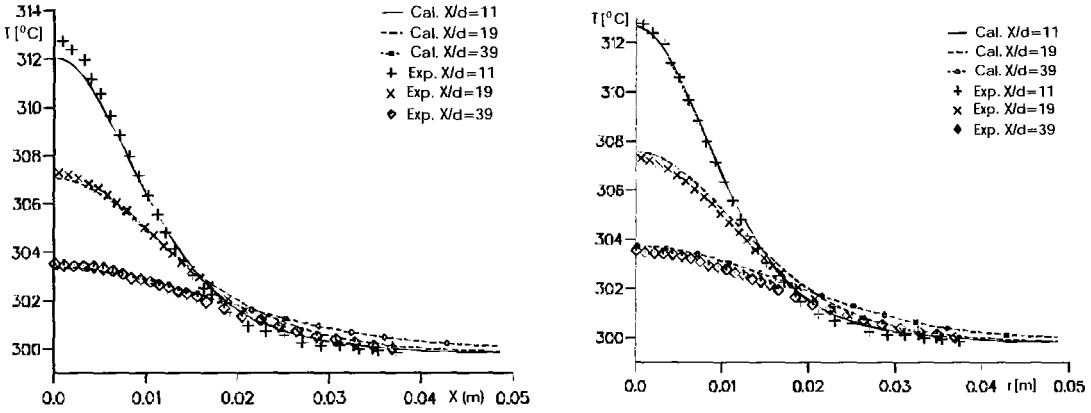

Figure 47: Radial temperature profiles. Plume. Calculation with the k-ε-σ_t model (left) and with the TMBF model (right).

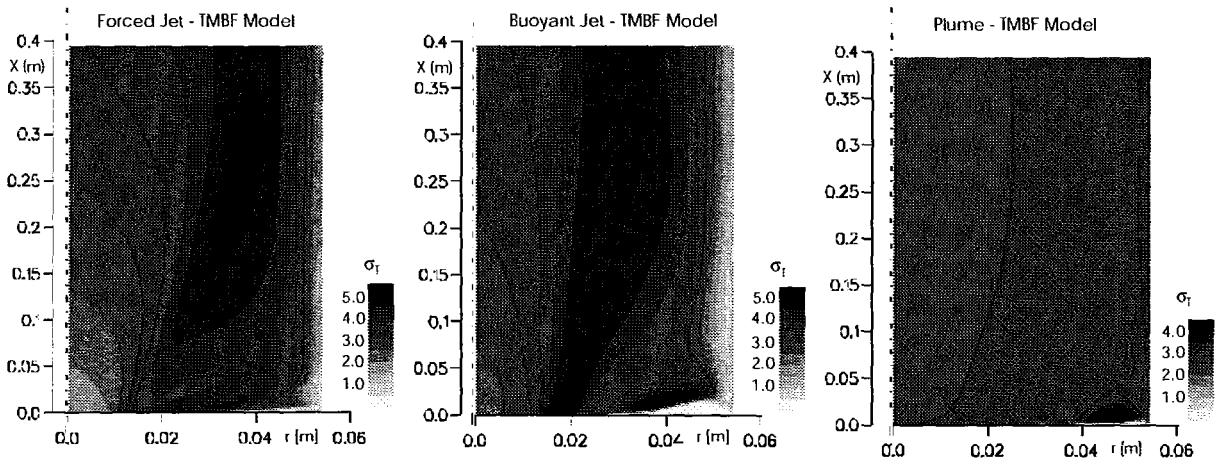

Figure 48: Field of the turbulent Prandtl number calculated with the TMBF model.

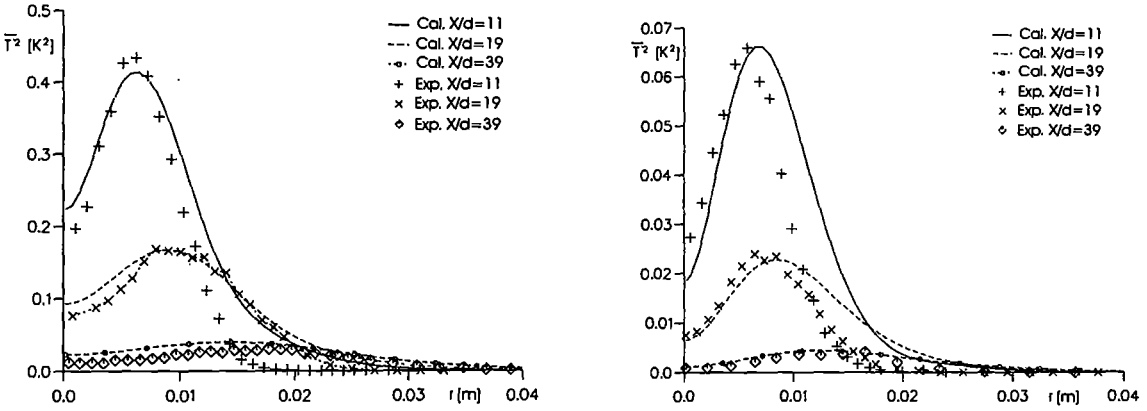

Figure 49: Radial profiles of the temperature variance. Forced Jet (left) and Buoyant Jet (right). Calculation with the TMBF model.

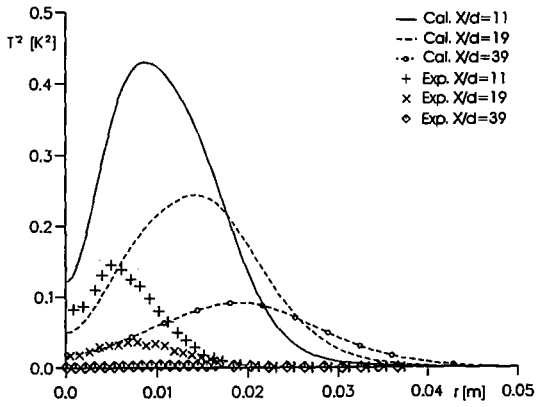

Figure 50: Radial profiles of the temperature variance. Plume. Calculation with the TMBF model.

2.2.3 Work Package WP3: Simulation Experiments for the Optimized Beam Window in Lead-Bismuth and Numerical Simulation of Beam Window and Spallation Target

2.2.3.1 Numerical Simulations for the modified COULI Benchmark

Investigated Target Geometry:

The numerical analysis of the cooling conditions and the temperature field in the target need accurate and reliable turbulence models in the used Computational Fluid Dynamics (CFD) codes. In order to analyze the quality of the numerical models, a reference geometry was specified for a first benchmark investigation (Bellucci et al. (1999)) in advance of experiments in the COULI water loop at CEA Grenoble. Calculations were performed by the participants using different codes; Forschungszentrum Karlsruhe participated with the FLUTAN code (Willerding and Baumann (1996)) in order to, first, further verify the turbulence models used (Baumann et al. (1999)) and, second, investigate in more detail the flow in the COULI geometry. This benchmark models an isothermal flow in an ADS target geometry which will be experimentally investigated in KALLA at a later stage.

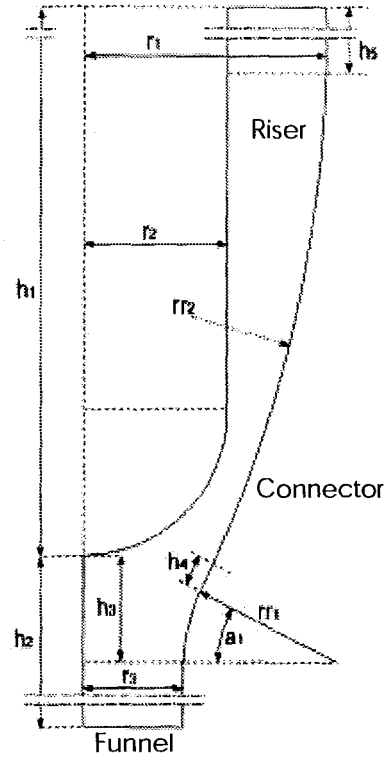

Parameter	Full scale value	COULI (1/1.4)
h_1 (mm)	1000	714.29
h_2 (mm)	1000	714.29
h_3 (mm)	80	57.14
h_4 (mm)	10	7.14
h_5 (mm)	(638.93)	(456.38)
r_1 (mm)	170	121.43
r_2 (mm)	100	71.43
r_3 (mm)	70	50
rr_1 (mm)	134	95.71
a_1 (deg)	25	25
rr_2 (mm)	(888.22)	(634.4)

Figure 51: Target geometry for the COULI benchmark (the numbers in brackets can be deduced from the other dimensions).

Two cases for the benchmark geometry (Figure 51) of the COULI experiment, one for a low Reynolds number Re = 2×10^4, and one for a realistically high Reynolds number Re = 9×10^5 were defined. The water temperature is 60°C. FLUTAN calculations, which were performed using the standard k-ε model, simulate a flow detachment at the inner wall downstream of the beam window (Figure 52). The flow detachment is indicated by the local inversion of the velocity gradient near the wall, i.e. by an increase of the modulus of the velocity in approaching the wall (fluid of higher velocity is encapsulated by fluid of lower velocity). The detailed results of the FLUTAN calculations are documented in Knebel et al. (2000). All codes participating in the

benchmark found some flow detachment downstream of the beam window, but at different locations, on the inner/outer wall, and at different Reynolds numbers. At present, none of the applied computer codes can reliably predict the location and extension of the flow detachment with the models used. Therefore, even without heat transport a complex interaction is observed between physical models and numerics in the simulation of flows, which are typical for an ADS spallation target and corresponding experiments in KALLA. As a consequence, an extremely careful physical modeling is needed.

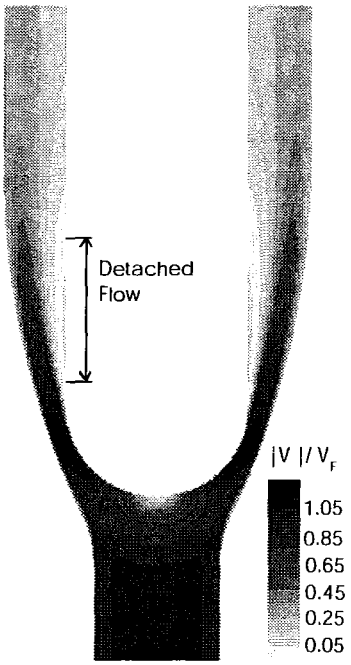

Figure 52: FLUTAN results for the COULI benchmark geometry. Field of the modulus of velocity for Re = $9x10^5$.

The objective of the work performed during the reporting period is to modify the geometry in such a way that the risk for the occurrence of flow separation is minimized. The modified geometry is deduced by means of numerical investigations in combination with the knowledge on criteria for separation-free diffusers.

Geometry Optimization and Numerical Results:

The calculated flow detachment in the original COULI geometry is caused by the strong non-linear widening of the cross section together with an insufficient momentum transport by turbulence away from the stagnation point. The opening angle of the outer tube in the benchmark geometry reaches a value of $\varphi = 17°$, which causes flow detachment in case of a fully developed turbulent flow in an annular diffuser. Therefore, geometry modifications are numerically investigated.
The COULI geometry is no standard geometry for which one can find recommendations for opening angles in text books to achieve a separation-free flow. Here the numerical investigations are done, first, for the two standard cases of a plane and an annular diffuser in order to reproduce these cases with the code. Second, a modified geometry for COULI, which is free of separation, is developed with the help of the FLUTAN code. The code version which is used throughout this investigation is the Cartesian version of FLUTAN, because the newly developed version using body-fitted non-orthogonal grids (Jin (2001)) is not fully implemented and tested whenperforming this study.

Plane and annular diffuser:
In case of a plane diffuser with a linear widening of the cross section, the critical opening angle φ_0 in which first detachments of the flow appear, depends on the Reynolds number: for example $\varphi_0 = 10°$ with $Re = 5x10^4$ (VDI-Wärmeatlas (1974)). This value is valid for cross section ratios $A < 0.5$. In the case of an annular diffuser with linear widening of the cross section, φ also depends on the radius. The critical angle decreases from $\varphi_0 = 10°$ to 7.2° in case of an annulus with a geometry similar to COULI.
Some numerical studies on the influence of the opening angles of the outer tube on the flow separation were performed with FLUTAN. A fully developed turbulent annular diffuser flow similar to the COULI-geometry with $A = 0.26$ and $Re = 9x10^5$ was investigated. The same total length of the COULI-geometry (h_1+h_2) was considered; the outer diameter of the annular diffuser varied from 87.1 mm to 121.4 mm (like r_1 of the COULI-geometry, see Figure 51); the inner diameter was 71.4 mm like r_2 of the COULI-geometry. The linear widening of the cross section was modeled with two different opening angles: $\varphi = 7.1°$ and 9.5°. A 2-D numerical grid was used with about 42,000 cells in cylindrical coordinates. The mesh size was uniform in the x direction $\Delta x = 0.71$ mm. A coarser grid was used in the vertical direction with Δz varying from 0.71 mm to 7.1 mm. The numerical results show that detached flow occurs only in the calculation for the higher opening angle, whereas FLUTAN shows non-detached flow for the smaller opening angle as well (Figures 53 and 54).

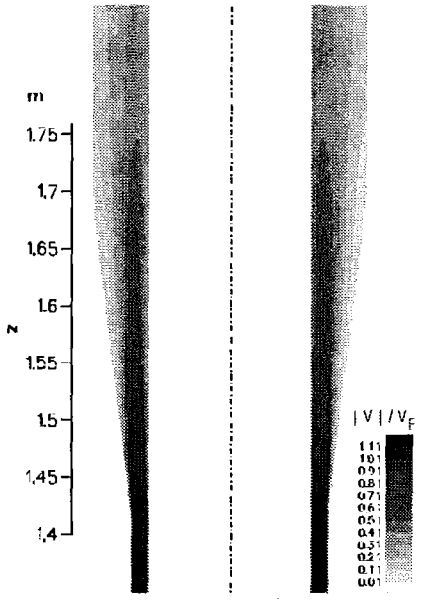

Figure 53: FLUTAN results for an annular diffuser flow with an outer tube opening angle of 7.1°. Field of the modulus of velocity for $Re = 9x10^5$.

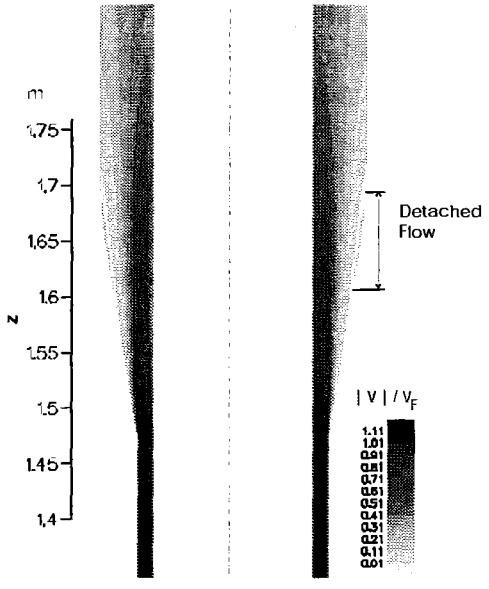

Figure 54: FLUTAN results for an annular diffuser flow with an outer tube opening angle of 9.5°. Field of the modulus of velocity for $Re = 9x10^5$.

Modified geometry:
In the benchmark geometry for COULI, the opening angle of the outer tube at the smallest cross section is $\varphi = 17°$. Thus, it is clearly higher than the critical angle for a fully developed turbulent annular diffuser flow. In order to obtain a geometry free of flow detachments, the benchmark geometry was modified by reducing the widening

of the cross section of the connector. In the modified geometry the opening angle of the outer tube was decreased to 9.5° with a linear cross section widening. Although separation was simulated for the annular diffuser with 9.5° opening angle, the same angle was chosen, because a higher turbulence production due to the stagnation point is expected in the COULI geometry helping to avoid flow separation.
The calculation was performed for the case with the high Reynolds number $Re = 9x10^5$. The water temperature is 60°C. The funnel length must be set to $h_2 = 14\ D_f = 1.4286$ m (the funnel diameter is $D_f = 0.1$ m) in order to achieve a fully developed flow at the inlet of the connector. A 2-D numerical grid was used. The mesh size was uniform ($\Delta x = \Delta z = 0.71$ mm) in the connector area which is the convergent-divergent duct joining the window region with the riser, see Figure 51. A coarser grid was used in the vertical direction for the funnel ($\Delta z = 7.1$ mm) and for the riser ($\Delta z = 3.6$ mm). The total length of the geometry, which was simulated with 55,929 cells in cylindrical coordinates, was 2.176 m including funnel and riser. The standard k-ε turbulence model was used. The system of the momentum equations and turbulence equations was solved using iterative solvers, respectively the CRESOR (Borgwaldt (1990)) and the SOR method. A very low value for the convergence criterion parameter was chosen: $\varepsilon_3 = 10^{-7}$. The steady state is reached when the change of each velocity component from one time step to the next one divided by the maximum velocity magnitude in the entire field is less than ε_3. The calculations were performed with a first order upwind discretisation method of the convective terms for the momentum and turbulence equations. This is acceptable because of the very fine numerical grid. A first order time discretisation was used with a time step width of $\Delta t = 0.1$ s.
The FLUTAN calculation with the modified geometry shows no separation of the flow along the inner tube (Figure 55) due to the reduction of the widening of the cross section of the connector. In contrast to the numerical study for the annular diffuser with the same opening angle of the outer tube (9.5°), the separation disappears now. The reason can be found in the higher production of turbulence at the stagnation point leading to larger turbulent viscosities along the beam window and in the potential separation area, see Figures 56 and 57.

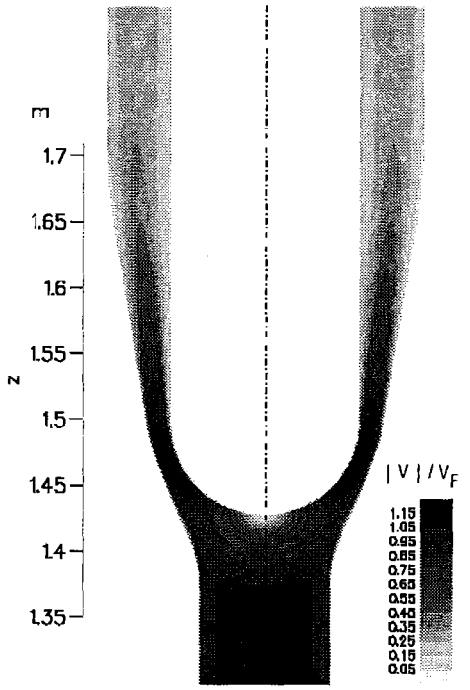

Figure 55: FLUTAN results for a modified geometry of COULI with an outer tube opening angle of 9.5^0. Field of the modulus of velocity for $Re = 9x10^5$.

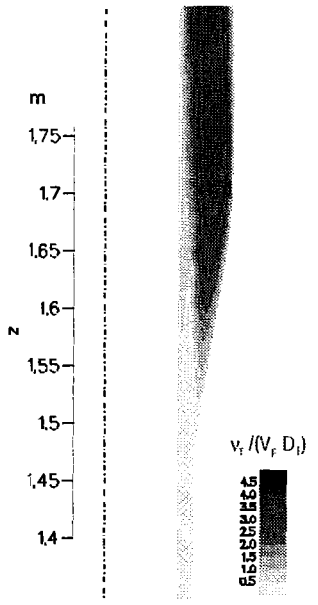

Figure 56: FLUTAN results for an annular diffuser flow with an outer tube opening angle of 9.5°. Field of turbulence viscosity for Re = $9x10^5$.

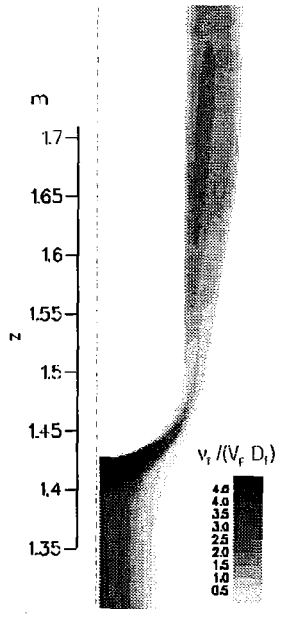

Figure 57: FLUTAN results for a modified geometry of COULI with an outer tube opening angle of 9.5°. Field of the turbulence viscosity for Re = $9x10^5$.

Conclusions:

A benchmark target geometry for the COULI experiment was proposed in order to test the turbulence models of different CFD codes and to clarify whether the COULI target geometry is free of boundary layer separation. FLUTAN calculations of the benchmark target geometry simulated a flow detachment at the inner wall downstream of the beam window. This is for an opening angle of the outer tube of 17°. A similar flow detachment is observed for the case of a fully developed turbulent flow in an annular diffuser of 17°.

The critical angle for the occurrence of flow separation in an annular diffuser was reproduced by FLUTAN. Therefore, a modified COULI geometry can be numerically investigated with the FLUTAN code. In the modified geometry, the connector has a smaller linear widening of the cross section, the opening angle of the outer tube being 9.5°. For this case no flow detachment is calculated by FLUTAN.

Nevertheless, an appropriate modeling of the turbulence transport in the connector is decisive in order to predict the existence or non-existence of a flow detachment. It has to be kept in mind that reliable predictions are not possible because the applied standard k-ε-σ_t model uses universal wall functions which are not valid in the surrounding of the stagnation point and in the separation area. A final conclusion on the quality of these results has to be backed up by lead-bismuth experiments in KALLA.

In addition, the consequences of the modified geometry on the cooling conditions for the beam window have to be considered. FLUTAN would be an adequate tool for such investigations because it uses the Turbulence Model for Buoyant Flows, TMBF (Carteciano et al. (1997)), which turned out to achieve good accuracy in another benchmark on liquid metal flows with heat transfer (Baumann et al. (1997)).

2.2.3.2 One-dimensional analysis of the flow behaviour within a 4 MW spallation target

Introduction:

The overall objective of sub-project 3 is to design a large-scale spallation target which can be implemented in an ADS demonstrator. Before starting to design a test rig for such a large-scale spallation target, simple one-dimensional calculations have to be performed, in order to clarify the general layout and geometry of the major components of such a spallation target (cf. figure 58) and its heat removal chain (cf. figure 59), together with the dimensions and the total driving heights needed. The heat removal considered here is by natural circulation only. These data are important as they have to be technically feasible and to match with the dimensions defined within the design of the ADS demonstrator.
The major objectives of the integral experiment on a large-scale spallation target are:

- Demonstration of the beam window coolability,
- Demonstration of the heat removal from the spallation area and the beam window by natural circulation,
- Steady-state and transient characteristics of heat transport in a coupled loop system under natural circulation,
- Demonstration of oxygen control system,
- Corrosion behaviour of structural and window materials,
- Set-up of a data base for physical model and code validation,
- Simulation of fluid flow phenomena using CFD codes.

Investigated Geometry:

The considered heat removal system consists of three coupled loops, see figure 59. The heat transport between spallation area and environment is done by natural circulation only.

- Primary loop or spallation target itself (fluid: Pb-Bi),
- Secondary loop (fluid: Pb-Bi),
- Tertiary loop (fluid: air).

The main components of the heat removal system are the following:

- Spallation area and beam window,
- Primary-secondary heat exchanger (see figure 60),
- Secondary-tertiary heat exchanger, see figure 61),
- Stack (see figure 59).

A detailed geometrical description of the components is given in Neitzel and Knebel (2000).
A modification to this design could be a forced convection heat removal system utilizing pumps in the primary and secondary loop, and an air blower in the tertiary loop. In this case, the fluid of the secondary loop could be an organic fluid, as proposed for the EA Demonstrator by Ansaldo Nucleare (1999). These modifications are not considered here.

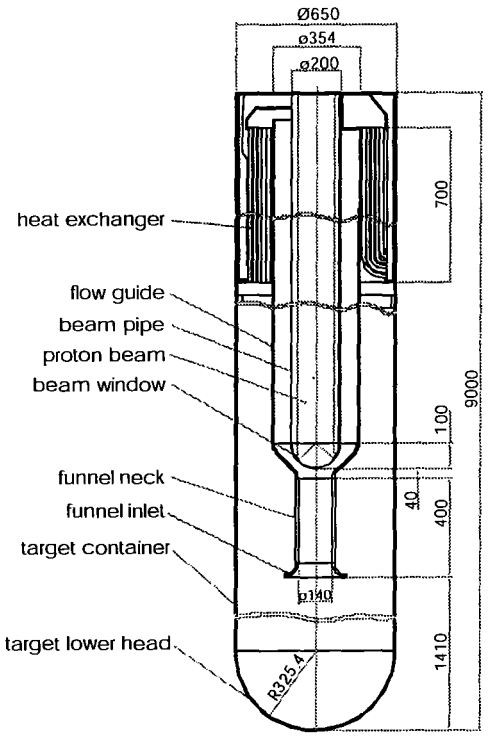

Figure 58: Sketch of a spallation target module of 4 MW beam power.

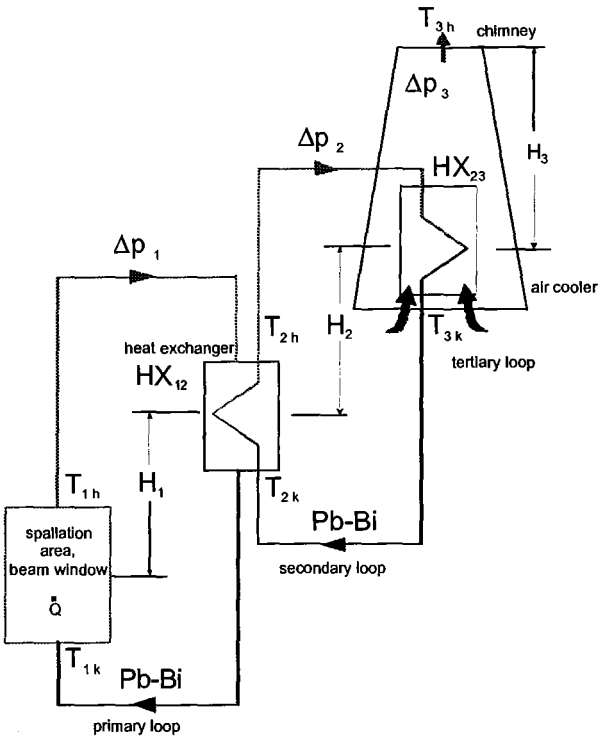

Figure 59: Natural circulation heat removal chain for the integral experiment K4T: primary Pb-Bi loop, secondary Pb-Bi loop, tertiary air loop.

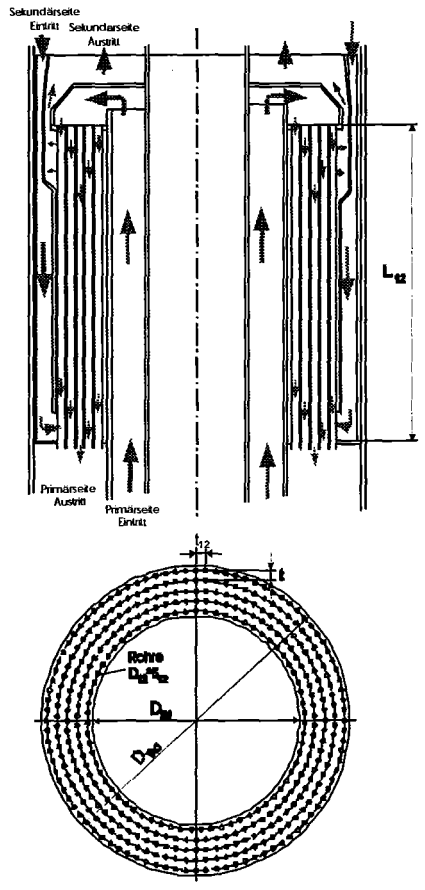

Figure 60: Sketch of primary-secondary heat exchanger.

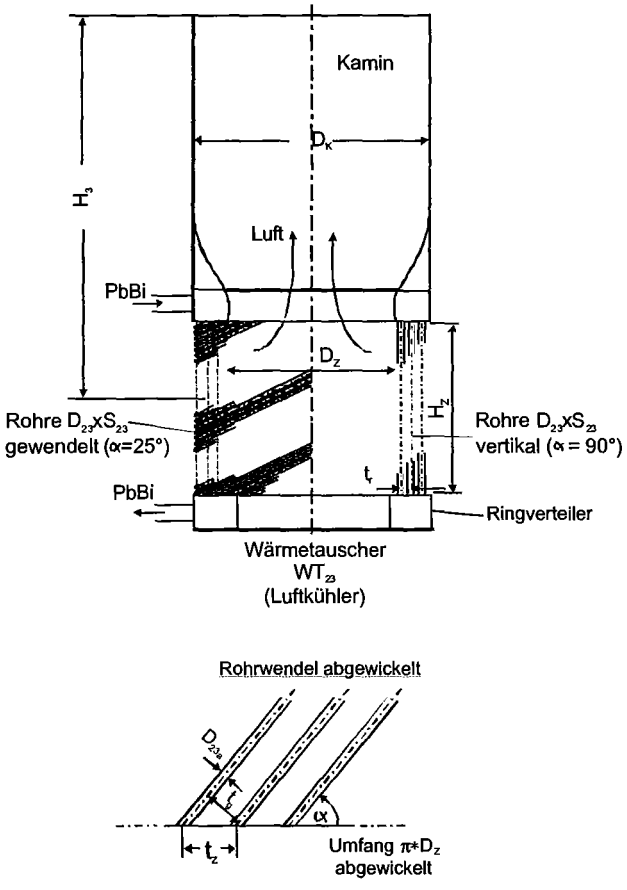

Figure 61: Sketch of secondary-tertiary heat exchanger.

Results:

According to the one-dimensional calculations in Neitzel and Knebel (2000) the main results for a spallation heat of 4 MW are summarized in table 4.

Table 4: Main results for the design of a 4 MW spallation target.

	Primary loop	Secondary loop	Tertiary loop
Power	$\dot{Q} = 4\ MW$		
Fluid	Pb-Bi	Pb-Bi	Air
Temperature hot leg / cold leg	$T_{1h} = 500°C$ $T_{1k} = 350°C$	$T_{2k} = 200°C$ $T_{2h} = 350°C$	$T_{3h} = 150°C$ $T_{3k} = 30°C$
Mass flux	$\dot{m}_1 = 181\ kg/s$	$\dot{m}_2 = 181\ kg/s$	$\dot{m}_3 = 33\ kg/s$
Pressure drop	$\Delta p_1 = 9130\ Pa$	$\Delta p_2 = 19300\ Pa$	$\Delta p_3 = 13\ Pa$
Driving height	$H_1 = 5.17\ m$	$H_2 = 10.36\ m$	$H_3 = 4.05\ m$

As shown in table 4 the overall dimensions such as temperature levels, mass fluxes, pressure drops and, above all, geodetic driving heights for the natural circulation heat removal can be realized with technically reasonable efforts in an ADS demonstrator. Thus, a spallation target with 4 MW of spallation power is a technically feasible design for normal, steady-state operation conditions.

Conclusions:

From the calculated pressure drops and required driving natural circulation heights it can be concluded that a natural circulation heat removal from a closed spallation module of 4 MW beam power is feasible. This holds for steady-state conditions.
Future emphasis will be on the transient characteristics of the complete heat removal chain from the spallation area to the environment under normal operation and decay heat removal conditions. Limitations of such a heat removal system, which is entirely relying on natural circulation forces, have to be specified.

2.2.3.3 Numerical two and three-dimensional analysis of the complete MEGAPIE spallation target with the computer code FLUTAN

Introduction:

The results of the experimental and numerical investigations on the cooling of thin-walled thermally highly-loaded surfaces shall finally be applied to the development of a complete spallation target module. In parallel to this HGF Project, the MEGAPIE spallation target is developed at PSI (Bauer et al. (1999)). The combination of the results of both projects will provide a valuable know-how and experience in order to develop a spallation target for an ADS demonstrator.
The detailed numerical analyses of the beam window area of the MEGAPIE spallation target needs a sufficiently fine grid. With the current computers and commercially available CFD codes such detailed numerical analyses can only be performed for a relatively limited area around the beam window. Thus, accurate boundary conditions are required for the inlet and outlet of this limited computational domain. Such boundary conditions can be provided by approximate 2-D and 3-D simulations of the complete MEGAPIE module using the FLUTAN code (Willerding and Baumann (1996)). FLUTAN is a transient 3-D thermal and fluid-dynamical code with a number of physical models like several turbulence models, heat exchanger and thermal structure models (Grötzbach et al. (2000)). Another task is the numerical investigation of the principal features of the complete target module in case of transients caused by proton beam or cooling loop trips.
The objective of this first numerical simulation for a complete target module is to investigate the feasibility of using FLUTAN for such calculations and to gain a first insight in the flow and cooling behavior of a target module.
Here, first, 2-D and 3-D calculations for a simplified so-called original geometry are performed, and, second, 3-D calculations for a simplified so-called new geometry by Sigg (2001) are discussed.

Investigated Geometries and Numerical Results:

Original geometry, 2-D natural and forced convection, without bypass:
In a first step, 2-D FLUTAN calculations with a simplified modeling of the complete MEGAPIE target module following the construction drawings of February 2000 were performed for natural convection without a bypass jet flow across the window. The spatial distribution of the power deposition by the proton beam of 541 kW in the liquid lead bismuth and in the structures is prescribed using an equation provided by Smith (2000). The window is cooled by liquid lead-bismuth flowing downwards in the annular space and upwards inside the inner pipe (Figure 62). Both channels are separated by the guide tube. The 2-D thermal conduction in the guide tube was calculated for several materials with thermal conductivities ranging from 1 to 16 W/(m K). The annular heat exchanger at the upper end of the target module is modeled by a heat sink distributed uniformly over the heat exchanger cross section, by the correct flow area, and by the two grid plates carrying the (not recorded) heat exchanger pipes. The fluid temperature at the heat exchanger exit is prescribed to be 223°C. The standard k-ε model is used.
When the guide tube is modeled as a thermal structure made of 316L steel with a given heat conductivity of 16 W/(m K), the FLUTAN calculation shows that a thermal power of 513 kW is conducted through the guide tube from the hot flow inside the guide tube to the cold downcomer flow. This heat input increases the fluid

temperature near the window drastically (Figure 62). The maximum temperature in the fluid reaches 2100°C at the stagnation point at the window center. This is above the boiling temperature, but we assumed single phase conditions and extrapolated the material property data linearly. On the other hand, the temperature difference between the fluid temperature in the window region and at the heat exchanger inlet is reduced correspondingly. Due to the large radial heat flux, large radial temperature differences occur mainly inside the guide tube and also inside the cold down comer. A mass flow rate of only 13.3 kg/s is achieved; correspondingly, the temperature difference between inlet and outlet of the heat exchanger results in 256 K. So, the large radial heat flux through the guide tube is a consequence of the small mass flow rate and the following high temperature differences inside the module. Such a concept, even if it would be used as a safety backup measure, is absolutely not acceptable.

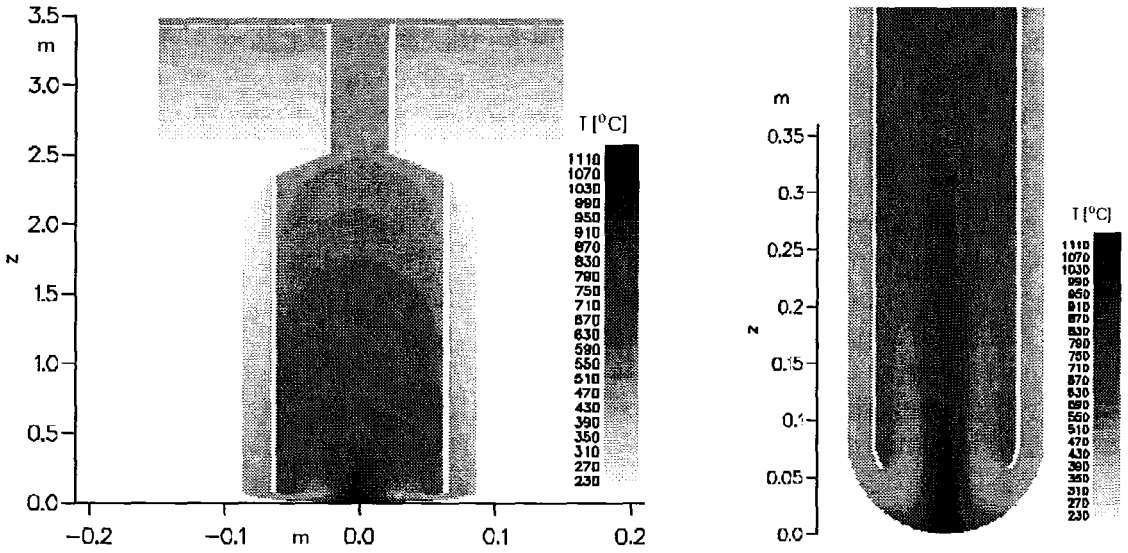

Figure 62: Calculated field of temperature. 2-D calculation, old geometry, natural convection, thermal conductivity of 16 W/(m K) inside the guide tube.

When a guide tube with a small thermal conductivity is used, e.g. with a heat conductivity of 1 W/(m K), the heat conducted through the guide tube decreases to only 70 kW. Therefore, the mean fluid temperature in the window region is clearly reduced in this case to 1888°C at the window center, in comparison to the previous case (Figure 63). On the other hand, the fluid temperature at the heat exchanger inlet is increased when the guide tube is almost thermally insulated. This results from the reduced heat conduction from inside the guide tube radially outwards into the heat exchanger. The influence of the thermal conductivity of the guide tube on the mass flow rate is almost negligible.

2-D calculations were also performed with FLUTAN for forced convection without a bypass, using a thermal conductivity of 16 W/(m K) inside the guide tube. The pump was specified to achieve a mass flow rate of 35 kg/s. The temperature difference across the heat exchanger is now reduced to 105 K (Figure 64). With the reduced temperature level inside the module the total radial heat flux through the guide tube is reduced to 165 kW; from this, 135 kW occur in the area below the cooler, and 30 kW radially into the cooler. The downcoming fluid arriving at the gap near the window is increased correspondingly by 29 K against the heat exchanger outlet temperature. The maximum fluid temperature near the window center remained with 1930°C above the boiling value. Thus, also these 2-D simulations with forced convection

show that a bypass jet flow across the beam window is absolutely necessary to remove the consequences of the insufficient heat transfer from the stagnation point at the beam window center.

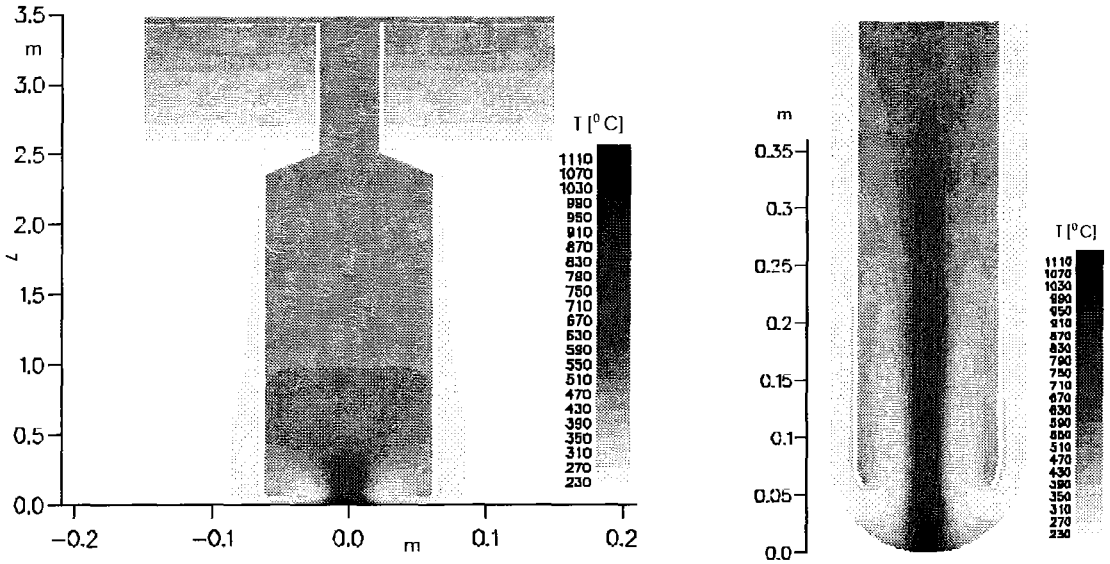

Figure 63: Calculated field of temperature. 2-D calculation, old geometry, natural convection, thermal conductivity of 1 W/(m K) inside the guide tube.

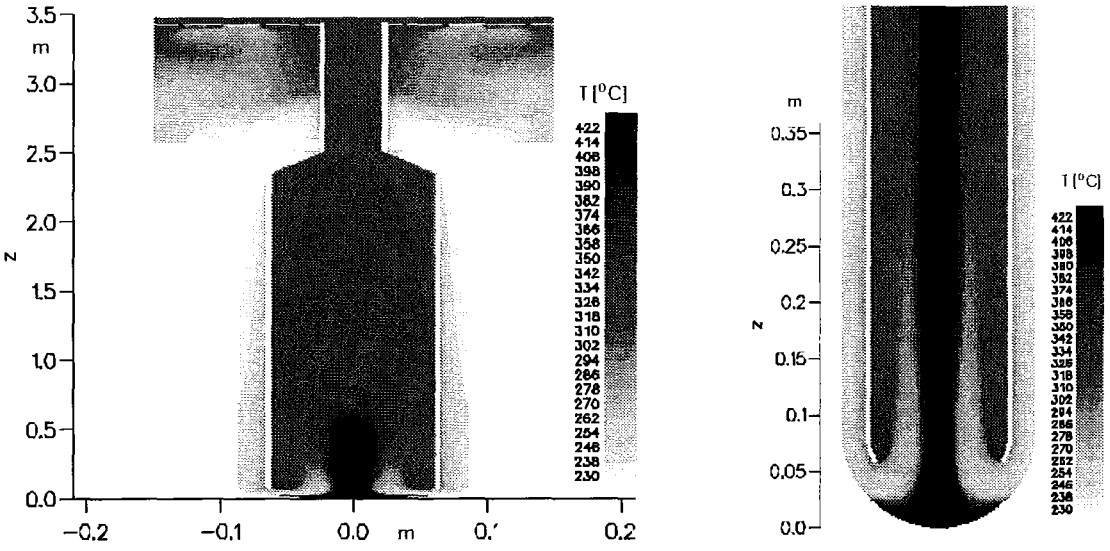

Figure 64: Calculated field of temperature. 2-D calculation, old geometry, forced convection, thermal conductivity of 16 W/(m K) inside the guide tube.

Original geometry, 3-D forced convection, with bypass:
Simulations for a concept with bypass require 3-D representations. We consider a forced convection case with thermal conduction in the guide tube in the old geometry, and natural convection cases for a rough approximation of the new reference geometry with and without thermal conduction in the guide tube.
First 3-D calculations were performed following the construction drawings of February 2000 for the MEGAPIE design. The bypass in form of a jet flow across the window surface is modeled numerically by adding a source term at the position of the outlet nozzle specifying a certain mass flow rate (see the position of the velocity maximum

near the center of the window). The piping system feeding that nozzle is not recorded in the simulation. The spatial distribution of the power deposition of 541 kW in the liquid lead bismuth and in the structures is the same as it is used in the 2-D calculations. The 3-D thermal conduction in the guide tube was calculated with two different thermal conductivities of 1 and 16 W/(m K). The heat exchanger is modeled by a heat sink distributed uniformly over the heat exchanger cross section, by the correct flow area, and by the grid plates carrying the heat exchanger pipes. The fluid temperature at the heat exchanger exit is prescribed to be 223°C. The standard k-ε model is used again with a constant turbulent Prandtl number of $\sigma_t = 0.9$ to calculate the heat transfer.

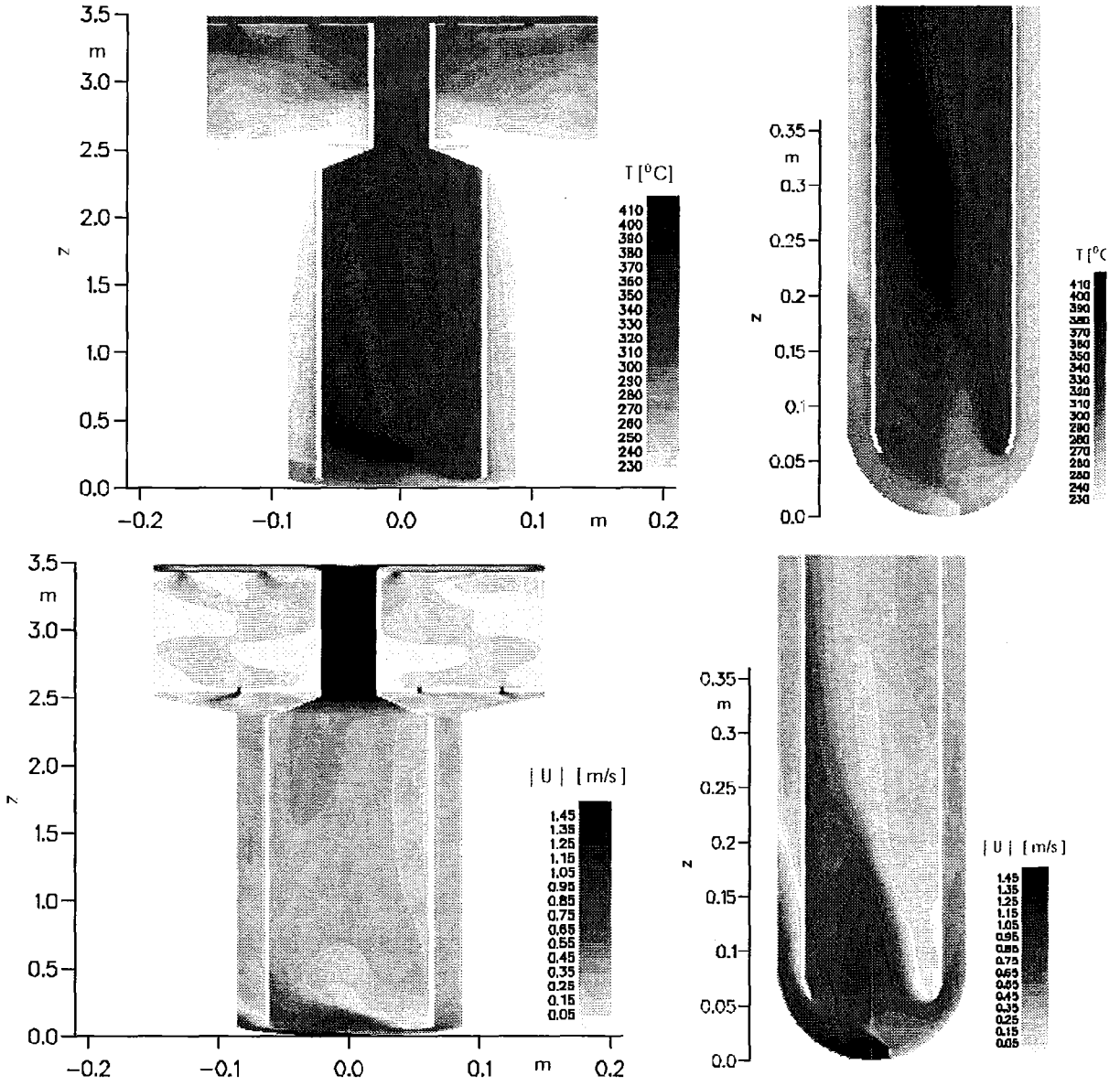

Figure 65: Calculated field of temperature and modulus of velocity for the whole module and for the bottom part. 3-D calculation, old geometry, forced convection, mass flow rate of the bypass 3.5 kg/s, thermal conductivity of 16 W/(m*K) inside the guide tube.

The 3-D forced convection results from FLUTAN with a bypass of 3.5 kg/s, using a thermal conductivity of 16 W/(m K) inside the guide tube, are shown in Figure 65. The pump was specified to achieve a mass flow rate of 35 kg/s. Due to the bypass flow, the maximum value of the temperature of 483°C is far below the boiling temperature.
The FLUTAN calculation shows that a thermal power of 152 kW (29% of the power deposition) is conducted through the guide tube from the hot flow inside the guide tube to the cold downcomer flow. The calculated velocity field shows an asymmetry between the flow field on the left bottom part of the downcomer and the one at the right side. This asymmetry is due to the fact that part of the bypass flow directly injects fluid through the gap between window and guide tube on the left. Some of the injected fluid is rising through the downcomer against the downwards coming cold fluid and forms a vortex flow in the lower part of the annular downcomer. The zero-line in the velocity field in the left part of the annulus separates upwards and downwards coming fluid. Thus, the fluid has to redistribute azimuthally in the annular downcomer and consequently forms there a complex 3-D vortex. This lower vortex induces also a vortex with opposite rotation direction in the annulus above, which is the reason for asymmetries in the u and T-field in the downcomer up to the heat exchanger outlet. The vortex may be even stronger in reality because the additional friction forces due to the bypass piping system coming down on the right hand side of the downcomer was not recorded in the calculation. The entity of this secondary flow will depend on the flow rate of the bypass and on the widths of the gap between guide tube and window. This asymmetry in the downcomer makes any separate local calculation for the window area problematic.

New geometry, 3-D natural convection, with forced bypass flow:
New construction sketches for the new MEGAPIE target module concept were provided by Sigg (2001). The concept for the upper part of the target with the heat exchanger and the disposition of the pumps was modified in order to reduce the irreversible pressure losses due to the geometry contour inside the guide tube (see geometry in Figure 1). Meanwhile 3-D calculations were also performed for an approximation of this new geometry. The heat exchanger is again modeled by a heat sink distributed uniformly over the heat exchanger cross section. The outer diameter is adapted to achieve the correct free flow area. The calculations were done for natural convection with a forced bypass flow rate of 1.18 kg/s and with two different thermal conductivities for the guide tube of 16 and 1 W/(m K).
The results show that the influence of the heat transferred through the guide tube on the temperature field is in this concept with 27.6% at λ = 16 W/(m K) versus 4.3% at λ = 1 W/(m K) very small. The temperature level near the window region is for the case of λ = 16 W/(m K) slightly higher in comparison with the other case (Figures 66 and 67). The maximum value of the fluid temperature remains below the boiling temperature in both cases. In fact, a mass flow rate of about 40 kg/s is achieved inside the guide tube. This value is higher than the mass flow rate given in forced convection for the original geometry. This positive result is due to the reduction of the irreversible pressure losses in the new geometry.
An asymmetry in the downcomer exists also in this design, but it is weaker than in the previous case calculated with the old geometry mainly because of a lower value of the bypass flow rate was chosen in this calculation. Nevertheless, the asymmetries reach again far up in the downcomer towards the heat exchanger area. Thus, also in these cases detailed local numerical investigations for the window area will need special assumptions for the inlet and outlet conditions at the boundaries of the computational domain.

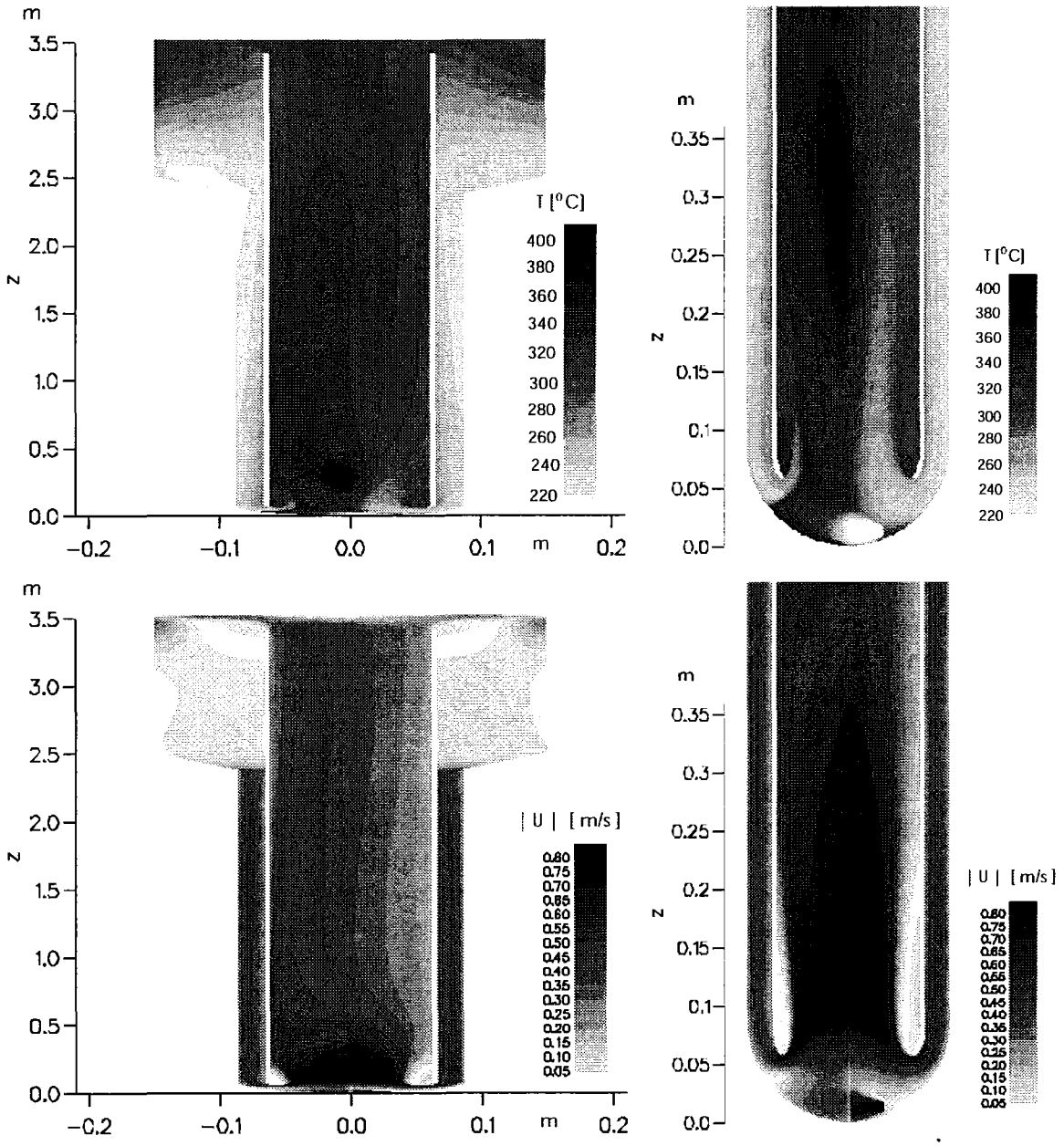

Figure 66: Calculated field of temperature and modulus of velocity for the whole module and for the bottom part. 3-D calculation, new geometry, natural convection, mass flow rate of the bypass 1.18 kg/s, thermal conductivity of 16 W/(m K) inside the guide tube.

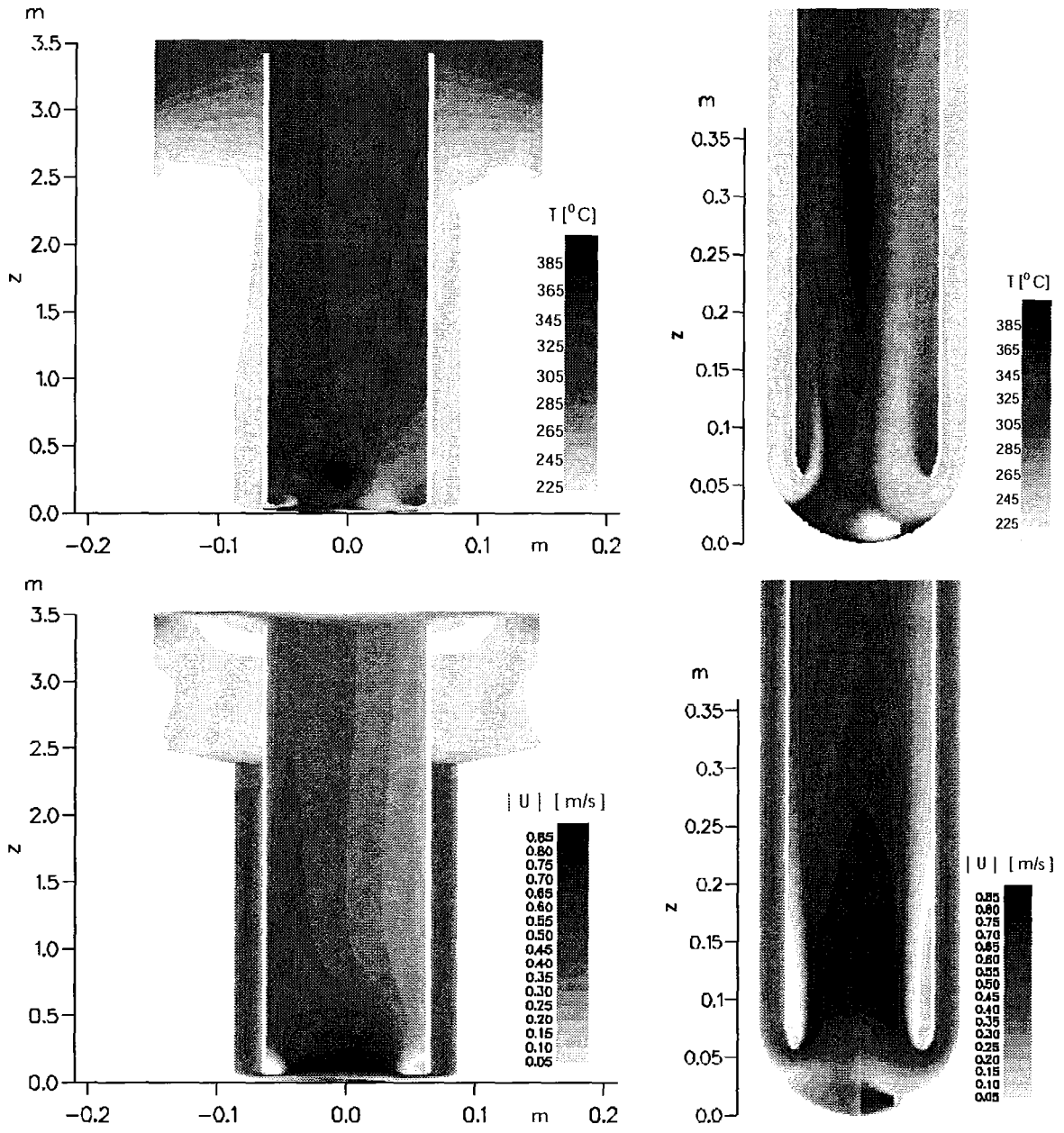

Figure 67: Calculated field of temperature and modulus of velocity for the whole module and for the bottom part. 3-D calculation, new geometry, natural convection, mass flow rate of the bypass 1.18 kg/s, thermal conductivity of 1 W/(m K) inside the guide tube.

Conclusions:

The 2-D and 3-D FLUTAN calculations with a simplified modeling of the complete MEGAPIE target module following the original geometry of February 2000 show that without a bypass jet flow across the window the fluid temperature is above the boiling temperature either in natural convection or in forced convection cases. Here, the thermal conduction inside the guide tube turns out to be a critical feature to determine the coolant temperature at the beam window.

The 3-D investigations with the new geometry and with a bypass jet flow across the beam window show that the influence of the thermal conduction in the guide tube is

small compared to the results for the original geometry, and that it may be possible to neglect it under natural convection conditions. The effects arising from the thermal conduction of the guide tube do not considerably influence the fluid temperature near the beam window. It can be concluded that this target can be effectively cooled even by means of a natural convection regime in combination with a forced bypass flow. This is achieved by the reduction of the irreversible pressure losses.
The 3-D results show that the bypass flow induces vortices in the guide tube which cause asymmetries in the downcomer up to the heat exchanger area. As this asymmetry may be increased by including more accurate geometry information, especially of the bypass flow system, it is an iterative procedure between design and more accurate calculations in order to provide the information which is necessary to perform local detailed beam window cooling calculations.
The next steps should be, first, to analyze the influence of using improved turbulence modeling of heat transfer, especially of using the extended Turbulence Model for Buoyant Flows TMBF (Carteciano et al. (1999)), and, second, to analyze the dynamic behavior of the MEGAPIE target by means of 3-D calculations. Such calculations are time consuming and expensive. Thus, only a small number of numerical investigations are possible. These will be performed as soon as the MEGAPIE design is widely settled and as soon as the complete detailed information on the new reference geometry is available.

2.3 Sub-Project SP2: Material Specific Investigations

2.3.1 Work Package WP1: Investigation of the Corrosion and Erosion of Structure and Window Materials in Flowing Lead-Bismuth

This work package WP1 is divided into three steps which systematically describe the mechanisms of corrosion and erosion: first, stagnant experiments without oxygen protection, second, stagnant experiments with oxygen protection, and, third, dynamic experiments in flowing lead are described. The applied techniques and methods for the improvement of corrosion resistivity by surface protection and the surface modification using the pulsed electron beam facility GESA are dealt with in work packages WP2 and WP3, respectively. The applied oxygen control system (OCS) is explained in detail in sub-project SP3, chapter 2.4.

2.3.1.1 Stagnant corrosion experiments without oxidation protection

Introduction:

It is well known from literature that the heavy liquid metal coolants Pb and Bi are much more aggressive corrodents than the alkali metals. For the development of an accelerator driven system (ADS) the corrosion problems of structural materials due to the physical/chemical interaction with the coolant must be solved. Until now there is only little or no experience in the field of corrosion except for military application in the former USSR. Unfortunately these results are unpublished, so that corrosion experiments are strongly required. The tests have to be performed in a corrosion loop in which the liquid metal has a flow velocity in the order of 2 m/s and temperatures of up to 650°C. Such a corrosion loop CORRIDA is part of KALLA. Beforehand, some screening corrosion experiments have been carried out using 8 different ferritic alloys with varying Cr and Al content in static Pb at 600°C up to 10.000 h. First results of specimens exposed for 3.000 h and 5.000 h are already at hand.

Experimental matrix:

Different types of steel have been selected for corrosion testing in Pb: 1.4713, Optifer IVa, Optifer IVc, MANET II, 1.4923, 1.4742, PM 2000 and Ducrolloy. All steels have no or only a small amount of Ni. The Cr content varies between 6 – 8 wt.-% (1.4713) and 50.4 wt.-% (Ducrolloy). The chemical composition of the steels is given in table 5.
The geometry of the steels to be tested was sheet material in different sizes. The samples were polished, degreased in acetone and finally cleaned ultrasonically in ethanol. Afterwards the sheets were inserted into molten lead inside an alumina crucible in a glove box under purified dry Ar atmosphere ($p_{O2} \leq 10^{-6}$ bar, $p_{H2O} \leq 10^{-6}$ bar). The alumina crucibles were put in hermetically closed stainless steel capsules which then were placed in a chamber furnace and kept there at 600°C for 3.000 h, 5.000 h and 10.000 h. After the tests the steel sheets were taken out of the liquid lead in a glove box. There were zones on the surface of the specimens which were covered with Pb. The remaining lead was not washed away in order to make sure that a possibly formed corrosion layer was not removed. All specimens were metallographically examined in order to see how the molten lead has reacted with the different steels. Moreover the lead was analysed to get information about dissolution

of steel elements. Further investigation like EDX and REM still have to be done on the specimens. First metallographical results are already obtained on the 3.000 h and 5.000 h specimens. The 10.000 h hour test is still running.

Table 5: Chemical composition of the investigated steels (wt.-%).

Steel	Fe	Cr	Mn	Others
1.4713	87.98-92.17	6-8	0-1	Al, V, W
Optifer IVa	89.20	8.5	0.57	Ta, V, W
Optifer IVc	89.16	9.05	0.52	Mo, Ta, W, Si
MANET II	86.75	10.37	0.76	Al, Mo, Ni, Si, V
1.4923	83.54-87.25	11-12.5	0.3-0.8	Mo, Ni, Si, V
1.4742	77.21-81.6	17-19	0-1	Al, Si
PM 2000	74.5	19	-	Al, Ti, Y2O3
Ducrolloy	44.14	50.4	-	Al, Ti, Y2O3

Results:

Pb analyses have been made of each crucible in which specimens were exposed for 3.000 h and 5.000 h. The results of the lead analysis after 3.000 h of exposure showed no difference compared to the values obtained for the virgin lead. No increase of any element could be observed. Pb analysis after 5.000 h exposure showed a slightly increase of the iron content. The amount of the other steel elements in lead did not increase in a measurable way.
Metallographical cross sections of Optifer IVc after 3.000 h and 5.000 h in lead are shown in figure 68. It can be exactly seen that the corrosion attack increases with increasing exposure time.

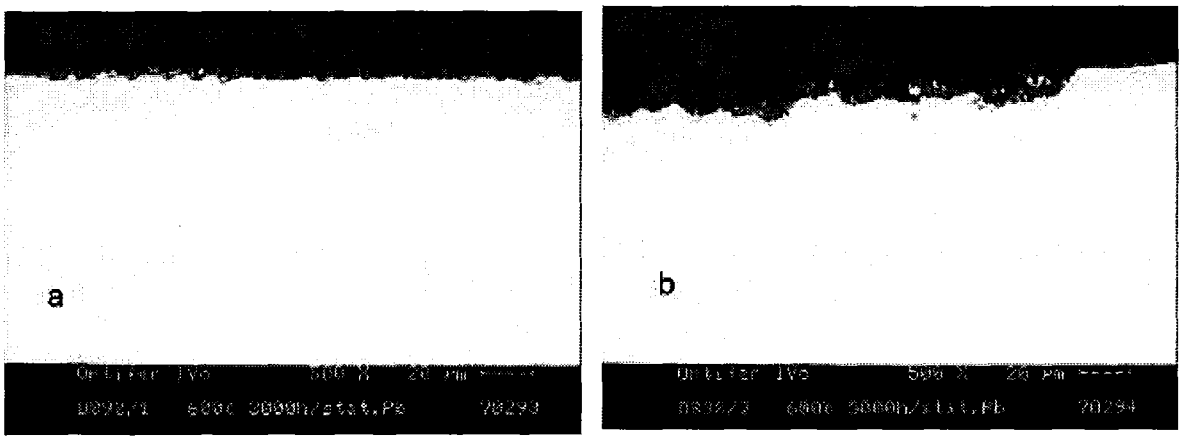

Figure 68: Metallographical cross sections of Optifer IVc after
a) 3.000 h and b) 5.000 h exposure to stagnant lead at 600°C.

Metallographical results obtained on the cross sections of the exposed specimens lead to the following observation: steels with lower chromium content were only little attacked. A more severe corrosion attack could be found in steels with higher chromium content. With longer exposure time the corrosion rate increases as well. Table 6 shows results of corrosion tests in stagnant molten lead. The attack depth was determined on the cross section of each specimen. These values are just a rough estimation for the time and the investigations being, but a tendency can be clearly recognised.

Table 6: Observed maximum corrosive attack depth on specimens exposed to stagnant lead at 600°C.

Steel	3.000 h	5.000 h
1.4713	2 µm	4 µm
Optifer IVa	4 µm	10 µm
Optifer IVc	4 µm	10 µm
MANET II	10 µm	15 µm
1.4923	12 µm	16 µm
1.4742	12 µm	16 µm
PM 2000	15 µm	20 µm
Ducrolloy	20 µm	44 µm

The most severe corrosion attack was found on the alloy Ducrolloy which has a high Cr content (50.4 wt.-%). One of the Ducrolloy specimen exposed to lead for 3.000 h was already investigated with EDX. It could be clearly seen that the Cr content in the near surface region was decreased enormously (down to app. 13 wt.-%) compared to the virgin material because of the high solubility of Cr in lead (Guminski (1990)).

Conclusions:

Corrosion tests in stagnant lead are important as they give general information about the corrosion behaviour of materials. For a further evaluation of the corrosion behaviour of alloys, tests in circulating lead or lead-bismuth are, however, essential due to the phenomena of erosion and mass transport. In addition, an oxygen protection has to be provided.
First results in stagnant lead determined metallographically on cross sections of specimens exposed for 3.000 h and 5.000 h repspectively gave the following observations: First, with increasing Cr content in the alloy the corrosion attack increases, second, with increasing exposure time the corrosion attack increases as well.
Corrosion by liquid metal is generally related to the solubility of the materials involved (Berry (1971), Borgstedt and Röhrig (1991), Asher et al. (1977)). The solubility of chromium in lead is about 4 orders of magnitude higher than the solubility of iron (Guminski (1990)). This means that alloys with a low chromium content are more stable in liquid lead than steels with a high Cr content. This is in agreement with our observations. Nevertheless, EDX and REM analyses are necessary before making more detailed statements concerning the corrosion characteristics. Probably the dissolution of steel elements in lead and / or the partly leaching out of one or more components out of the steel matrix are responsible for the corrosion attack. Further investigations on specimens exposed to lead for 3.000 h, 5.000 h and 10.000 h are in progress.

2.3.1.2 Stagnant corrosion experiments with oxidation protection

Introduction:

In contrast to the stagnant corrosion experiments of chapter 2.3.1.1, this chapter describes the stagnant corrosion experiments which consider an oxygen protection for the steel specimen. These experiments are performed in the stagnant experiment COSTA which is described in detail in chapter 2.1.1. A flow diagramme of COSTA is given in figure 5. The oxygen control system (OCS) which is applied to control the oxygen partial pressure in the liquid metal is described in chapter 2.1.3 (stagnant experiment KOCOS) and chapter 2.4 (sub-project 3).

Experimental Setup:

The steel specimens are dipped in crucibles which are filled with 40 g of high purity lead. In total, there are 10 crucibles for one COSTA experimental setup, each setup taking a maximum of 20 specimens. The lead within the crucibles is stagnant. The crucibles are set up within a quartz tube (reactor). The quartz tube is located within a furnace and set at a temperature of 550°C. To control the oxygen partial pressure in the liquid lead the OCS is applied: a mixture of Ar and Ar5%H_2 allows to adjust the hydrogen concentration in the gas; water vapor is added by passing the gas through water of a definite temperature. The maximum hydrogen concentration to be introduced is 5 %, which is well below the lower explosion limit. In the actual experiments, the ratio of Ar and Ar5%H_2 is 200 / 16 cm^3min^{-1} which gives a H_2/H_2O ratio of 0.4 at a water temperature of 7.4°C.
The maximum exposure time completed up to now is 3.000 h. The samples immerge about 1 cm deep into the liquid lead during the test. After the test, the adherent lead is not removed from the specimen surface in order to conserve a possible oxide scale. Specimens are examined by cutting them perpendicular to the surface and looking at the cross section by microscope and SEM combined with an EDX (energy disperive X-ray analysis) analyser. The SEC (standardless element concentration) factor for oxygen was estimated by a reversed ZAF-calculation from polished Al_2O_3 and ZrO_2 ceramics covered with the same carbon coating as that on the analyzed specimens. Examinations are carried out after 800 h, 1500 h and 3.000 h of exposure.
The oxide scale grown at the surface of the specimens is also analyzed by X-ray diffraction. Because the specimens are difficult to clean from adhering lead, the analysis is done with specimens which were exposed to the controlled atmosphere in the furnace close to the lead crucibles. These specimens show about the same features and oxide scale structure as they are observed with those in lead. However, the growth rate of the magnetite scale is enhanced by a factor of 2-3 in the gas atmosphere.

Results:

After the corrosion test in liquid lead of 550°C under controlled Ar-H_2/H_2O-atmosphere in COSTA, the specimens are taken from the test stand for metallographic examination and concentration analysis. Specimens and test data are listed in table 7. Specimens F2, F3 and A2, A3 were surface treated by the GESA process, Müller et al. (1996, 1998), Knebel et al. (2000). At F2 and A2 a 20 µm surface layer was restructured by one electron pulse. Aluminium Al was alloyed into the surface of F3 and A3 by the same process.

Table 7: Materials and test data after maximum exposure to lead at 550°C containing $8 \cdot 10^{-6}$ at% oxygen.

material data			test data			
Spec. No.	Type	Treatment	t_{tot} [h]	Mag. scale [µm]	sp. zone [µm]	diff. zone [µm]
F1	OPTIFER IVc	original	3000	20	15	10
F2		e - pulse	3000	16	15	8
F3		Al - alloyed	1500	None	none	none
A1	1.4970	original	3000	10	6	12(1)
A2		e - pulse	3000	6	6	3(1)
A3		Al - alloyed	1500	None	none	none

mag. = magnetite; sp = Fe (Fe, Cr)$_2$ O$_4$; diff. = diffusion; e-pulse = pulsed electron beam, GESA;
(1) including grain boundary penetration

The cross section of the original OPTIFER IVc specimen F1 after exposure is presented in figure 69 together with the concentration profiles that are recorded as a function of the distance from the original specimen surface. The micrograph of the cross section shows the typical corrosion attack with three different zones. The zone at the top, that ends at the original specimen surface, consists of magnetite without appreciable Cr - concentration. It is obviously brittle, because many defects, caused by spallation of scale parts, exist. The layer in the middle contains Cr-Fe spinel that roots in the pore belt. At some places the spinel layer is also missing, an effect that is more pronounced at other places of the specimen. In the interior, an oxygen diffusion zone can be observed in which oxides precipitate along the grain boundaries.

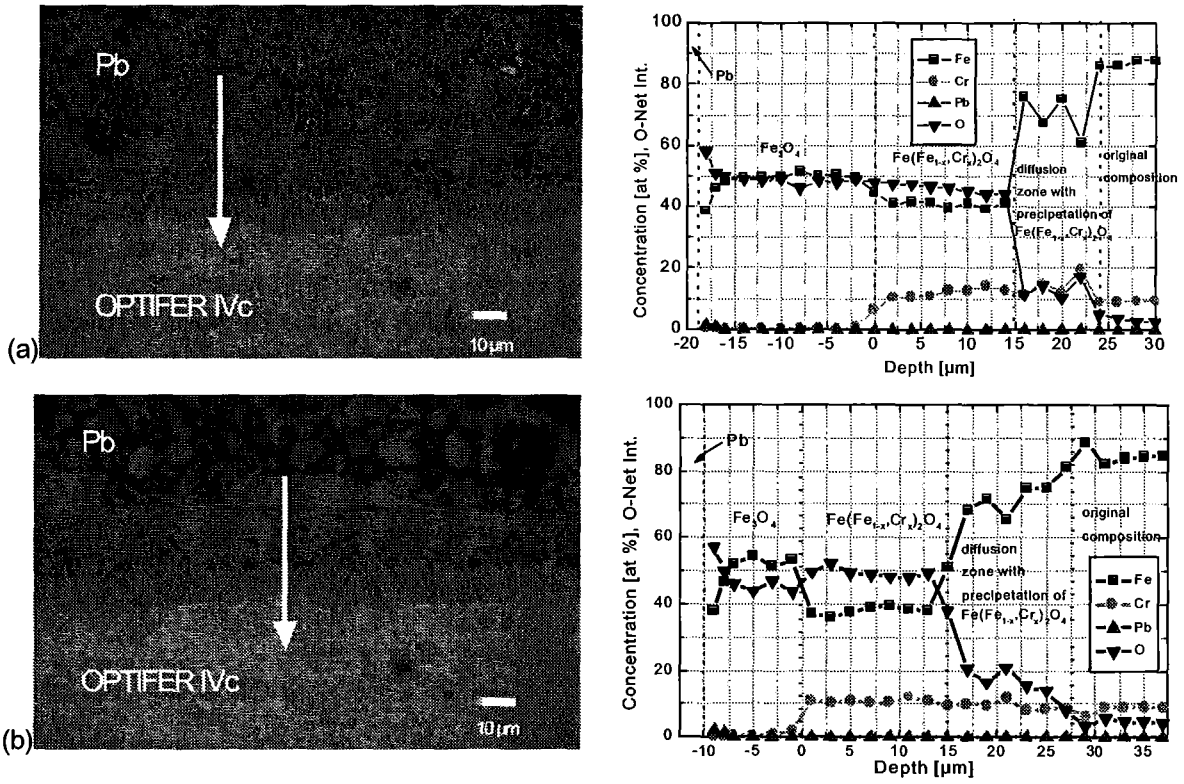

Figure 69: Micrograph of cross section of OPTIFER IVc specimens and eDX concentration profiles after 3.000 h at 550°C.
(a): original, F1, (b): GESA treated, F2.

The concentration profile in figure 69a indicates the zone structure as well. Both oxide layers are hypostoichiometric with O/M ratios of around 1 for the oxides. Only at the scale surface the O/M ratio was higher and reached a value of 1.3. The concentration in the diffusion zone is about 10 % of that in the magnetite scale. Peaks in this zone indicate spinel precipitation in a grain boundary. Within the spinel zone, the Cr - concentration reaches a maximum of twice the concentration in the bulk due to Fe depletion caused by the magnetite scale formation.
Specimen F2 which was treated by an electron pulse before the test, shows the same features, as the non treated specimen F1. Different is the size of the magnetite scale which is smaller and more compact than on the untreated surface but is also partially spalled off, figure 69b. Furthermore, the spinel layer is completely retained without spallation.
For demonstration of the effect of Al-alloying into the surface, specimen F3 is alloyed with Al by electron pulse treatment only on one half of the surface, figure 70. There is no corrosion attack visible in the alloyed part (left) at all after 1.500 h exposure to liquid lead at 550°C.

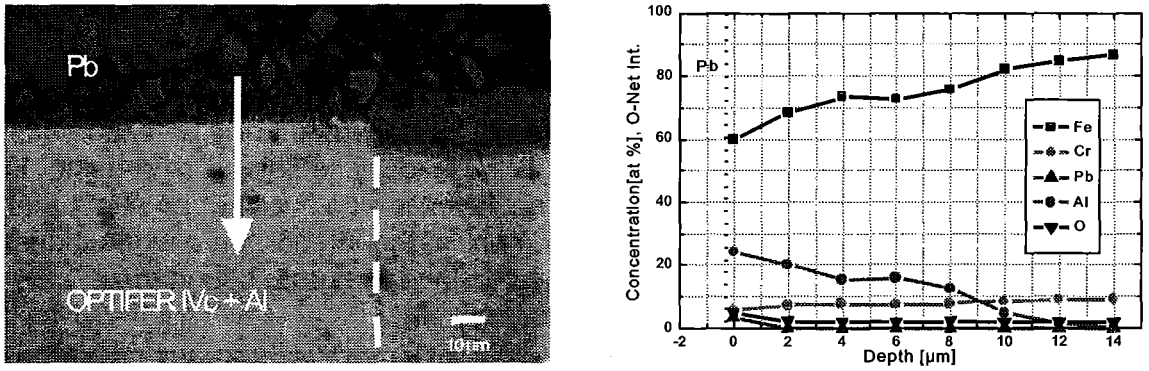

Figure 70: Micrograph of the cross section of OPTIFER IVc specimen F3 alloyed with Al on the left surface part and eDX concentration profiles through the alloyed surface layer after 1500 h at 550 °C.

The concentration profiles do not give any indication of an interaction between lead or oxygen and the alloyed specimen part. Only the unalloyed part of the surface to the right is covered with thick oxide scales. It is obvious from this micrograph that the Fe-Cr spinel layer ends at the original specimen surface. The development of the magnetite scale is also examined by X-ray diffraction. Figure 71a represents diffraction patterns of the OPTIFER IVc specimen F1 after exposure to the atmosphere in the test furnace for times up to 500 h. The peaks of α Fe disappear already after 110 h and get replaced by magnetite and/or spinel peaks marked by 'M' (magnetite).
Intensity changes of those peaks during exposure indicate a reorientation of crystals in the oxide scale. Besides the magnetite peaks there are several others marked by 'H' (hematite) that only can be fitted by data of Fe_2O_3 and $(Fe, Cr)_2O_3$. Those peaks are steadily increasing and indicate a growing part of this phase.
Scale development on the electron pulse treated OPTIFER IVc specimen F2 shows essentially the same features as observed on the original specimen F1, Figure 71b. The only difference is in the starting material (0 h), where a reoriented structure can be seen as described before.
A completely different behavior is visible from the X-ray spectra of the surface of the specimen F3 alloyed with Al at the surface, figure 71c. Even after 500 h of oxidation

there exist no peaks of magnetite, spinel or Al_2O_3. The alumina layer is still too small to give clear peaks and the peaks of α-Fe(Al) are not diminished. The only change is an intensity shift between the two mayor peaks probably because of thermal restructuring.
The structure of the oxidation region in the original 1.4970 steel specimen A1 is similar to that in OPTIFER IVc with layers of magnetite and Fe-Cr-spinel and an oxygen diffusion zone in the interior.

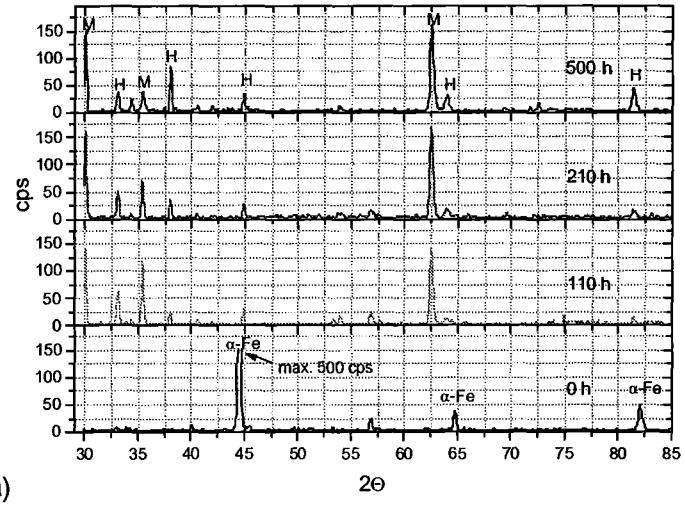

(a)

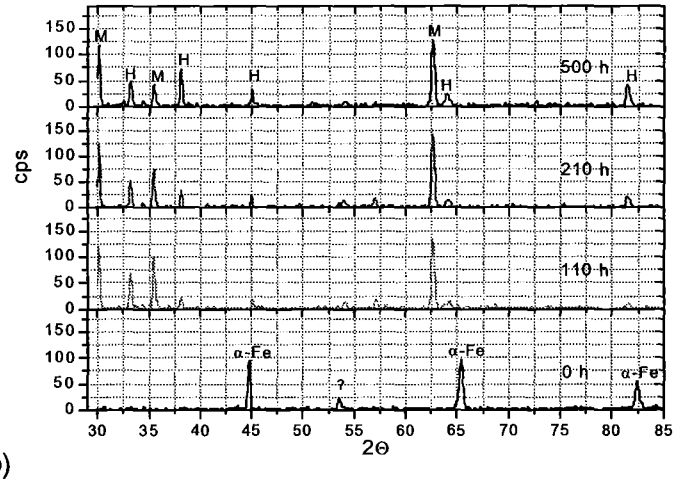

(b)

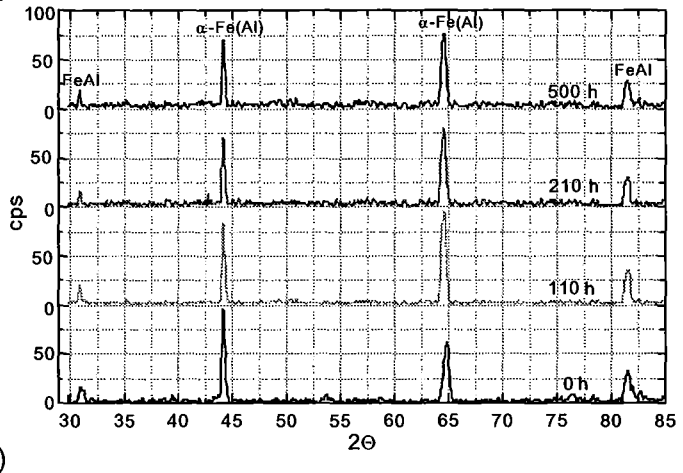

(c)

Figure 71: X-ray diffraction patterns of OPTIFER IVc specimens after oxidation at 550°C in COSTA with an H_2/H_2O ratio of 0.4.

(a) Specimen F1 (original),
(b) Specimen F2 e-pulse),
(c) specimen F3 (Al-alloyed).

M = magnetite, H = hematite.

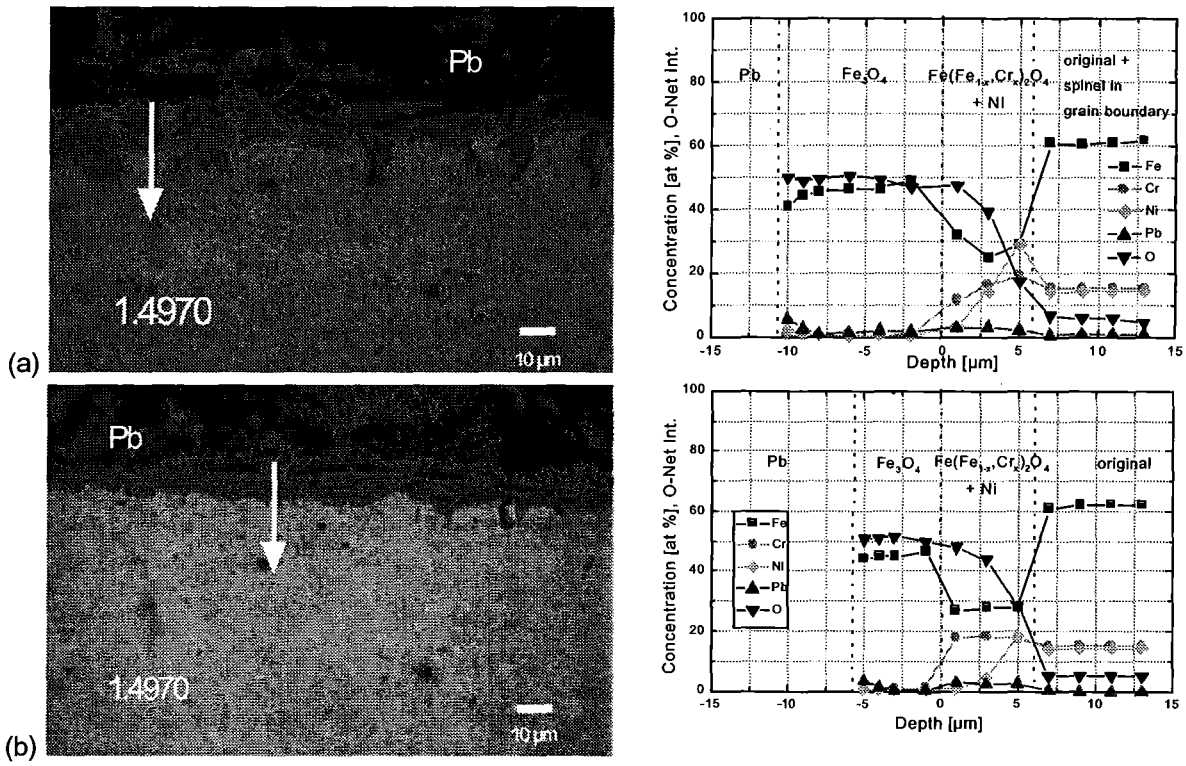

Figure 72: Micrograph of the cross section of 1.4970 specimens and eDX concentration profiles after 3.000 h at 550°C.
(a): original A1, (b): GESA treated A2.

As can be seen in figure 72a, the Fe-Cr-spinel zone contains Pb and oxygen penetrates along grain boundaries up to 20 µm deep into the metal matrix. Here it has to be mentioned that a remarkable depletion of Ni within the spinel zone takes place that is observed after 800 h of exposure and that does not change markedly since that time.
The oxygen diffusion zone is much smaller with the electron pulse treated specimen A2 than in A1, because it does not show the deep grain boundary attack, figure 72b. The Pb-containing spinel layer looks tighter and smaller and is strongly depleted in Ni. Most of the magnetite layer got lost.
There is no attack observable from the concentration profiles of the Al-alloyed austenitic specimen A3, figure 73. No oxygen penetration through the surface and no Ni-depletion took place. The micrograph does not show any signs of corrosion.

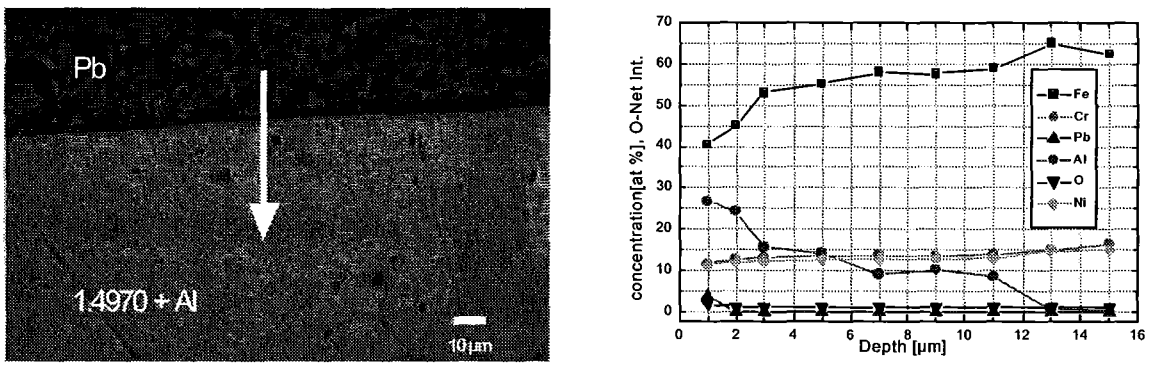

Figure 73: 1.4970 alloyed with aluminum after 1.500 h at 550°C in liquid Pb.

X-ray examination of austenitic specimens did not result in new findings and are not presented here. The only difference to the OPTIFER IVc material is the lower growth rate of the magnetite peaks, because after 500 h there are still α-Fe peaks visible.
Experiments were started in COSTA to examine the influence of Bi in a liquid Pb-Bi alloy on the corrosion behavior of steels. For this purpose OPTIFER IVc was exposed to Pb and the eutectic Pb-Bi alloy at an oxygen concentration of 8×10^{-6} at% and 550°C. After 800 h severe attack can be observed after exposure to Pb-Bi (figure 74a) while on the specimen exposed to Pb a homogeneous dense oxide layer of ~13 µm appeared (figure 74b).
The dissolution attack of Pb/Bi extends up to 20 µm deep in the base material and proceeds along the grain boundaries. No dissolution attack is visible at the specimen exposed to Pb.

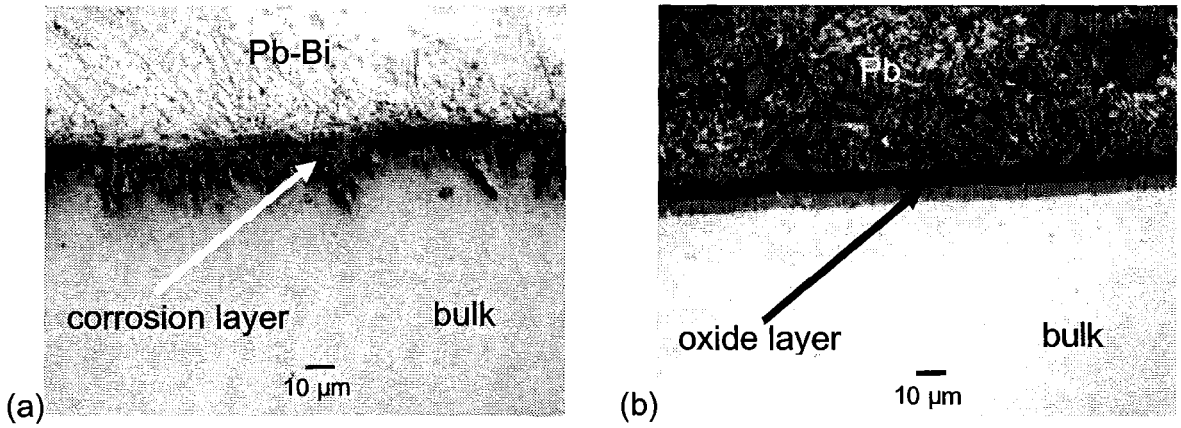

Figure 74: Comparison of corrosion effects on OPTIFER IVc steel after exposure to Pb-Bi (a) and Pb (b) at 550°C after 800 h with $8 \cdot 10^{-6}$ at% oxygen.

Discussion of the Results:

The examination of the corrosion tests with OPTIFER IVc and 1.4970 steel specimens prove that the behavior of these materials in liquid lead differs with differing treatment of the surface. Large oxidation layers are formed at the unalloyed OPTIFER IVc surface. The oxidation layers are smaller at 1.4970. No oxidation attack can be observed on both steel surfaces when alloyed with Al.
The behavior of 1.4970 specimens differ substantially from OPTIFER IVc , although the stratified scale structure is the same. The magnetite scale is much smaller than that of OPTIFER IVc, if it is visible at all. The same holds for the spinel zone and the diffusion zone with exception of the deep grain boundary penetration of oxygen in the nontreated specimen A1 in Fig. 10a. The low oxidation rates are caused by the higher oxidation resistance of high alloyed steels.
As opposed to OPTIFER IVc, 1.4970 shows Pb-inclusions in the interface region between the magnetite scale and the spinel layer that reaches frequently into the spinel, Figs. 10a,b. This effect depends obviously on the presence of Ni in the initial stage of scale formation when Ni is dissolved by liquid lead which gets trapped by the growing magnetite scale and solidifies with about 2 at% of Ni, Massalski (1990). After this process the Ni depletion does not change any more with increasing exposure time. Thus, the Ni depletion zones in Figs. 10a, b represent the state established in the time before the first examination at 800 h of exposure.
The influence of electron pulse melting of a surface layer of the steels on the corrosion behavior in liquid lead at 550°C up to 3.000 h exposure time manifests in

some more or less important effects. In OPTIFER IVc it causes a smaller magnetite scale and better spallation resistance of the spinel zone, while in 1.4970 the deep grain boundary penetration of oxygen is avoided. The reason for this behavior is thought to be the much finer grain structure in the specimen surface layer after melting and rapid solidification. However, whether there will be a benefit of this effects for the corrosion behavior can not yet be said with confidence. Tests with much longer exposure times and experiments in loops with flowing liquid metal will be necessary to attain confidential statements.

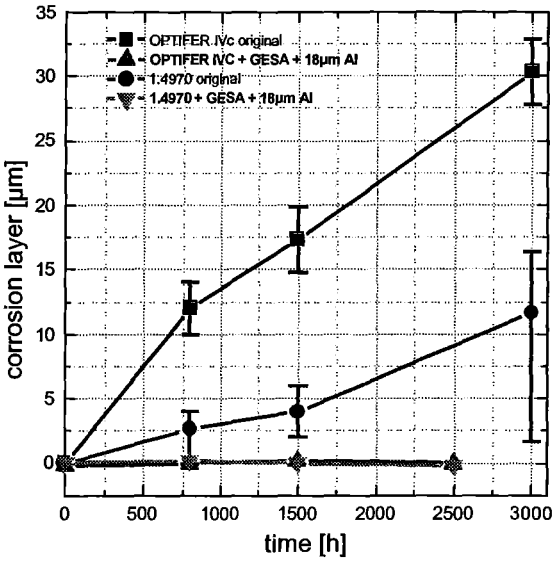

Figure 75: Growth rate of the corrosion layers for original and GESA treated OPTIFER IVc and 1.4970.
The growth rate for Al-alloyed specimens is practically zero.

In the comparison of OPTIFER IVc and 1.4970, the austenitic material should be favored so far after 3.000 h of testing, especially when the surface is treated by GESA. The corrosion zone consisting of the spinel layer and the diffusion zone is much smaller after that time. Figure 75 shows the growth of the corrosion zones in both steels with and without surface treatment. The points represent the mean values of 5 measurements, each one obtained at a different position parallel the surface. At least for the first 3000 h it indicates the better performance of 1.4970 with advantages for the surface treated specimen. No visible advantage of surface treatment can be observed for the OPTIFER IVc specimen. The fragile magnetite scale is not considered in the evaluation because it constitutes a corrosion product that lies above the original specimen surface and is lost in the greatest part of the surface area. This effect will be enhanced by the flowing lead in loops.
The most striking effect is obtained with both steels, OPTIFER IVc and 1.4970, when Al is alloyed into the surface layer during melting by GESA. The alumina layer that must have been formed at the surface during oxidation in lead with $8 \cdot 10^{-6}$ at% of oxygen is very thin and could not be detected up to now. However, it constitutes such an effective barrier against corrosion that up to 1500 h not even a minimal attack occurred. This agrees with investigations of the behavior of aluminized steel in liquid Pb-17 Li in tests with 10.000 h exposure time (Borgstedt and Glasbrenner (1997)) and with tests of the corrosion behavior of FeAl in liquid lead at 600 °C, Asher (1977).
An experiment shows that the Pb-Bi alloy is much more aggressive than pure Pb. This may be reasoned by the much higher solubilitis of steel components in Bi listed in table 8. The competition between oxide scale formation and dissolution could shift in this case in favor of dissolution. A possible counter measure could be the application of a higher oxygen potential, i.e. the oxygen concentration in the alloy. This is the goal of ongoing experiments.

Table 8: Solubility of steel components in Pb and Bi at 600°C.

	Bi (at 600 °C) [at%]	Pb (at 600 °C) [at%]
Ni	21	2
Cr	0.056	0.02
Fe	0.017	0.001

Conclusions:

Oxide layers on the steel specimens can effectively prevent alloy components to be leached out of the steel by dissolution in liquid lead. To maintain the oxide layers over long exposure time it is necessary to control the oxygen concentration in lead which can be done with a gas atmosphere of 10^{-22} to 10^{-25} bar of oxygen partial pressure. By this procedure the corrosion attack is changed from that of liquid metal corrosion to that of oxidation. Thus, it is needed to find materials that form stable protective oxide scales under oxygen control in liquid lead.

Among the two steels OPTIFER IVc and 1.4970, the austenite 1.4970 shows better resistance in liquid lead under oxygen control than OPTIFER IVc. This is a consequence of the better oxidation resistance of 1.4970.

Electron pulse treatment (GESA) improves the behavior of 1.4970: due to the fine grained structure that forms by rapid melting and solidification, it suppresses deep grain boundary penetration of oxygen.

Alloying of aluminum into the surface by pulsed electron beam surface melting improves the corrosion oxidation behavior of both examined steel types in an impressive manner. No corrosion attack at all is observed after 1.500 h of exposure.

The eutectic Pb-Bi alloy causes severe dissolution attack and is, therefore, much more aggressive to steels than pure liquid Pb, considering the same oxygen potential which is applied in liquid Pb. A higher oxygen potential could be a solution and will be investigated next.

2.3.1.3 Dynamic corrosion experiments with oxygen control

Introduction:

Within the reported period, some corrosion experiments have been carried out in collaboration with IPPE in Obninsk, Russia. Two ferritic-martensitic and two austenitic steels in original condition and with a surface treatment by GESA were exposed to Pb in a loop at 400°C and 550°C resp. for 1027, 2000 and 3000 h, respectively. First results of specimens exposed for 1027 h are already available and are discussed here.

Material and specimen preparation:

Different types of steel were selected for corrosion tests in the Pb loop: two ferritic-martensitic steels (Optifer IVc and EM10) and two austenitic steels (1.4948 and 1.4970). The two ferritic-martensitic steels were developed as low activation steels to be used as structural materials in a common fusion reactor. Optifer IVc was developed in Forschungszentrum Karlsruhe, EM10 is an Italian development. Both austenitic steels are highly resistant to elevated temperatures. Large experience exists on the steel 1.4948 which was used for tubes, pressure vessels and other structural components in sodium cooled fast breeder reactors.
The chemical composition of these steels is given in table 9.

Table 9: Chemical composition of the steels tested in Pb (wt.-%).

Material	C	Mn	Si	Cr	Ni	Mo	W	V	Nb
1.4970	0.08-0.12	1.6-2.0	0.25-0.45	14.5-15.5	15-16	1.05-1.25	--	--	--
1.4948	0.04-0.08	0-2.0	0-0.75	17-19	10-12	--	--	--	--
Optifer IVc	0.13	0.52	--	9.05	--	--	1.0	0.25	--
EM 10	0.10	0.51	0.37	8.8	0.2	1.0	--	0.03	0.01

The specimens to be tested were machined at Forschungszentrum Karlsruhe before delivering to IPPE. The specimens have a cylindrical shape (see figure 76) with a total length of about 110 mm and a diameter of 8 mm. The original specimens were not heat treated before exposure. Some specimens were treated by GESA (Pulsed Electron Beam Facility GESA, see chapter 2.3.3) on approximately one third of the total length. The rapid solidification after the pulse with about 10^7 K/s results in a very fine grained structure. The GESA installation is described elsewhere, Müller et al. (1996). In this work the corrosion behaviour of original and GESA treated specimens will be examined in flowing Pb.

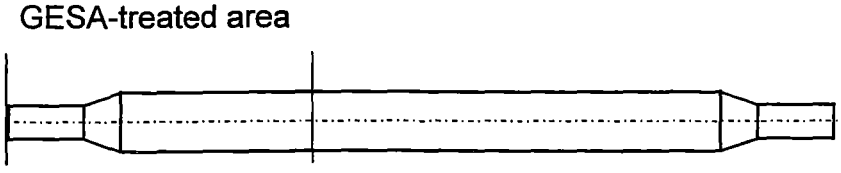

Figure 76: Shape of the specimens exposed to flowing Pb. Some materials were treated by pulsed electron beam (GESA).

The degreased samples were weighed before the corrosion testing. After the exposure, the specimens were washed to remove adherent Pb at 170 to 180°C in a special fluid which is not interacting with steels and oxide films.

Lead corrosion loop:

The corrosion tests were carried out in a non-isothermal forced lead loop at IPPE Obninsk. It consists of a main heater, a cooler, a hot and a cold test section, an electromechanical pump, a purification system, a flow meter and two oxygen meters. Two test sections are available, one at 400°C, the other at 550°C.
The volume of the liquid lead in the loop is about 60 l, the flow velocity at the specimens is 1.9 m/s. The temperature of the lead is maintained by electrical resistance heating. The heater part is positioned just upstream of the hot test section. For cooling the circulating lead, a three-wall cooler construction is applied: cooling water – stagnant Pb-Bi alloy – pumped lead.
The loop consists of tubes with 30 x 4 mm in diameter. The tubing of the hot part is made of austenitic chromium nickel 20Cr14Ni2Si steel whereas the cold part (less than 460°C) is made of ordinary austenitic stainless steel 18Cr10Ni1Ti.
In the present corrosion test the oxygen content in the lead was monitored by two oxygen meters placed in the two temperature zones. The oxygen activity in the liquid lead is measured by the electrochemical cells of the oxygen meters. The error of the E.M.F. measurements in the Pb-O system does not exceed 2%.

Experimental conditions:

The specimens to be tested were fit together in the test sections with fixing their tails by pins in adapter bushes and in upper and bottom grids. The temperature of the hot test section was 550°C, the temperature in the cold test section was 400°C. The concentration of oxygen dissolved in the liquid metal was about $3-4 \times 10^{-5}$ wt.-%. The exposed materials and the corresponding test conditions are summarised in table 10. Specimens were washed after exposure to remove residues of lead.
The applied analysis techniques consisted of:

- weighing of the cleaned specimens,
- X-ray spectral microanalysis of the surface of the specimens,
- metallurgical examination,
- EDX line scan analysis on the cross-sections of the specimens.

Table 10: Materials exposed to flowing lead at 400°C and 550°C.

Material	400°C	550°C	400°C	550°C	400°C	550°C
1.4970	1027 h	1027 h	2000 h	2000 h	3027 h	3027 h
1.4970 - GESA	--	1027 h	--	2000 h	--	3027 h
1.4948	1027 h	1027 h	2000 h	2000 h	--	3027 h
1.4948 - GESA	1027 h	1027 h	--	2000 h	--	3027 h
Optifer IVc	1027 h	1027 h	2000 h	2000 h	3027 h	3027 h
OptiferIVc-GESA	--	1027 h	--	--	--	--
EM 10	--	1027 h	--	--	--	3027 h

Results:

The cleaned specimens showed no sign of damage by dissolution attack. The visual inspection revealed an oxide formation with varying thickness on the surface of each specimen. Austenitic steels exposed to lead up to 2000 h still have a golden shiny surface even when exposed to 550°C, which indicates the existence of a thin oxide layer. With increasing exposure time the colour of the surface turned darker, but even then it was still shiny. The surfaces of the ferrites (GESA treated and untreated) and also the GESA treated austentic steels were black coloured without any shiny area, i.e. thick oxide layers were formed.
X-ray diffraction patterns obtained from the surface of the ferritic steels showed the formation of the compound Me_3O_4 already after 1000 h of exposure at 400°C and 550°C. No other compounds could be detected even after longer exposure time. In contrary to this, oxide patterns were not visible in the spectra of the austenitic steels, because the oxide layers were too thin.
Metallurgical examination of these steels showed an oxide layer thickness of about 2 µm after 3000 h of exposure at 550°C (see figure 77). This prevents the dissolution corrosion attack of the liquid lead at least during the limited time of exposure.

50 µm

Figure 77: Metallurgical examination of 1.4970 specimen after 3000 h at 550°C.

A two phase oxide scale was found on all austenitic steels treated by GESA. Both layers vary in thickness. The adherence seems to be very good. The cross sections of GESA treated 1.4970 and 1.4948 steels after 3000 h of exposure at 550°C and the corresponding EDX concentration profiles are presented in figures 78 a,b and 79 a,b. The external layer has a composition of pure magnetite which is in agreement with the X-ray diffraction results obtained from specimens exposed to stagnant lead [9]. Other steel elements like nickel and chromium are not detected. The internal layer contains iron, chromium nickel and oxygen. This corresponds to an iron chromium spinel plus nickel. The concentration of iron and chromium stays constant in the whole layer whereas the oxygen content decreases slowly and nickel increases slightly towards to the steel side. In both austenitic steels the content of chromium and nickel is higher in the internal layer than in the steel matrix because of the release of iron into the magnetite layer.

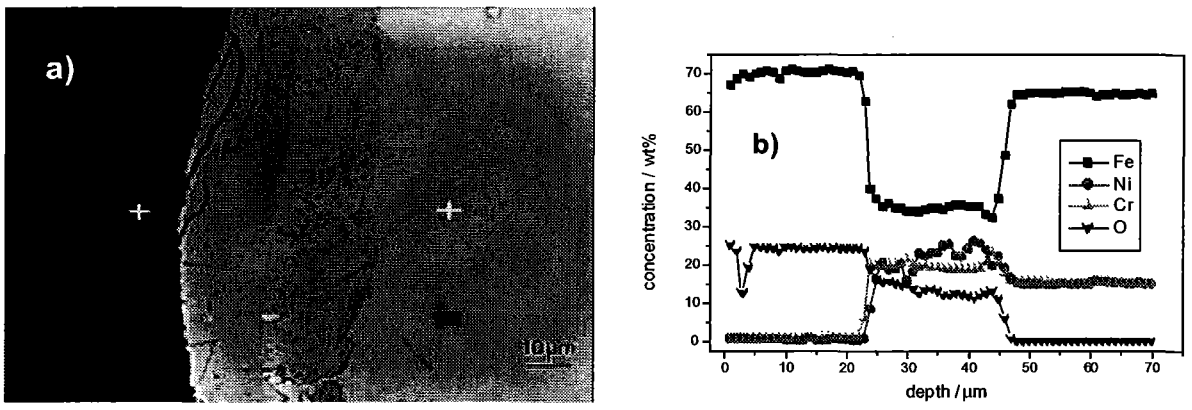

Figure 78: Micrograph of GESA-treated 1.4970 specimen cross section (a) and EDX concentration profile after 3000 h at 550°C (b).

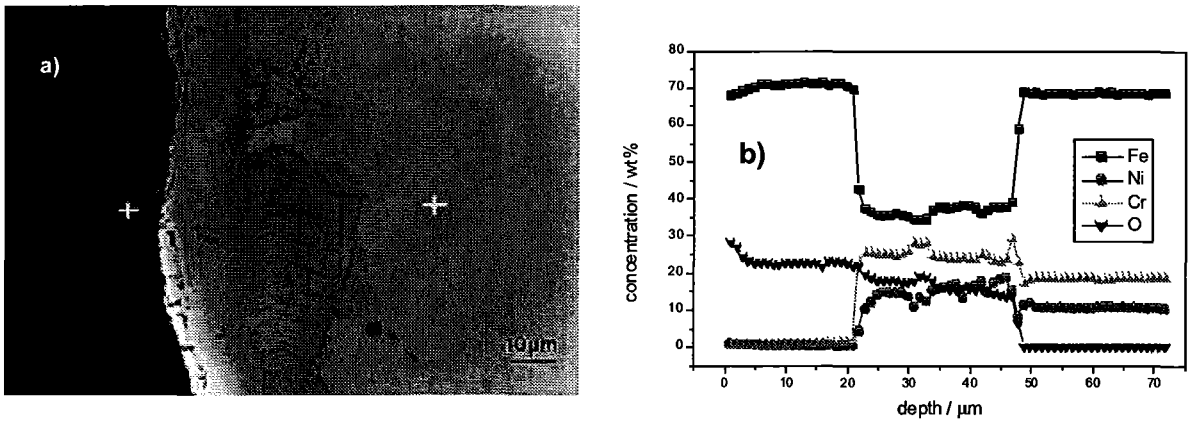

Figure 79: Micrograph of GESA-treated 1.4948 specimen cross section (a) and EDX concentration profile after 3000 h at 550°C (b).

In ferritic steels no obvious influence of the GESA treatment was observed. The EDX concentration profiles with the corresponding cross sections of Optifer IVc (2000 h at 550°C in lead) and EM 10 (3000 h at 550°C in lead) are shown in figures 80 a,b and 81 a,b. The micrographs of the cross sections show the typical corrosion attack with three different zones. The zone at the top consists of magnetite without appreciable chromium concentration. The layer in the middle contains Cr-Fe spinel that roots in a porous belt. Within the spinel zone, the chromium content reaches a maximum that is 1.5 times higher than the concentration in the bulk material due to iron depletion caused by the magnetite scale formation. In the interior, an oxygen diffusion zone can be observed in which oxides precipitate along grain boundaries. In the case of EM 10 the thickness of all three zones formed is smaller than that on Optifer IVc.
The oxide layers increase with time and temperature. The largest thickness is achieved on Optifer IVc, followed by the GESA treated austenitic steel 1.4948. The steels EM 10 and 1.4970 (GESA treated) showed more or less the same growth rate. The oxide layers thickness versus exposure time in liquid lead at 550°C is given in figure 82. It can be seen that the growth of the oxides on all steels obeys the parabolic law.

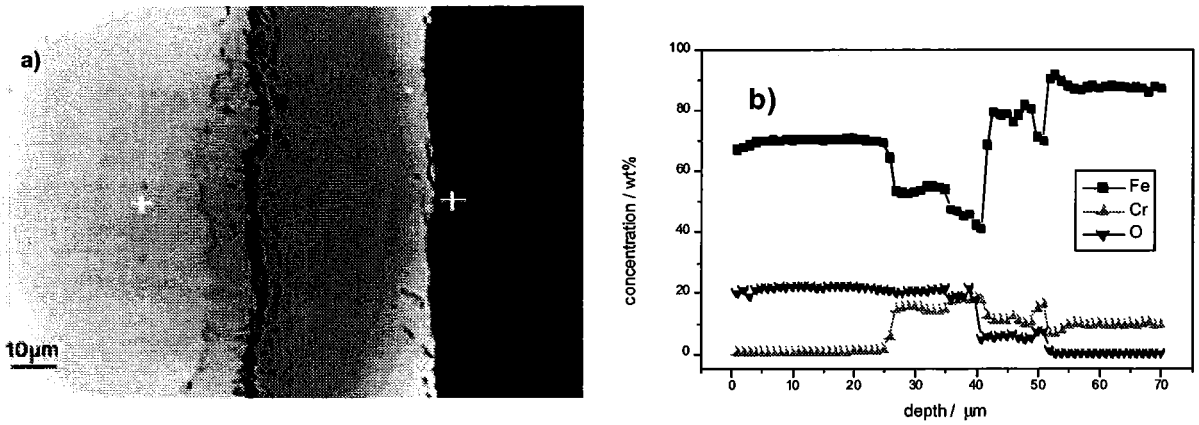

Figure 80: Micrograph of Optifer IVc specimen cross section (a) and EDX concentration profile after 2000 h at 550°C (b).

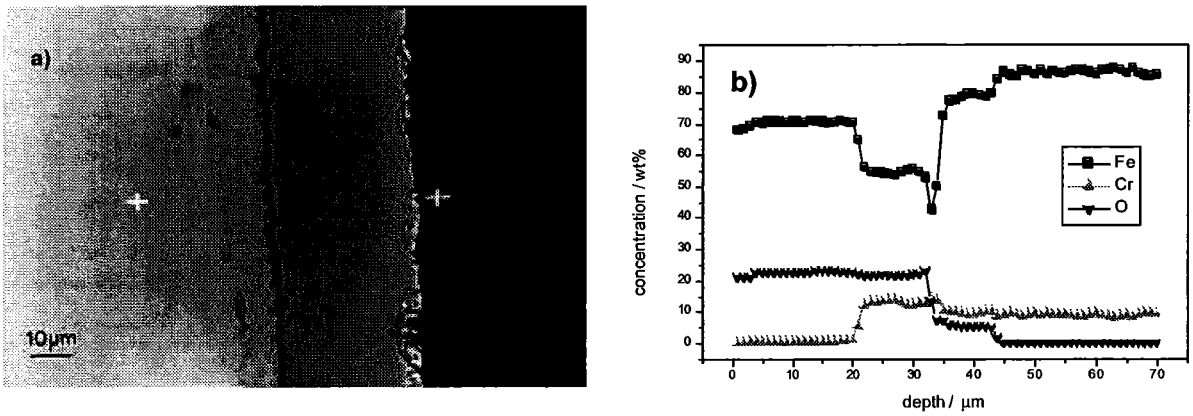

Figure 81: Micrograph of EM 10 specimen cross section (a) and EDX concentration profile after 3000 h at 550°C (b).

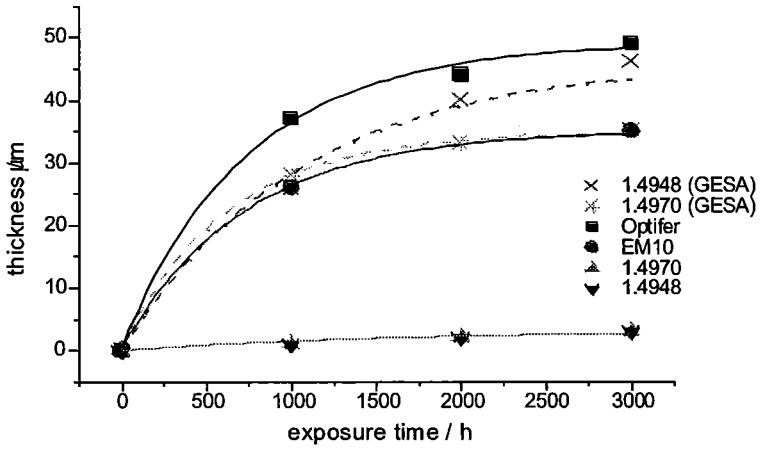

Figure 82: Total thickness of oxide layers versus the duration of corrosion tests of steels in flowing lead at 550°C.

Discussion of results:

Multiphase oxide scales were formed on the steel surfaces of the ferritic steels and the two GESA treated austenitic steels during exposure to flowing lead. The scales protect the steels against dissolution attack. Alloy components do not diffuse at the same rate in the oxide layers and the alloy. Therefore, a multiphase oxide scale is formed during oxidation of the alloys. The stratified oxide layer structure agrees with

descriptions by Hauffe (1965) and Talbot and Talbot (1998) for oxidation of steels below 570°C in air.
Three distinct oxidation zones are developed at the steel surfaces: an outer magnetite scale (Fe_3O_4) which is placed on top of the original surface. Besides Fe and O other elements do not appear in an appreciable amount in this scale. The intermediate layer below the magnetite scale consists of a spinel $Fe^{2+}(Fe_{1-x}^{3+}Cr_x^{3+})_2O_4$ (+ Ni). This layer is an oxygen diffusion zone with spinel formation along grain boundaries.
The proposed oxidation mechanism for this multiphase oxide scale can be described as follows (Kuroda et al. (1983), Gesmundo et al. (1987), Müller (2000)): firstly, oxygen reacts with iron and chromium to form the Fe-Cr spinel. Oxygen has the capability to diffuse inwards through the oxide scale and reacts with steel elements to a spinel type structure. As a result of this O-ion diffusion the Fe-Cr spinel grows inwards. The outer layer grows by Fe-ion diffusion to the surface, which creates the magnetite scale that grows on the surface. Cr diffuses more slowly and is only present in the inner part of the scale.
The thickness and composition of the multiphase oxide scales formed on the ferritic steels with and without GESA treatment do not show any difference. Hence, the additional surface treatment did not have an obvious influence on the oxidation behaviour of Optifer IVc and EM 10. Not so for the GESA treated austenitic steels 1.4970 and 1.4980 in which multiphase oxide scales were developed like observed for the ferritic steels. In the case of untreated austenitic steel surfaces a thin dense oxide layer was formed.
All the oxide scales developed on the examined steels provide a good protection against the dissolution attack at 400°C and 550°C up to an exposure time of 3.000 h in a liquid lead loop with controlled oxygen concentration. This corresponds with the results of corrosion tests in stagnant lead during the same exposure time, Müller et al. (2000). Those tests include also austenitic and ferritic steels in which aluminium was alloyed into the surface by GESA pulse heating. In this case a thin alumina scale appeared during the tests on the surface that prevented not only the dissolution attack of liquid lead but also oxidation of the steel components. This treatment may provide a better corrosion protection especially for exposure times much higher than 3.000 h.

Conclusions:

Ferritic and austenitic steels appear to be suitable structural materials for liquid lead loops up to 550°C if the dissolution attack is prevented by a dilute solution of oxygen in the liquid metal. The concentration of oxygen must be controlled at a value at which a protective oxide scale builds up at the steel surface but no PbO is formed, cf. chapter 2.4.2. Oxide scales on ferrites that develop under these conditions agree in structure with those for oxidation in air. Austenitic steels have such scales only when the surface is treated by the GESA process. Untreated austenites show only very thin oxide layers of about 1 µm. Results obtained so far are representative for exposure times up to 3.000 h. It has to be prooved whether this holds for longer exposure times and also whether the thick oxide scales provide a better protection than the thin scale observed on austenitic steel. However, oxidative corrosion may become a problem with high exposure times. Alloying of aluminum into the surface of the steels has to be considered as a prospective treatment for a protection against corrosion. This is because the alumina scale prevents not only dissolution attack but also oxidation of steel components.

2.3.2 Work Package WP2: Improvement of the Corrosion Resistivity using Surface Protection

Within this work package, the conditions which are required in order to establish a protective oxide scale formation are explained. The possible experimental working region for a loop system within a given temperature range are defined.
The concentration of oxygen in lead that is necessary for the protective oxide scale formation on steel structures, may be controlled by solid electrolyte cells that measure and feed oxygen into the liquid lead or lead-bismuth. Such cells are sophisticated and require a special know-how to build them. Another possibility to control the concentration of oxygen in the liquid metal is the control via an atmosphere with a definite oxygen partial pressure that determines the chemical potential of oxygen within the liquid metal bath. To prevent PbO precipitation and to support Fe_3O_4 formation, the following conditions must be established.

$$2\Delta G^0_{PbO} > RT\,ln\,p_{O_2} > 0.5\Delta G^0_{Fe_3O_4} \qquad (12)$$

The standard values ΔG^0 of the Gibbs energies are known for the oxides in question and with these values the equilibrium oxygen partial pressure region that retains the stable conditions can be determined. The easiest way to do this is to draw a diagram that contains oxygen potentials of the relevant oxides PbO, NiO, Fe_3O_4 and Cr_2O_3 and the lines for constant oxygen partial pressures and constant H_2/H_2O ratios as a function of temperature. The latter will be used to control the oxygen potential as follows:

$$p_{O_2} = \frac{p^2_{H_2O}}{p^2_{H_2}} exp \frac{2\Delta G^0_{H_2O}}{RT} \qquad (13)$$

Figure 83 demonstrates in which region the stable conditions exist and how the conditions can be established. The ordinate shows the chemical potential of oxygen, the abscissa the temperature. Dashed lines in the diagram represent the isobars of the oxygen partial pressure and the lines of constant H_2/H_2O ratios in the gas atmosphere above the oxidizing species or above the liquid lead that dissolved oxygen, respectively. The important region in the diagram is between the lines of the oxygen potential for PbO and Fe_3O_4 in the temperature regime of 400 to 550°C.
For working conditions with reduced corrosion a field of oxygen partial pressures has to be selected, the boundary lines of which do not cross the PbO- and Fe_3O_4-lines within the temperature regime of 400 to 550°C. Lines of constant H_2/H_2O ratios within the boarders of this field show the ratios that must be established to maintain the appropriate oxygen partial pressures.
If a H_2/H_2O ratio of 0.4 is chosen, a partial oxygen pressure of $Po_2 \approx 10^{-25}$ bar at 550°C and $Po_2 \approx 10^{-29}$ bar at 400°C will be attained. At both temperatures iron oxide but no PbO in the case of stagnant Pb is formed. If a liquid metal loop is considered, there will be no equilibration across the temperature region via the H_2/H_2O ratio but through the oxygen dissolved in Pb (Pb-Bi). In this case the variation of the oxygen potential for a constant oxygen concentration throughout the considered temperature region between 400 and 550°C has to be considered.
For calculation of the oxygen concentration c_0 in equilibrium with an oxygen partial pressure p_{O_2}, the activity coefficient γ_0 has to be known. It can be calculated from the following relation for the oxygen activity in lead a_o:

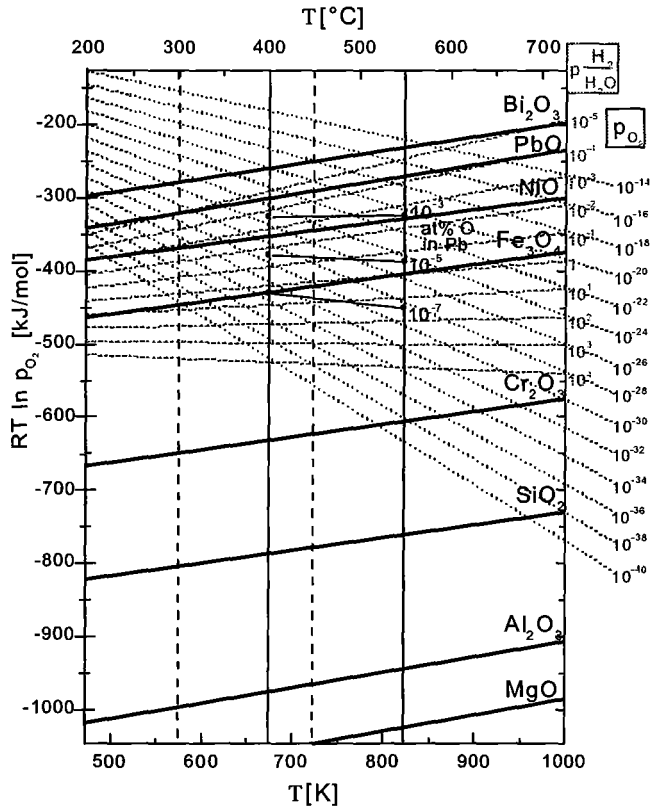

Figure 83: Oxygen potential-diagram with PbO, Fe_3O_4 and other oxides of interest containing lines of constant oxygen partial pressures and H_2/H_2O ratios. Loop temperature regions are marked for Pb by solid, and Pb-Bi by dashed vertical lines. Lines of constant oxygen concentration are drawn in the Pb loop region for 10^{-7}, 10^{-5} and 10^{-3} at%.

$$a_o = \gamma_o c_o = \frac{c_o}{c_{o,s}} = \left(\frac{p_{o_2}}{p_{o_2,s}}\right)^{\frac{1}{2}} \quad . \tag{14}$$

The suffix (s) indicates the values that correspond to saturation conditions at which the activity becomes unity.

With values for the saturation concentration of oxygen in lead of $4{\cdot}10^{-2}$ at% at 550°C and $7.5{\cdot}10^{-3}$ at% at 400°C, the equilibrium oxygen concentrations in the range of 400 to 550°C were calculated and drawn in figure 83. The solid vertical lines at 400 and 550°C mark the operating range for a lead cooled loop and the dashed lines at 300 and 450°C the one for a lead-bismuth loop. The lines of constant oxygen concentrations indicate safe regions with 10^{-3} - 10^{-5} at% oxygen for the high temperature Pb loop and 10^{-4} - 10^{-6} at% for the low temperature Pb-Bi loop. Activity coefficients for Pb and Pb-Bi do not differ much in the region above about 50 at% of Pb, Markov (1997). Therefore, the values calculated here for Pb can be extrapolated for Pb - Bi as an approximation.

The diagram in figure 83 also shows the advantage of controlling the oxygen partial pressure by the H_2/H_2O ratio. It would not be possible with an oxygen partial pressure of 10^{-25} bar to replace oxygen that was used for oxidation of the surface of the specimens in lead. However, with a H_2/H_2O ratio of 0.4 it is easy to replace the oxygen. With a gas flow of 200 cm^3/min, it is possible to provide 10 cm^3 O_2/min which corresponds to about 1000 cm^2 of a Cr_2O_3 layer of 1µm thickness. With this gas flow, delivery of the amount necessary for solution of 10^{-6} at% oxygen in 1000 cm^3 Pb would take about one second. Therefore, the controlling step is only the uptake of oxygen from the gas phase. Thus, not only small and medium loops can be managed by controlling them via the H_2/H_2O ratio in the gas phase, if one could deliver the available oxygen through the surface to the lead, e.g. by bubbling.

2.3.3 Work Package WP3: Surface Modification using the Pulsed Electron Beam Facility (GESA)

Besides surface restructuring and alloying, coating of the steel surface is a promising measure of improving the corrosion resistance. From their application in high temperature gas turbines NiCrAl alloys (MCrAlY) with aluminum concentrations of up to 12 wt% are known as very resistant by formation of protective alumina layers. Also, experiments employing a Fe aluminide layer on MANET steel, which was oxidized before the experiment to form an alumina layer, resulted in no corrosion attack in liquid Pb-17Li after 10.000 h at 450°C.
For investigation of the protective behavior of MCrAlY, cladding tubes of 1.4970 steel (8 mm diameter) were coated with a 20 – 30 µm thick layer of AMDRY 962 (Ni66 Cr22 Al10) by Sulzer Mecto, Wohlen, Switzerland. Because of the coarse particle size (≤ 11 µm) of the powder, the surface roughness of the coating deposited by the low pressure plasma spray (LPPS) process is relatively high as shown in figure 84.
Since the thin-walled tubes (0.4 mm) cannot be heated during coating large pores appear and the adherence is not satisfying. This undesired structure had to be removed to attain an effective surface protection. Restructuring of the coating layer was achieved by applying an electron pulse to the surface with GESA. By this process the coating melts together with a thin layer of the base material and solidifies rapidly by thermal conduction. The effect is a smooth surface and a nanocrystalline, dense structure of the coating with improved adhesion in the interface, shown in figure 85.

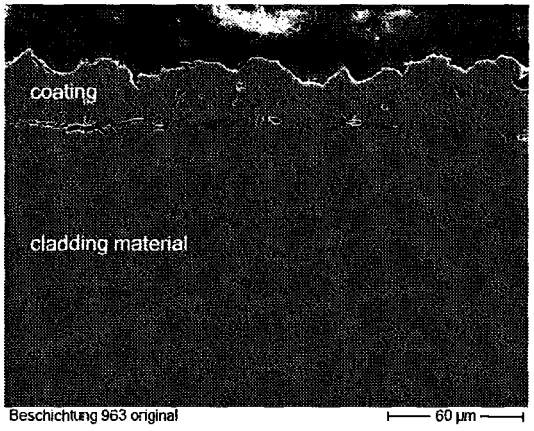

Figure 84: Ni66, Cr22, Al10 – coating on 1.4970 cladding tube.

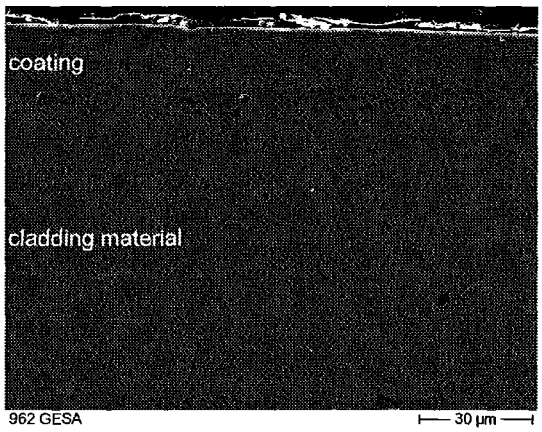

Figure 85: Ni66, Cr22, Al10 – coating after GESA treatment.

Such coating structures provide an ideal basis for formation of a dense protective alumina layer with good adhesion, as known from experiments with protective MCrAlY coatings on turbine blades. Tests with coated tubes are running since end of 2000 in loop experiments and in the stagnant experiment COSTA, see chapter 2.1.1.

2.4 Sub-Project SP3: Oxygen Control System (OCS)

2.4.1 Work Package WP1: Oxygen measurement in flowing lead-bismuth

2.4.1.1 Introduction

In the 1999 Status Report, a detailed description about the theoretical background of the electrochemical oxygen meter, the possible reference electrodes and the oxygen meter design was given. First results of measurements of the temperature dependency of the EMF of oxygen meters with Pt/air and In/In_2O_3 reference electrodes have shown that the theoretical predictions are fulfilled for oxygen saturated and pure lead-bismuth. In this report results about the response behavior of the EMF signal against changes in the oxygen concentration in the eutectic lead-bismuth and data about the long term stability of the EMF signal will be presented.
The experiments were performed in the stagnant experiment KOSIMA, see chapter 2.1.2.

2.4.1.2 Results

Figure 86 describes the response of a oxygen meter with Pt/air reference system during bubbling of reducing and oxidizing gases through the Pb-Bi melt. First $Ar+5\%H_2$, then air (p = 0.21 bar) with subsequent $Ar+5\%H_2$ bubbling was performed. The rate of the meter response to oxygen activity changes in the Pb-Bi has been found to be very rapid. The transient response to step changes of the oxygen activity in Pb-Bi exhibit no unusual behavior. The excellent time response of the EMF values after replacing of the $Ar+5\%H_2$ with air bubbling (no time delay) is obvious. By changes in the opposite direction there is some phase shift detected. The intrinsic temperature fluctuations at the beginning of the curve (Figure 86, lower part) are due to the reaction enthalpies of oxide scales degradation (oxygen removed by $Ar+5\%H_2$) and growth of oxides (air bubbling) respectively, whereas at the end of the curve only the noise level of the control unit was measured.

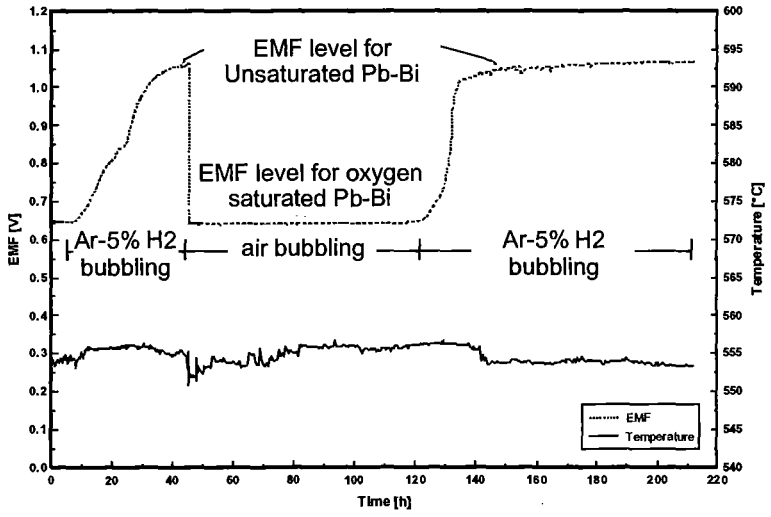

Figure 86: Changes of EMF for a cell with Pt/air reference system due to bubbling of reducing and oxidizing gases through the Pb-Bi melt.

A very similar behavior was seen for the In/In_2O_3 cell at 552°C (Figure 87). Shortly after starting of $Ar+5\%H_2$ bubbling from a intermediate oxygen level, a strong

increase of the EMF, corresponding to a decrease in oxygen activity in the Pb-Bi, was measured. After about 5 hours, an EMF level of about 0.95 V was reached, which stayed nearly constant for the rest of the bubbling period.

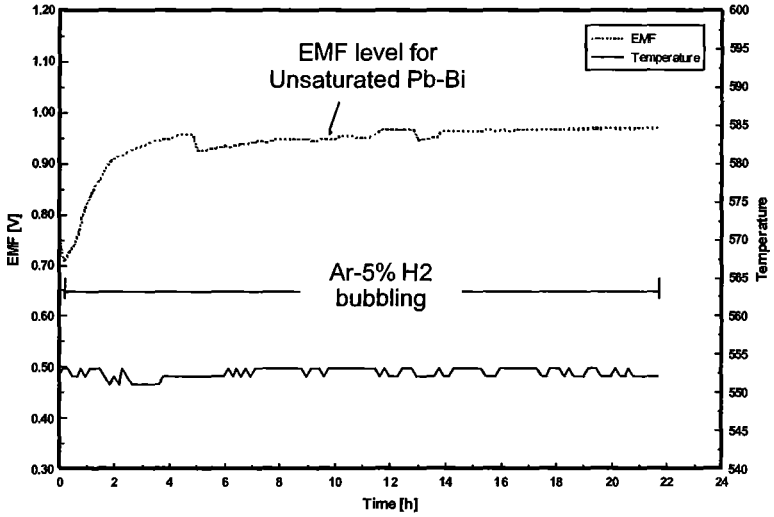

Figure 87: Change of EMF for a cell with In/In_2O_3 reference system due to bubbling of a reducing gas through the Pb-Bi.

Figure 88 shows the mid-term-stability of the EMF of a cell with Pt/air reference electrode at 555°C over about 4 months of continuous collecting of data during the immersion of the oxygen-meter in the Pb-Bi melt. Regardless of the high level of the EMF during and after the equilibration, the long-time stability within a small range of 75 mV over months without any intermittencies buried in noise seems to be very good. The ascending of the EMF at the beginning of the experiment was due to the chemical reaction of the dissolved oxygen with the steel of the container wall.

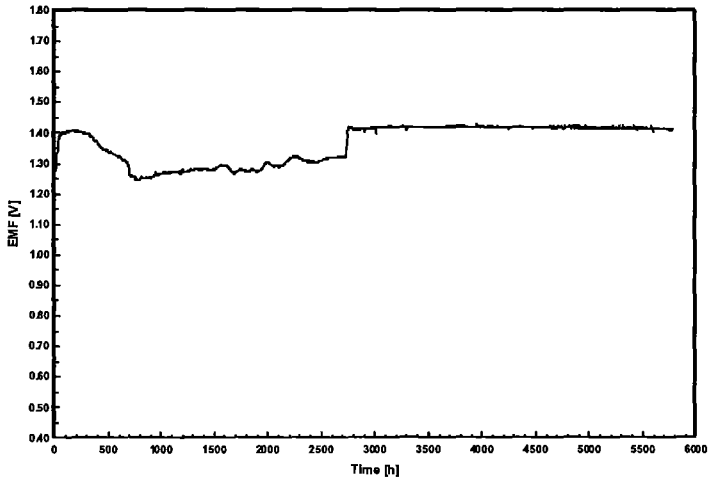

Figure 88: Mid–term behavior of EMF at 555°C for a cell with Pt/air reference system.

2.4.1.3 Conclusions

Electrochemical oxygen meters with Pt/air and In/In_2O_3 reference systems can be used as in-situ devices for measuring the chemical activity of dissolved oxygen in liquid Pb-Bi. The data obtained confirm the feasibility of using oxygen meters for the purposes of oxygen control in Pb-Bi.
The Pt/air system is a suitable reference electrode capable of maintaining stable EMF values over a long time of immersion in liquid Pb-Bi. Pt/air offers both a fast response-kinetics and a very good mid-term stability. Successful performance has

been demonstrated in a lot of experiments. Calibration slopes EMF versus temperature for Pt/air were fitting to theoretical calculations very well.
Similar results have been obtained for oxygen meters with In/In_2O_3 reference systems. The operational experiences are less good, compared to Pt/air results, regarding to the theoretical estimations. The deviations in the slopes of the EMF-temperature curves, especially in unsaturated Pb-Bi, might be due to a more pronounced sensibility to the time to reach thermodynamic equilibrium during cooling.
The current results from mid-term stability tests indicate a very satisfactory behavior for cells with a Pt/air reference system. Up to nearly 6.000 h, no degradation of the oxygen sensor was detected. Comparable results for In/In_2O_3 cells are not existing at the moment.
Sensors with both types of reference electrodes revealed an excellent response to changes in the oxygen activity of the Pb-Bi. The response time for significant reactions of the EMF was in the range of minutes. The reproducibility of this behavior was very good for cells with Pt/air reference system, when cycling between reducing and oxidizing gases.
The results from the EMF-temperature dependency tests have shown, that the minimum operational temperature of the oxygen sensor is about 400°C for Pt/air. This is much lower than the measured about 480°C for In/In_2O_3. The reason for such differences could be due to higher internal resistances of the In/In_2O_3 electrode.

2.4.2 Work Package WP2: Oxygen control in flowing lead-bismuth

2.4.2.1 Introduction

Liquid metal corrosion is a serious problem for systems using a Pb or Pb-Bi as spallation material and as coolant like an ADS system. Because of the partially high solubility of some steel components strong corrosion effects could be observed, Massalski (1990). One way to protect the metal surface is by an oxide layer that has the ability to slow down the dissolution of the protected metal components to tolerable values, Markov (1997) and Orlov (1998).
The Oxygen Control System (OCS) developed at FZK gives the possibility to control the oxygen content in the liquid metal. A detailed description is given in Lefhalm et al. (2001). As stated in Knebel et al. (2000) an oxygen concentrations between 10^{-6} at% and 10^{-7} at% in lead is desired to prevent both liquid metal corrosion and oxygen corrosion due to excessive oxidation of the steel surface.
One key question to an oxygen control system (OCS) is the physical description of its kinetics. The time which is needed to reach the desired oxygen concentration in a Pb-Bi system of a given liquid volume is crucial for the applicability to systems of industrial size.
With the OCS the oxygen concentration is controlled via a gas atmosphere above the liquid metal with a definite oxygen partial pressure p_{O_2} that determines the chemical potential of oxygen within the liquid metal. To prevent PbO precipitation and to support Fe_3O_4 formation the following condition must be established:

$$2\,\Delta G^0_{PbO} > RT\,ln\,p_{O_2} > 0.5\,\Delta G^0_{Fe_3O_4} \quad . \tag{15}$$

The standard values ΔG^0 of the Gibbs energies are known for the oxides in question, so the oxygen partial pressure that retains the stable condition can be calculated. To set the desired oxygen partial pressure in the gas phase a mixture of hydrogen and water vapour within the carrier gas argon is used. The H_2/H_2O ratio determines the oxygen potential as shown by the following relation:

$$p_{O_2} = \frac{p^2_{H_2O}}{p^2_{H_2}} exp \frac{2\,\Delta G^0_{H_2O}}{RT} \quad . \tag{16}$$

For the safe operation of a PbBi- or Pb-loop with ADS relevant temperatures the typical working conditions are between $p_{O_2}=10^{-31}$ bar at *400°C* and $p_{O_2}=10^{-24}$ bar at *550°C*, respectively. This results in a corresponding H_2/H_2O ratio of *0.4.* In the case of stagnant Pb-Bi or Pb, iron oxide is formed at both temperatures that prevents liquid metal corrosion. However, no PbO is formed. In the case of a liquid Pb-Bi- or Pb-loop (flowing liquid metal), there is no equilibrium across the temperature region via the H_2/H_2O ratio but via the oxygen dissolved in the flowing liquid Pb-Bi or Pb.

2.4.2.2 Theoretical Background

The physical process found to determine the timescale of the oxygen control process via OCS is the diffusion. The exchange of oxygen atoms through the interface between the gas phase and the liquid metal can be modelled with solutions of the diffusion equations, Fick's laws:

$$j = -D\frac{\partial c}{\partial x} \quad \text{and} \quad \frac{\partial c}{\partial t} = D\frac{\partial^2 c}{\partial x^2}. \tag{17}$$

In this case a solution can be obtained by the use of Laplace transformation. Here a rigid plane of stagnant liquid metal (height *l*) with a given oxygen concentration at the surface is assumed, which is given according to the H_2/H_2O ratio in the gas phase. The time dependent solution for oxygen sorption or desorption with a constant diffusion coefficient results in:

$$\frac{M_t}{M_\infty} = 1 - \sum_{n=0}^{\infty} \frac{8}{(2n-1)^2\pi^2} exp\left\{-\frac{D(2n+1)^2\pi^2 t}{4l^2}\right\}, \tag{18}$$

where M_t is the amount of oxygen exchanged between the gas phase and the liquid metal in the time t according to the concentration difference. In /4/ the value for the diffusion constant D of oxygen in liquid lead is given as $D=1.2\cdot10^{-5}$ cm^2/s. With this value a change of the H_2/H_2O ratio from 0.57 (equivalent to $8.85\cdot10^{-7}$ at%) to 0.19 (equivalent to $2.66\cdot10^{-7}$ at%) in the gas phase results in a duration of about 2 hours for desorption of oxygen at the surface.
However this model seems to be too simple to describe the experimental findings. Further calculations with more complex boundary conditions (stagnant liquid metal plane with variable oxygen concentration on the surface with respect to the concentration-dependent diffusion coefficient) were made. The final solution (Jost (1970), Crank (1975))

$$\frac{M_t}{2lc_1} = 1 - \sqrt{\frac{D}{\beta l^2}} tan\sqrt{\frac{\beta l^2}{D}} e^{-\beta t} - \frac{8}{\pi}\sum_{n=0}^{\infty} \frac{exp\left(-D(2n+1)^2\pi^2 t / 4l^2\right)}{(2n+1)^2\left[1-(2n+1)^2(D\pi^2/4\beta l^2)\right]} \tag{19}$$

fits the experimental results, see figure 90.

2.4.2.3 Results

The oxygen control test stand KOCOS (Kinetics of Oxygen COntrol Systems), see chapter 2.1.3, is installed within the KArlsruhe Lead Laboratory. KOCOS allows the investigation of kinetics of the oxygen control process via the gas phase as described above in theory. A mixture of Ar and $Ar/5\%H_2$ allows to adjust the hydrogen concentration in the gas. The water vapour is added by passing the gas through water at a given temperature. By changing the gas flow of $Ar/5\%H_2$ the H_2/H_2O ratio can be controlled. The gas is guided through a chilled mirror moisture sensor and over the surface of 680g stagnant liquid Pb-Bi at a constant temperature of 430°C. The liquid metal is held in a crucible of aluminium oxide to prevent contact to the steel wall of the oven. So it is ensured that no oxide formation other than PbO can take place. The moisture and the oxygen partial pressure in the escaping gas is measured. A constant total gas flow rate of 18 l/h is set.
For the experimental investigations a stepwise change of the H_2/H_2O ratio from 0.053 to 1.725 is established and observed until thermodynamic equilibrium is reached (figure 89). Due to limitations in the sensibility of the measurement equipment for the oxygen partial pressure in the gas phase, one has to take into account that the concentration in the liquid metal bath is not homogeneous throughout the bath, even when the thermodynamic equilibrium on the interface seems to be already stable. Therefore the given results are related to the exchange of oxygen at the interface

between the gas phase and the liquid Pb-Bi only. However, this is the process that determines the kinetics of the gas phase oxygen control system (OCS).

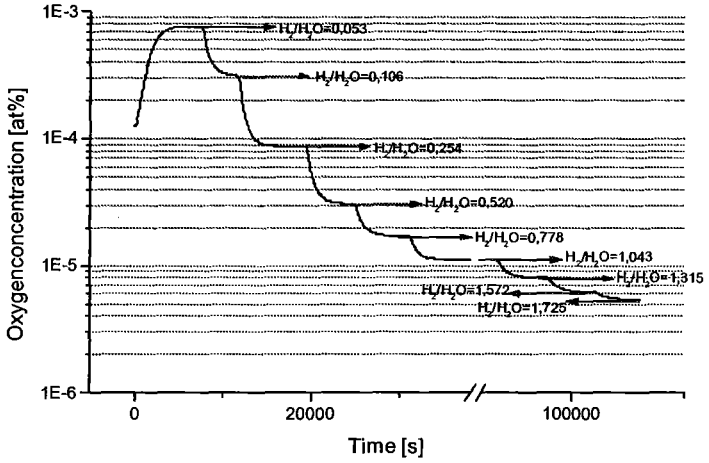

Figure 89: Oxygen concentration versus time for a stepwise change of the H_2/H_2O ratio.

Beside the issue that the oxygen control process is reversible in time, three important results have been found. First, the measured values for the H_2/H_2O ratio in equilibrium conditions are in very good agreement with the values calculated from the given gas flows and dew point (moisture). The error is less than 2 %. So the control of the partial oxygen pressure is guaranteed even at low gas flow rates, especially for hydrogen (figure 90).

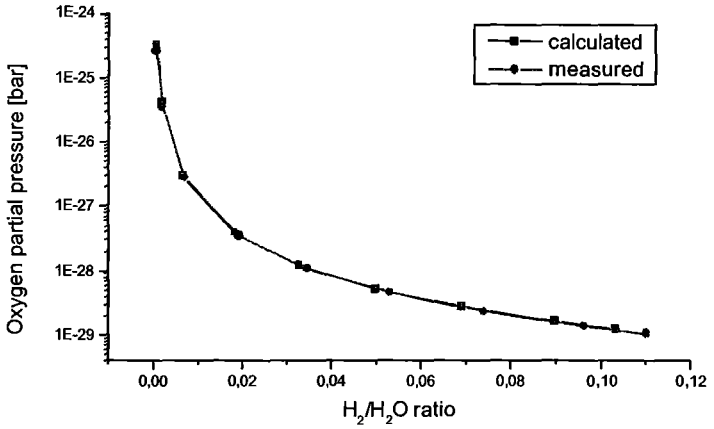

Figure 90: Oxygen partial pressure versus H_2/H_2O ratio. Measured and calculated values at a Pb-Bi temperature of 430°C.

Second, the physical model of the diffusion process, which considers a variable oxygen concentration on the surface of the liquid metal as described above, fits the experimental findings. After a change of the H_2/H_2O ratio the desorption of oxygen was observed and compared with the calculations (figure 91). Applying this model (equation 19) a prediction of the time is possible that is needed in order to reach a desired concentration in the liquid metal bath using the oxygen control system. To the author's knowledge, this is the first theoretical approach to the description of the process of oxygen exchange between gas phase and liquid metal under oxygen control with respect to variable surface concentrations.

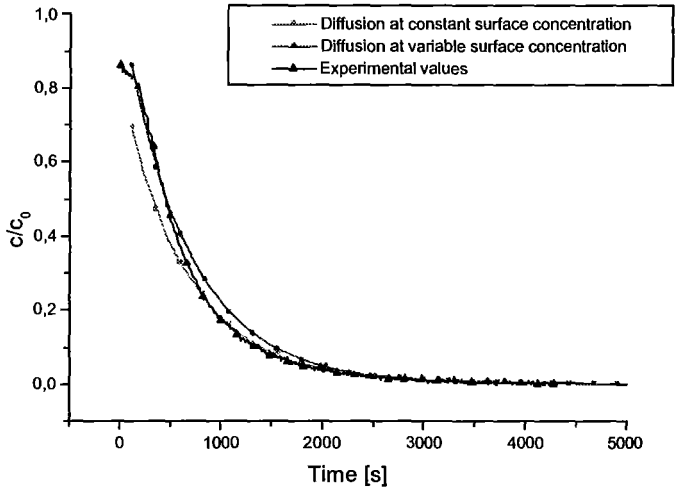

Figure 91: Comparison between diffusion models and experimental data: concentration versus time.

Third, the diffusion coefficient is found to be concentration dependent. From the data of the experiments with stepwise change of the H_2/H_2O ratio, (see figure 89), the diffusion coefficient for oxygen desorption is calculated. For each step of concentration difference another diffusion coefficient is evaluated. One important consequence of this result is the different time behaviour of sorption and desorption of oxygen. In the experiments, the process of desorption is found to be always faster than the process of sorption of oxygen. Furthermore, the expected dependency of the diffusion on the ratio between surface and volume is viewed (figure 92).

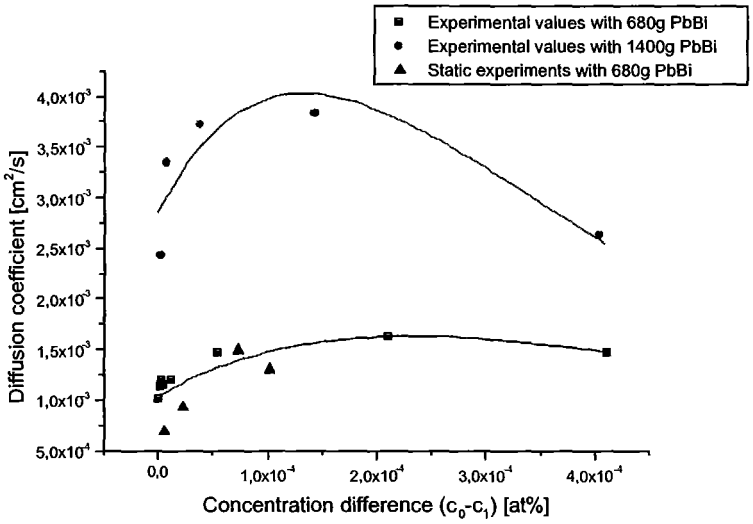

Figure 92: Dependency of diffusion coefficient on concentration difference for different Pb-Bi masses (ratio surface/volume).

2.4.2.4 Summary

Liquid metal loops with Pb or Pb-Bi as spallation material and as coolant are only feasible if the problem of steel corrosion by liquid Pb-Bi at the relevant temperatures is solved. At Forschungszentrum Karlsruhe, this is done by applying an OCS which controls the oxygen concentration in the liquid metal under thermodynamic equilibrium conditions by controlling the H_2/H_2O ratio in the gas atmosphere.
The exchange of oxygen between gas phase and liquid metal is limited by the process of diffusion. The physical model of the kinetics betwen the gas phase and the liquid phase is given. Experimental findings at the oxygen control test stand KOCOS are in excellent agreement with the results of the developed diffusion model. Dependencies on the variable oxygen concentration in the gas phase and the total concentration differences are determined.

3. OVERALL CONCLUSIONS AND PERSPECTIVES

The objective of the HGF Project is to provide the scientific-technical basis which allows the conception and the design of a spallation target. The application of a spallation target is in the fields of, first, spallation neutron source for material investigations and, second, transmutation of highly radioactive waste.

The HGF Strategy Fund Project is divided into three sub-projects:

- SP1: Thermalhydraulic investigations,
- SP2: Material specific investigations,
- SP3: Oxygen control system.

Each sub-project consists of several work packages. All results and deliverables that were due in 2000, could be delivered successfully. In SP1, work package 2, the heat transfer experiment within THESYS could not be performed with Pb-Bi as working fluid, because the HETSS device, which is needed for the heat transfer measurement, was not delivered on time. As a compensation, the same expected physical results were achieved in an experiment performed with Na-K as working fluid in a different test facility.

The major results are:

- KALLA:
  The stagnant experiments COSTA, KOSIMA and KOCOS are in operation. The loop experiment THESYS is in operation; THEADES and CORRIDA are in the commissioning phase.
- SP1: Thermalhydraulic investigations
  Experimental (HYTAS test facility) and numerical (CFX and FIDAP) results for a beam window with water as the model fluid were performed for two international reference designs: the ISTC 559 and the MEGAPIE spallation target. A good agreement between measurement and calculation is achieved. The numerical optimization and the detailed design of a beam window in Pb-Bi (cf. COULI) is in progress.
  A fundamental liquid metal heat transfer experiment is performed, a numerical simulation using FIDAP is finished.
  The benchmark exercise TEFLU (buoyant liquid metal jet) is finished for the TMBF turbulence model in FLUTAN. Deficiencies and further modelling work are outlined.
  A stepwise numerical analysis (1D, 2D and 3D) of a complete spallation target is in progress. The general technical feasibility of the heat removal chain is demonstrated. The integral experiment K4T is proposed and preliminarily designed in order to simulate the thermalhydraulic behaviour of a spallation target including the heat removal chain.
- SP2: Material specific investigations
  The protection of ferritic and austenitic steels is experimentally investigated and proven for exposure times up to 3.000 h, as long as the dilute solution of oxygen in the liquid metal is kept in a representative region (cf. SP3: Oxygen Control System).

Using the GESA test facility, several steel specimens were prepared by surface restructuring and surface aluminium alloying. First experimental results are obtained: Under a cover gas atmosphere with H_2/H_2O = 0.4 (equilibrium oxygen concentration of 8×10^{-6} at%), oxide scales develop on OPTIFER IVc and 1.4970 steel which prevent the dissolution attack of Pb at 550°C. Pb/Bi eutectic alloy appears to be considerably more aggressive: a severe dissolution attack on OPTIFER IVc under the same conditions after 800 h is observed. Surface alloying of Aluminium by GESA provides the best protection due to a thin, dense alumina scale on top of the base material.

- SP3: Oxygen control system (OCS)
  It is successfully demonstrated that electrochemical oxygen meters with Pt/air and In/In_2O_3 reference systems are an in-situ device to measure the chemical activity of dissolved oxygen in liquid lead or lead-bismuth.
  A physical model to describe the kinetics of the exchange of oxygen between the gas atmosphere and the liquid heavy metal is developped and validated with experiments performed in KOCOS.
  The oxygen control system (OCS) is successfully applied to experiments with stagnant lead or lead-bismuth. The next step is the application of the OCS to a loop system.

4. Literature

H.J. Allgeier, 2000
EU Research: the case for more nuclear R&D, Nuclear Europe Worldscan 9-10, p.6

Ansaldo Nucleare, 1999
Energy Amplifier Demonstration Facility Reference Configuration, Summary Report, EA B0.001200-Rev.0, January 1999

R.C. Asher, D. Davies, S.A. Beetham, 1977
Cor. Sci., 17, pp.545

L. Barleon, K.-J. Mack, R. Stieglitz, (1996)
The MEKKA-facility a flexible tool to investigate MHD-flow phenomena, FZKA-5821, September 1996

G. Bauer, M. Salvatores, G. Heusener, 1999
The MEGAPIE Initiative – Executive Outline and Status as per November 1999, Paul Scherrer Institut, Würenlingen Switzerland

W. Baumann, L. Carteciano, B. Dorr, G. Grötzbach, 1999
Validierung des k-ε-σt-Modells im 3D Thermohydraulik-Code FLUTAN 3.0 an Turbulenzmessdaten, Wissenschaftliche Berichte FZKA 6395, Forschungszentrum Karlsruhe

W. Baumann, L. Carteciano, D. Weinberg, 1997
Thermal propagation effects in a vertical turbulent flow behind a jet block - A benchmark exercise. Journal of Hydraulics Research, 1997, Vol. 35, pp. 843-864

V. Bellucci, S. Buono, L. Maciocco, V. Moreau, L. Sorrentino, 1999
Proposal for the fluid-dynamic simulation of the target geometry for the COULI experiment

W.E. Berry, 1971
In „Corrosion in Nuclear Applications", John Wiley and Sons, New York 1971, p. 308

H. U. Borgstedt and H. Glasbrenner, 1995
Development of a direct insulation layer for a self-cooled liquid metal fusion reactor blanket, Proc. 3rd Int. Symp. on Fusion Nuclear Technology, Los Angeles CA, June 27-July 1, 1994, Part A, Fusion Engng. Design 27(1995), pp. 659-662

H.U. Borgstedt, H.D. Röhrig, 1991
J. Nucl. Mater. 596, pp. 179-181

H. Borgwaldt, 1990
CRESOR, a robust vectorized Poisson solver implemented in the COMMIX-2(V) thermal-hydraulics code, Proc. of the 1st Internat. Conf. on Supercomputing in Nuclear Applications, Mito Japan, March 12-16, Japan Atomic Energy Research Institute, Tokyo, p. 346-351

C.D. Bowman, E.D. Arthur, P.W. Lisowski, G.P. Lawrence, R.J. Jensen, J.L. Anderson, B. Blind, M. Cappiello, J.W. Davidson, T.R. England, L.N. Engel, R.C. Haight, H.G. Hughes III, J.R. Ireland, R.A. Krakowski, R.J. LaBauve, B.C. Letellier, R.T. Perry, G.J. Russell, K.P. Staudhammer, G. Versamis, W.B. Wilson, 1992
Nuclear Energy Generation And Waste Transmutation Using an Accelerator-Driven Intense Thermal Neutron Source, Nuclear Instruments and Methods in Physics Research A320, pp. 336-367

F. Carminati, R. Klapisch, J.P. Revol, Ch. Roche, J.A. Rubio, C. Rubbia, 1993
An Energy Amplifier For Cleaner and Inexhaustible Nuclear Energy Production Driven by a Particle Beam Accelerator, CERN/AT/93-47 (ET)

L.N., Carteciano, 1996
Entwicklung eines Turbulenzmodells für Auftriebsströmungen. Dissertation Universität Karlsruhe und Wissenschaftliche Berichte FZKA 5775, Forschungszentrum Karlsruhe

L.N. Carteciano, D. Weinberg, U. Müller, 1997
Development and Analysis of a turbulence Model for Buoyant Flows. Proc. of the 4th World Conf. on Experimental Heat Transfer, Fluid Mechanics and Thermodynamics, Bruxelles, Belgium, June 2-6, Vol. 3, S. 1339-46. Pisa Edition ETS

L. N. Carteciano, M. Wörner, G. Grötzbach, 1999
Erweiterte Turbulenzmodelle für technische Anwendungen von FLUTAN auf Naturkonvektion. Jahrestagung Kerntechnik 1999, Karlsruhe, 18.-20. Mai, pp. 129–133

L.N., Carteciano, G., Grötzbach, 2001
Validation of turbulence models for a free hot sodium jet with different buoyancy flow regimes using the computer code FLUTAN, Wissenschaftliche Berichte FZKA 6600, Forschungszentrum Karlsruhe

X. Cheng, (1994)
Numerical Analysis of Thermally Induced Transients in Forced Flow of Supercritical Helium, Cryogenics, Vol.34, No.3, 195-201

X. Cheng, I. Slessarev, (2000)
Thermal-hydraulic Investigation on a Pilot Liquid Metal Target, Nuclear Engineering and Design 202, pp.297-310

CFX International Services (Harwell Lab.), 1995
CFX 4.1, Flow Solver User Guide, AEA Technology plc, Oxfordshire

J. Crank, 1975
The Mathematics of Diffusion, 2nd Edition, Clarendon Press, Oxford

S. Dementjev, 2000
Personal communications, June 2000

EURATOM, 2001
European Research Area and Proposed Direction of EURATOM Research in FP (2002-2006), http:// europa.eu.int/comm/research/index_en.html

European Commission, 2001
Partitioning and Transmutation: Towards an easing of the nuclear waste management problem, EURATOM Report EUR 19785

Evaluierungskommission, 2000
Nukleare Sicherheits- und Endlagerforschung in Deutschland, Bericht der vom BMWi berufenen Arbeitsgruppe (Evaluierungskommission)

Fluid Dynamics International, 1993
FIDAP 7.0, User Manual

Flow Technology, 1999
Manual of FT Series Turbine Flowmeters, TM-86675 Rev. N, Published by Flow Technology, Inc. May 1999

F. Gesmundo, C. de Asmundis, G. Battilana, E. Ruedl, 1987
Werkstoffe und Korrosion, 38, pp.367

M.M., Gibson, B.E., Launder, 1978
Ground effect on pressure fluctuations in the atmospheric boundary layer. J. of Fluid Mech., 86, 491-511.

Grötzbach, G., Carteciano, L.N., Dorr, B., 2000
Numerical Analysis of Experiments modelling LWR Sump Cooling by Natural Convection, International Atomic Energy Agency, Technical Committee Meeting on "Natural Circulation Data and Methods for Innovative Nuclear Power Plant Design", Vienna, Austria, July 18-21

C. Guminski, 1990
Metallkunde 81, pp. 105

K. Hauffe, 1965
Oxidation of Metals, Plenum Press 1965

G. Heusener, M. Salvatores, 1998
Use of heavy liquid metal: A perspective for critical/subcritical fast neutron concepts, HLMC'98, 5-9 October, Obninsk, Russia

X. Jin, 2001
Rechenverfahren zur Diskretisierung von Strömungen in komplexer Geometrie mittels körperangepasster Gitter, Dissertation Universität Karlsruhe und Wissenschaftliche Berichte FZKA 6596, Forschungszentrum Karlsruhe

W. Jost, 1970
Diffusion in Solids, Liquids, Gases, Sixth Printing, Academic Press, NewYork

KALLA, 2001
The KArlsruhe Lead Laboratory KALLA Server under http:// kalla.fzk.de

J.-U. Klügel, R. Gilli, J. Vigfusson, 1999
Ergebnisse einer ersten sicherheitstechnischen Beurteilung des Konzeptes eines bleigekühlten Energy Amplifiers aus behördlicher Sicht, atw 44, Heft 11, pp. 664-669

J.U. Knebel, 1993
Experimentelle Untersuchungen in turbulenten Auftriebsstrahlen in Natrium, Dissertation, Univ. Karlsruhe, KfK 5175, Kernforschungszentrum Karlsruhe

J.U. Knebel, X. Cheng, G. Müller, G. Schumacher, J. Konys, O. Wedemeyer, G. Grötzbach, L. Carteciano, 2000
Thermalhydraulic and Material Specific Investigations into the Realization of an Accelerator Driven System (ADS) to Transmute Minor Actinides, 1999 Status Report, Forschungszentrum Karlsruhe, Wissenschaftliche Berichte FZKA 6506

J.U. Knebel, et al. 2001
KArlsruhe Lead LAboratory KALLA – A Technical Description, Forschungszentrum Karlsruhe, Wissenschaftliche Berichte FZKA, (to be published)

J.U. Knebel, G. Heusener, 2000
Research on Transmutation and Accelerator Driven Systems at the Forschungszentrum Karlsruhe, Int. Zeitschrift für Kernenergie atw, Jg.45, Heft 6, pp. 350-358

J.U. Knebel, L. Krebs, 1994
Calibration of a miniature permanent magnet flowmeter probe and its application to velocity measurements in liquid sodium, Exp. Thermal and Fluid Sci. 8, pp.135-148

J.U. Knebel, L. Krebs, U. Müller, B.P. Axcell, 1998
Experimental Investigation of a Confined Heated Sodium Jet in a Co-Flow, J. Fluid Mech, vol. 368, pp. 51-79

L. Krebs, K. Bremhorst, 1983
Verification of the extended gradient diffusion model by measurement of the mean and fluctuating temperature fields in sodium flow downstream of a multi-bore jet block, Proc. 4th Symp. Turbulent Shear Flows, Karlsruhe, FR Germany, 17.1-17.5.

K. Kuroda, P.A. Luban, G. Welsch, T.E. Mitchell, 1983
Oxidation of Metals, 19, pp.117

C.H. Lefhalm, J.U. Knebel, K.J. Mack, 2001
Kinetics of Gas Phase Oxygen Control System (OCS) for Stagnant and Flowing Pb-Bi Systems, Journal of Nuclear Materials Vol. 296/1-3, pp. 301-304

L., Maciocco, 2000
Proposal for the benchmarking activity on the TEFLU sodium jet experiment

V. Markov, 1997
Corrosion of structural materials in Pb-Bi and Pb, Seminar on the Concept of Lead-Cooled fast Reactor, Cadarache, September 22-23

W. Maschek, D. Thiem, G. Heusener, 1999
Safety assessment of a reactor core dedicated to burn minor actinides, Proc. of the Jahrestagung Kerntechnik'99, Karlsruhe, pp.635-638

T.B. Massalski, 1990
Editor, Binary phase Diagrams, 2nd Edition, ASM International

G. Müller, 2000
Korrosionsverhalten von Stählen in flüssigem Blei nach Behandlung mit hochenergetischen gepulsten Elektronenstrahlen, Dissertation Universität Karlsruhe und Forschungszentrum Karlsruhe, Wissenschaftliche Berichte FZKA 6422

G. Müller, G. Schumacher, D. Strauß, 1998
Oxide scale growth on MCrAlY coatings after pulsed electron beam treatment, Surface and Coating Technology, Vol. 43, pp. 108-109

G. Müller, G. Schumacher, D. Strauß, V. Engelko, A. Andreev and V. Kavaljov, 1996
Modification of material surfaces by the pulsed electron beam facility GESA, K. Jungwirth [Hrsg.], Beams 96: Proc. Of the 11th Intern. Conf. On High-power Particle Beams, praha, CR, June 10-14, Vol. 2 pp. 809-812

St. Müller, G. Thun, 1977
Permanentmagnetische Durchflußmesser-Sonde für flüssige Metalle, KfK-Report 2429, Kernforschungszentrum Karlsruhe, FR Germany

Y. Nagano, C., Kim, 1988
A two-equation model for heat transport in wall turbulent shear flows, J. Heat Transfer, 110, 583-589

Natec Schultheiss, 2001
http://www.natec.org/products/durchflussmesstechnik.html

H.J. Neitzel, J.U. Knebel, 2000
Forschungszentrum Karlsruhe, Interner Bericht

Y. Orlov, 1998
Stages of Development of Lead-Bismuth as a Coolant for Nuclear Reactors in Russia, Presentation at Forschungszentrum Karlsruhe, IATF, July 7

Panametrics, (2000)
http:// www.panametrics.com, info 6/2000

W.S. Park, 1999
HYPER (Hybrid Power Extraction Reactor) System Design Study, Report of Korean Atomic Energy Research Institute KAERI/TR-1316/99

Paul Scherrer Institute, 1997
PSI Annual Report 1997 on: Solid State Research at Large Facilities, Annex IIIA, Paul Scherrer Institute (PSI) Switzerland

I. Platnieks, G.S. Bauer, O. Lielausis, Y. Takeda, 1998
Measurements of Heat Transfer at the Beam Window in a Mockup Target for SINQ using mercury, 14th Meeting of the Intern. Collaboration on Adv. Neutron Sources, Starved Rock Lodge, Utica, Ill., USA, June 14-19

W., Rodi, 1980
Turbulence models and their application in hydraulics. MH DELFT, The Netherlands

W. Rodi, 1985
Turbulenzmodelle und ihre Anwendung, Scriptum zur Vorlesung an der TH Karlsruhe 1985/86

PSI Annual Report, 1997
Condensed Matter Research with Neutrons
Annex IIIA, Paul Scherrer Institut, Würenlingen, Switzerland

C. Rubbia, Rubio, J.A., Buono, S., Carminati, F., Fiétier, F., Galvez, J., Gelès, C., Kadi, Y., Klapisch, R., Mandrillon, P., Revol, J.P., Roche, Ch., 1995
Conceptual design of a fast neutron operated high power energy emplifier, CERN/AT/95-44(ET)

B., Smith, 2000
Personal Information, Paul Scherrer Institut, Würenlingen, Switzerland

B., Sigg, 2001
Personal Information, Paul Scherrer Institut, Würenlingen, Switzerland

Y. Takeda, H. Kikura, 1997
Measurement of Liquid Metal Flow in a SINQ Target Geometry, in: PSI Annual Report 1997 Annex IIIA, pp. 20-21

D. Talbot, J. Talbot, 1968
Corrosion Science and Technology, CRC Press, 1998

T. Takizuka, K. Tsujimoto, T. Sasa, H. Takano, K. Hirota, Y. Kamishima, 1998
Heavy liquid-metal cooling option of JAERI accelerator-driven transmutation systems, HLMC'98, Vol.1, pp.143-155, October 5-9, Obninsk, Russia

Technical Working Group, 2001
A European Roadmap for Developing Accelerator Driven Systems (ADS) for Nuclear Waste Incineration, Issued by the Enlarged TWG on ADS chaired by C. Rubbia, April

G. van Tuyle, 2000
Plan to Assess and Develop Accelerator Driven Waste Transmutation Technology, 4th Topical Meeting on Nuclear Applications of Accelerator Technology, Washington DC, November 12-16

United States Department of Energy, 1999
A Roadmap for Developing Accelerator Transmutation of Waste (ATW) Technology, A Report to Congress, DOE/RW-0519, October 1999

VDI-Wärmeatlas, 1974
Abschnitt L, 2. Auflage

H. Wider, 1998
Safety of acclerator-driven nuclear waste burners, Proc. of the Jahrestagung Kerntechnik'98, München, pp.217-220

G. Willerding, W. Baumann, 1996
FLUTAN 2.0 Input Specifications, Forschungszentrum Karlsruhe, Wissenschaftliche Berichte FZKA 5712, Mai 1996

M., Wörner, G., Grötzbach, 1996
Analysis of the transport equation of temperature variance dissipation rate by direct numerical simulation data of natural convection. "Engineering Turbulence Modelling and Experiments 3", Eds.: W. Rodi, G. Bergeles, Elsevier Science B. V., pp. 229-238

M. Wörner, G. Grötzbach, 1997
DNS database of turbulent natural convection in horizontal fluid layers. World Wide Web-site http:// www.fzk.de/irs/turbit

M. Wörner, Q.-Y. Ye, G. Grötzbach, 1999
Consistent modelling of fluctuating temperature-gradient-velocity-gradient correlations for natural convection. "Engineering Turbulence Modelling and Experiments 4", Eds.: W. Rodi, D. Laurence, Elsevier Science B. V., pp. 165-174

Q.-Y., Ye, M., Wörner, G., Grötzbach, J., Jovanovic, 1997
Modelling turbulent dissipation rate for Rayleigh-Bénard convection. „Turbulence, Heat and Mass Transfer 2", Eds.: K. Hanjalic, T.W.J. Peeters, Delft University Press, pp. 331-340

E. Yefimov, (1998)
The main results of feasibility study of liquid metal targets and the working plan on the project ,559, Kick-Off Meeting on the ISTC Project #559, February, Obninsk, Russia